UNIVERSIDADE DE LISBOA
FACULDADE DE CIÊNCIAS

The shape of days to come: effects of climate change on building energy consumption

" Documento Definitivo"

Doutoramento em Ciências Geofísicas e da Geoinformação

Especialidade de Meteorologia

João Maria Bravo Vieira Dias

Tese orientada por:

Professor Doutor Guilherme Carvalho Canhoto Carrilho da Graça

Professor Doutor Pedro Miguel Matos Soares

Documento especialmente elaborado para a obtenção do grau de doutor

2021

UNIVERSIDADE DE LISBOA
FACULDADE DE CIÊNCIAS

The shape of days to come: effects of climate change on building energy consumption

Doutoramento em Ciências Geofísicas e da Geoinformação

Especialidade de Meteorologia

João Maria Bravo Vieira Dias

Tese orientada por:

Professor Doutor Guilherme Carvalho Canhoto Carrilho da Graça

Professor Doutor Pedro Miguel Matos Soares

Júri:

Presidente:

- Doutor João Manuel de Almeida Serra, Professor Catedrático e Presidente do Departamento de Engenharia Geográfica, Geofísica e Energia, Faculdade de Ciências da Universidade de Lisboa

Vogais:

- Doutor Lorenzo Pagliano, Associate Professor, Dipartimento di Energia do Politecnico di Milano, Itália
- Doutor Pieter de Wilde, Professor, Faculty of Arts, Humanities and Business da University of Plymouth, Reino Unido
- Doutor Miguel Centeno da Costa Ferreira Brito, Professor Auxiliar com Agregação, Faculdade de Ciências da Universidade de Lisboa
- Doutor Guilherme Carvalho Canhoto Carrilho da Graça, Professor Auxiliar, Faculdade de Ciências da Universidade de Lisboa

Documento especialmente elaborado para a obtenção do grau de doutor

Doutoramento financiado pela Fundação para a Ciência e a Tecnologia (PB/BD/114487/2016)

2021

Acknowledgments

Esta tese, desenvolvida nos últimos cinco anos, só foi possível graças a um conjunto de pessoas que me apoiou e guiou, pessoal e profissionalmente, e aos quais expresso a minha gratidão:

Aos meus orientadores, pelo desafio lançado há mais de cinco anos e pela oportunidade de me iniciar no mundo da investigação. Ao Professor Guilherme Carrilho da Graça por todas as discussões, ideias e ensinamentos, e ao Professor Pedro Soares pelo apoio e discussões sobretudo sobre clima futuro.

Ao Instituto Dom Luiz, em especial ao programa doutoral EarthSystems, e ao Grupo de Edifícios da Faculdade de Ciências da Universidade de Lisboa.

Ao Dr. Nuno R. Martins e João Francisco Pinto, por disponibilizarem os seus modelos; à Dr. Rita M. Cardoso, pelos dados de clima; ao Dr. Nuno M. Mateus, Miguel Vargues, Gonçalo Vilela e Câmara Municipal do Seixal, pela partilha dos dados de medições; e ao Rafael, pela ajuda final com o *EnergyPlus*.

Ao Nuno Mateus, Nuno Martins, Filipa, Daniel e Ângelo, por tudo o que aprendi com vocês, pelo BujaBall e todos os bons momentos passados no Bunker.

À malta do EarthSystems; Andreia, Dorota, Filipa, às Joanas (JC e JF), ao Alex e Riccardo (ainda estou a contar com a subida ao Pico!) e ao Rodrigo, por todas as discussões fora do mundo da Energia e, claro, toda amizade construída nos últimos anos.

Ao grupo dos almoços, lanches e, ultimamente, zooms, pela amizade e pelas pep talks.

Aos que foram perguntando quando é que deixava de estudar e começava a trabalhar.

Aos meus pais, irmão e avós, sobretudo à minha Avó Géna que nos últimos meses perguntava constantemente se já tinha terminado.

E à Sara, por tudo!

Abstract

Climate change effects vary with region, season, and time of the day. Existing annual and diurnal temperature cycles will shift and be reshaped, leading to increased air temperatures earlier and later in the year. Buildings will be affected by these changes, especially the ones using passive design strategies, whose performance is highly weather dependent. Building energy simulation (BES) is key for building energy design and optimization. Since most buildings last 50+ years, BES must use future weather data accounting for climate change. Presently, photovoltaic (PV) energy self-consumption must be maximized through building demand flexibility and energy storage, because of grid and economic interests. However, clouds can shade PV systems, reducing production and increasing grid demand, particularly in the cooling season.

This thesis addresses three complementary research topics that build on the use of high-resolution state-of-the-art historical and future climate data. First, two methods to produce future climate data for BES are compared. Secondly, upcoming changes in temperature, their interaction with solar radiation, and the consequent impacts on passive building strategies are analysed in the EU 43 most populated cities. Finally, cloud shading periods capable of triggering demand flexibility events are analysed and simulated.

The results show that current methods used to produce future climate data for BES, produce reliable results when correctly applied. Upcoming climate change will impact diurnal temperature cycle by increasing or decreasing the daily temperature range depending on season and region. Further, natural ventilation and shading seasons will be affected, with a higher impact on energy consumption in Southern Europe. Finally, cloud shading periods vary with climate but, on average, clouds last 20 minutes and occur predominately in the afternoon. The simulation results show that grid energy demand can be reduced by 60 % while maintaining comfortable indoor conditions.

Keywords: Climate change; future weather data; low energy buildings; demand flexibility; cloud shading.

Resumo

As alterações climáticas são um dos maiores desafios contemporâneos. Entre 1880 e 2020 a temperatura média global aumentou 1.2 ºC. Estas alterações, que não se limitam à temperatura, mas também à precipitação e vento, têm-se verificado em todo o planeta e já são visíveis as suas consequências ao nível do consumo de energia, na economia e na saúde humana. Nas últimas décadas, o aumento da temperatura tem-se acentuado, assim como o aumento da ocorrência de fenómenos climáticos extremos, como ondas de calor. Por exemplo, na Europa Ocidental a frequência de dias quentes triplicou e a duração das ondas de calor duplicou entre 1880 e 2005. As projeções climáticas para o futuro confirmam estas tendências de agravamento das alterações climáticas. No cenário *business as usual* projeta-se um aumento da temperatura média global em 4 ºC até ao final do século, assim como um intensificar dos eventos de temperatura extremos. Estes aumentos irão variar dependendo da região do globo, da estação do ano e do período do dia. Projeções futuras também apontam que os ciclos anual e diário da temperatura serão modificados, resultando em temperaturas elevadas fora do típico período de verão, ocorrendo tanto mais cedo como mais tarde no ano. Para enfatizar o problema, o continuo desenvolvimento urbano irá intensificar este problema, sobretudo em grandes zonas urbanas, onde a grande maioria da população mundial irá residir.

Os edifícios são um dos maiores emissores de gases de efeito de estufa, contribuindo com cerca de 50 % das emissões de CO2 na União Europeia, 43 % nos Estados Unidos da América e mais de 50 % na China. Os edifícios consomem cerca de 40 % da energia final total consumida, sendo que nos países desenvolvidos cerca de metade é utilizada para aquecimento, ventilação e ar condicionado (HVAC).

Os edifícios são construídos para durarem mais de 50 anos, como tal um edifício contemporâneo irá estar sujeito às alterações climáticas e, portanto, a um clima mais quente e com a incidência de mais extremos. Este aquecimento, combinado com maiores exigências de conforto, por parte dos ocupantes e da legislação, irá resultar no aumento do consumo de energia para arrefecimento tanto em edifícios comerciais como residenciais. Para limitar estes aumentos, os designers têm vindo a ser encorajados a usar estratégias de design passivas e sistemas de arrefecimento passivo, como é o caso de ventilação natural (NV), arrefecimento noturno (NC), controlo otimizado dos ganhos solares, aumento do isolamento térmico, controlo da infiltração do ar e uso de massa térmica exposta. Todas estas estratégias utilizam o clima exterior como uma fonte de arrefecimento grátis ou de baixo consumo energético. Sem surpresa, a eficácia destas estratégias está intrinsecamente ligada ao clima exterior,

particularmente à temperatura, vento, radiação solar e humidade. Consequentemente, se os edifícios não forem preparados e corretamente desenhados para um clima em mudança, estas estratégias podem resultar em temperaturas elevadas no interior dos edifícios, comprometendo o conforto, a saúde ou a vida dos ocupantes. Ao mesmo tempo, existe uma necessidade crescente para incorporar fontes energia local no edificado, como energia solar fotovoltaica (PV). No entanto, a produção destas fontes de energia locais terá de ser otimizada para autoconsumo, de forma a que os produtores maximizem o retorno do seu investimento e não causem problemas na rede de distribuição.

Atualmente, os designers recorrem à simulação energética de edifícios (BES) para garantirem um maior grau de fiabilidade dos reais impactos das soluções construtivas selecionadas. Uma BES necessita de utilizar dados climático que seja representativo da localização do edifício, sendo o ficheiro habitualmente constituído por um ano de dados com resolução horária. Estes ficheiros são construídos utilizando dados históricos e idealmente consideram 30 anos de medições, de forma a representar o clima típico do local. No entanto, com as expectáveis alterações climáticas, os edifícios atualmente construídos deverão ser simulados não só considerando o clima histórico, mas sobretudo o clima futuro, onde na realidade estes irão operar.

Os efeitos das alterações climáticas irão variar com a região, a estação do ano e com a hora do dia. Os ciclos de temperatura anual e diurno irão ser modificados e as suas formas típicas serão alteradas, resultando em temperaturas mais elevadas tanto mais cedo com mais tarde no ano. Os edifícios irão ser impactados por estas alteração, particularmente os que utilizam estratégias de design passivas que são extremamente dependentes do clima exterior. Para garantir que estas estratégias são corretamente desenhadas e otimizadas é necessário recorrer a BES. Sabendo que os edifícios hoje construídos ainda estarão em pleno funcionamento daqui a 50 anos, é fundamental que se simule também o clima futuro. No curto prazo, a produção de energia PV nos edifícios tem de ser focada no autoconsumo, para maximizar o retorno do investimento e minimizar o impacto na rede. Isto poderá ser conseguido recorrendo a estratégias como flexibilidade do lado do consumo e o armazenamento de energia. Estas duas estratégias poderão ser combinadas quando nuvens causam sombreamento dos sistemas PV, principalmente em edifícios de escritórios predominantemente em arrefecimento. Habitualmente, nestes períodos a produção de energia diminui, enquanto as necessidades de arrefecimento mantém-se, obrigando os edifícios a recorrer à rede elétrica.

Esta tese está dividida em três tópicos/estudos de investigação complementares entre si e que assentam no uso de dados de clima histórico e futuro de alta resolução temporal e espacial. No primeiro tópico, dois métodos utilizados habitualmente para a produção de ficheiros climáticos futuros para BES são comparados. No segundo tópico, projeções climáticas futuras de temperatura são analisadas detalhadamente, assim como a sua interação com o vento e radiação solar, e os seus possíveis impactos em estratégias de design passivo são avaliados. Por fim, são analisados, medidos e simulados períodos de nebulosidade com impacto na produção PV e capazes de desencadear eventos de flexibilidade do lado do consumo.

A primeira parte da tese apresenta uma comparação entre dois métodos de produzir dados climáticos futuros para BES: *Morphing* e *typical meteorological year of future climate* (F-TMY), assim como uma análise de sensibilidade de várias formas de produzir ficheiros com *Morphing*. O estudo utilizou 10 anos de dados horários históricos e futuros de um modelo regional de clima de alta-resolução (9 km) cujo domínio cobre a Ibéria. Os métodos foram comparados através da análise das anomalias na temperatura do ar e nos impactos de BES ao nível do consumo de energia anual e pico dos sistemas HVAC de quatro edifícios. Os resultados mostram que *Morphing* de alta qualidade tem uma performance semelhante ao *F-TMY* (diferenças médias de 8 % contra 7 %). No entanto, caso o *Morphing* utilize dados de baixa resolução, projeções climáticas antiquadas ou um clima de referência errado os erros médios situam-se entre 16 e 20 %, tornando estes dados inadequados para BES.

Na segunda parte, foram utilizados dados modelados de alta resolução (sub-diários e mensais) para o clima histórico (1971-2000) e futuro (2071-2100) para avaliar as alterações na temperatura, vento e radiação solar, e os seus impactos em estratégias de design passivas, nas 43 cidades mais populosas da EU. Os resultados mostram que o ciclo diurno da temperatura irá ser alterado e a amplitude térmica diária (DTR) será modificada, resultando duas novas formas no ciclo diário de temperatura: uma diurna (aumento do DTR) e outra noturna (diminuição do DTR), que terão impactos diferentes consoante a estação do ano. Adicionalmente, dias amenos e quentes ocorrerão mais cedo no ano e persistirão até mais tarde ao longo do ano, modificando as temporadas habituais de NV e de sombreamento. Em toda a Europa a eficácia das estratégias de design passivo irá diminuir, com exceção da Escandinávia e Ilhas Britânicas. Na Europa do Norte a estação de NV durará mais 6 semanas, enquanto na Europa do Sul diminuirá em 9 semanas. Na Europa do Sul será necessário sombreamento durante mais 2.5 meses, comprometendo a eficácia das palas horizontais utilizadas para sombreamento. Nos limites da

estação de sombreamento, a radiação solar direta numa janela virada a Sul irá aumentar em 60 % devido a uma redução média de 13.5º da altitude solar máxima diária.

Na terceira parte, foram utilizados dados de estações meteorológicas com uma resolução de 1 minuto para analisar a eficácia da utilização de períodos de sombreamento causados por nuvens em sistemas PV, para desencadear eventos de flexibilidade do lado do consumo (através do desligar do HVAC). Esta análise foi feita recorrendo a medições num escritório ocupado e a BES. Adicionalmente, foi realizada uma análise de períodos de nebulosidade (mínimo de 5 minutos) que poderão desencadear os eventos de flexibilidade em diferentes climas. Foram identificados quatro regimes de nuvens (nublado, nublado frio, nublado quente, e quente) e a maioria dos eventos dura menos de 20 minutos e ocorre durante a tarde, independentemente do clima. As medições mostraram que o escritório em estudo demorou 50 minutos a aumentar a temperatura interior em 2 ºC. Por fim, os resultados da BES mostraram que os eventos de flexibilidade permitem reduzir em 60 % o consumo de energia da rede durante a estação de arrefecimento, sem comprometer o conforto dos ocupantes.

Palavras-chave: Alterações climáticas; dados climáticos futuros; estratégias de design passivas; flexibilidade do lado do consumo; períodos de nebulosidade.

List of original contributions

Paper 1: **João Bravo Dias**, Guilherme Carrilho da Graça, Pedro M.M. Soares, *Comparison of methodologies for generation of future weather data for building thermal energy simulation*, Energy and Buildings, Volume 206, 2020, 109556, ISSN 0378-7788, https://doi.org/10.1016/j.enbuild.2019.109556.

Paper 2: **João Bravo Dias**, Pedro M.M. Soares, Guilherme Carrilho da Graça, *The shape of days to come: Effects of climate change on low energy buildings*, Building and Environment, Volume 181, 2020, 107125, ISSN 0360-1323, https://doi.org/10.1016/j.buildenv.2020.107125.

Paper 3: **João Bravo Dias**, Guilherme Carrilho da Graça, *Using building thermal mass energy storage to offset temporary BIPV output reductions due to passing clouds in an office building*, Building and Environment, Volume 207, Part B, 2022, 108504, ISSN 0360-1323, https://doi.org/10.1016/j.buildenv.2021.108504.

Contents

Acknowledgments i
Abstract ii
Resumo iii
List of original contributions vii
Contents ix
List of Acronyms, abbreviations and symbols xi
List of Figures xv
List of Tables xvii
Chapter 1 - Introduction 1
1.1 Research questions 5
1.2 Thesis structure 5
Chapter 2 - Comparison of methodologies for generation of future weather data for building thermal energy simulation 7
2.1 Introduction 7
2.2 Weather data for building energy simulation 8
2.2.1 Typical Meteorological Year 8
2.2.2 Future climate 9
2.3 Methodology 11
2.3.1 Climate data 11
2.3.2 BES methodology 18
2.3.3 Data analysis 21
2.4 Results and discussion 24
2.4.1 Temperature analysis of future climate data files 25
2.4.2 Impact on building energy consumption 29
2.4.3 Impact of inter-annual variability 36
2.5 Conclusions 37
Chapter 3 - The shape of days to come: effects of climate change on low energy buildings 40
3.1 Introduction 40
3.2 Methodology 43
3.2.1 Climate data 44
3.2.2 Changes in shape of days 46
3.2.3 Shifts in NV potential 47
3.2.4 Days with similar maximum temperature 49
3.2.5 Optimal overhangs and solar gains 50
3.3 Results and discussion 52

3.3.1 Capability of RCM to represent urban heat island 52
3.3.2 Changes in shape of days 52
3.3.3 Shifts NV potential 57
3.3.4 Days with similar maximum temperature 61
3.3.5 Optimal overhangs and solar gains 62
3.4 Conclusions 64
Chapter 4 - Using building thermal mass energy storage to offset temporary BIPV output reductions due to passing clouds in a cooling dominated office building 67
4.1 Introduction 67
4.2 Methodology 70
4.2.1 Weather data 71
4.2.2 Office building test case 74
4.2.3 Whole building thermal simulation model 78
4.3 Results and discussion 82
4.3.1 Cloud shading periods 83
4.3.2 Measurements and calibration of the dynamic thermal simulation model 86
4.3.3 Whole building simulation 88
4.4 Conclusions 92
Chapter 5 – General conclusions 94
Chapter 6 - Bibliography 96

List of Acronyms, abbreviations and symbols

ach	Air changes per hour
AHU	Air handling units
ALI	Alicante
A_{open}	Window opening Area
$A_{open,max}$	Maximum window openable area
BaB	Building thermal mass as a battery
BAR	Barcelona
BES	Building energy simulation
BIL	Bilbao
BIPV	Building integrated photovoltaic
BS-22	Reference scenario with HVAC cooling setpoint set to 22 ºC
BS-24	Reference scenario with HVAC cooling setpoint set to 24 ºC
C	Heat capacity
CDD	Cooling Degree Days
CDF	Cumulative distribution function
CDH	Cooling Degree Hours
CDH_{res-NC}	Residual CDH due to night cooling ventilation
CDH_{res-WD}	Residual CDH due to wind-driven natural ventilation
CL-24	Flexibility triggered by cloud shading periods
CMIP5	Coupled Model Intercomparison Project
CO_2	Carbon Dioxide
COP	Coefficient of performance
COR	A Coruña
C_p	Specific heat capacity of the material
C_T	Zone capacitance multiplier
CV	Coefficient of variation
C_z	Total heat capacity of the zone
day	Number of days
DBT	Dry bulb temperature
DHW	Domestic hot water
DJF	December, January, February
dt	Time interval (3 hour)
DTR	Daily Temperature Range
EF	Exploitation factor
EPL-TMY	Past TMY download from EnergyPlus weather database
EU	European Union
E_{vent}	Electrical energy use of the fan coils
F-10Y	10-year file of future hourly data (2090-2099);
FF	Optimal overhang day Future, climate Future
FP	Optimal overhang day Future, climate Past
f_{rw}	Reduction factor applied to replicate the discharge coefficient
FS	Finkelstein-Schafer statistics

F-TMY	Typical meteorological year of future climate
G	Global horizontal radiation (G)
G_0	Extra-terrestrial incident irradiance
GCM	General Circulation Models
GHG	Greenhouse gas
GRA	Granada
HadCM3	Hadley Centre Coupled Model 3
HDD	Heating Degree Days
h_o	Operation hours
HVAC	Heating, ventilation and air conditioning
IAQ	Indoor air quality
$I_{diffuse}$	Diffuse horizontal solar radiation
I_{direct}	Direct horizontal solar radiation
$I_{direct,façace}$	Direct solar radiation incident on the south facing façade
I_{global}	Total solar radiation
IPPC	Intergovernmental Panel on Climate Change
IWEC	International Weather Year for Energy Calculations
JJA	June, July, August
ko	Ranked order number
k	Conductivity
k_t	Clearness index
LIS	Lisbon
M	Number of days during the month
MAD	Madrid
MAD	Mean absolute difference
MAL	Malaga
MAM	March, April, May
MAPD	Mean absolute percentage difference
M-CCT	Morphed EPL-TMY using the CCWorldWeatherGenerator tool
M-EPL	Morphed EPL-TMY.
M-TMY	Morphed TMY file;
MUR	Murcia
ne	Total number of elements
n	Number of hours
NC	Night cooling
nday,cd	Number of hours with cooling demand
nday,nc	Number of hours with nigh cooling potential
NO_x	Nitrogen Oxide
NV	Natural ventilation
OLR	Overhang length ratio
OOR_{Future}	Overhang obstruction ratio on the window plane
OVI	Oviedo
P	Density of the material

P-10Y	10-year file of past hourly data (1990-1999)
PCM	Passive change materials
PF	Optimal overhang day Past, climate Future
POR	Porto
PP	Optimal overhang day Past, climate Past
P-TMY	Past TMY file;
PV	Photovoltaic
PV-24	Flexibility triggered by BIPV production shortages
P_{vent}	Average fan coil pressure drop
RCM	Regional Climate Model
RCP	Representative Concentration Pathways
RE	Renewable energy
SEV	Sevilla
SO_2	Sulphur Dioxide
SON	September, November, December
t	Duration of the event
T_{base}	Base temperature
TC	Too Cold
T_{cond}	Condenser temperature
T_{evap}	Evaporation temperature
$T_{F,h}$	Diurnal temperature cycle for future climate
$T_{F,m}$	Average temperature future climate
$\bar{T}_i$	Mean daily temperature (average between daily maximum and minimum temperatures)
TMY	Typical Meteorological Year
T_{out}	Outdoor air temperature
$T_{P,h}$	Diurnal temperature cycle for past climate
$T_{P,m}$	Average temperature past climate
TW	Too Warm
UHI	Urban Heat Island
US	United States of America
V	Volume
$\dot{V}$	Volume flow rate
V_{air}	Indoor air velocity
VAL	Valencia
VC	Ventilative Cooling
V_{wind}	Wind speed
W_j	Weighting factor for each variable (j)
WRF	Weather Research and Forecasting
WS	Weighted statistics
x	Morphed climate variable,
x_0	Present-day climate variable
$<x_0>_m$	Monthly mean value of the climate variable

Y_i	Reference value
Y_j	Mean value
$\hat{Y}_i$	Value obtained with the other methodology
ZAR	Zaragoza
α	Solar altitude
α_m	Fractional change in the monthly mean
δ_k	Absolute difference between long-term CDF and short-term CDF
δ_p	Thermal penetration depth
ΔT_h	Diurnal Temperature Cycle
$\Delta T_{v,air}$	Temperature decrease perceived by the occupants due to air velocity
Δx_m	Projected absolute change in monthly mean for the month (m)
σ_i	Standard variation
η_{vent}	Average fan efficiency
Ψ	*E*fficiency heating and cooling

List of Figures

Figure 2.1 Fifteen biggest metropolitan regions in Iberia [] 13
Figure 2.2 Schematic representation of the different climate data files 13
Figure 2.3 Building simulation model section cut and zones [106]. 20
Figure 2.4 Townhouse building and floor plan [111]. 21
Figure 2.5 Average future seasonal temperatures (ºC): DJF (December, January, February), MAM (March, April, May), JJA (June, July, August), SON (September, November, December). Boxplots of F-10Y with green dark dots representing the mean of F-10Y, in blue F-TMY, in red M-TMY, in orange M-EPL and in white M-CCT. 26
Figure 2.6 Annual heating energy consumption (Townhouse buildings) and annual HVAC electric energy consumption (Office buildings). Boxplots of the F-10Y with green dark dots representing the mean of F-10Y, in blue F-TMY, in red M-TMY, in orange M-EPL and in white M-CCT. 31
Figure 2.7 Peak hourly heating energy consumption (Townhouse buildings) and peak hourly HVAC electric energy consumption (Office buildings). Boxplots of F-10Y with green dark dots representing the mean of F-10Y, in blue F-TMY, in red M-TMY, in orange M-EPL and in white M-CCT. 33
Figure 2.8 Summer overheating hours (%) of the standard townhouse building (top) and optimized townhouse building (down) calculated for all the cities and methods: boxplots of the multi-year data with green dark dots representing the mean of the multi-year data, in blue F-TMY, in red M-TMY, in orange M-EPL and in white M-CCT 35
Figure 3.1 Representation of future annual shifts in daily average temperature and changes in future shape of days 42
Figure 3.2 Schematic representation of the different analysis and spatial distribution of 43 most populated cities in the EU. 43
Figure 3.3 The four steps used to obtain the diurnal temperature cycle difference and the two shapes patterns. 47
Figure 3.4 Mean, maximum, and minimum temperatures differences between the city centre and the surrounding grid points for past and future climate at Paris and London. 52
Figure 3.5 Average season temperature of future climate (colour scheme) and average season temperature increase between future and past climates (circle size). 53
Figure 3.6 Boxplots of DTR change function of the hour of maximum monthly temperature increase calculated for all cities and months. 54
Figure 3.7 Hour of maximum monthly temperature increase and amplitude of the monthly diurnal temperature cycle. 56
Figure 3.8 Difference in the number of weeks in each temperature interval, between past and future datasets. 58
Figure 3.9 Cooling Degree Hours (CDH) for past and future climates 59
Figure 3.10 CDH (colour scheme) and CDH relative reduction due to wind driven NV (%) 60
Figure 3.11 CDH (colour scheme) and CDH relative reduction due to night cooling (%) 61
Figure 3.12 Average first and last day, DTR, total daily radiation, and direct solar radiation at solar noon incident on a south facing façade differences between future and past climates for days with similar maximum temperature. 62
Figure 3.13 Average maximum solar altitude at London (North), Paris (Mid-North), Rome (Mid-South) and Madrid (South) for days with similar maximum temperature. 62
Figure 3.14 Overhang length ratio (OLR) for past and future climates 63

Figure 3.15 Incident direct solar radiation on a south facing façade at solar noon in the optimal overhang day of past climate, PP (a); and future climate, FF (b). 64
Figure 4.1 Schematic representation of the four sequential steps 71
Figure 4.2. Aerial view with the open space used in the measured campaign highlighted (left), and interior view of the measured open space (right). 75
Figure 4.3. Characterization of cloud shading periods in four US cities: 1st column, number of days per year (Cloudy days represented in grey, sunny days in blue, and days with cloudy periods represented in grey and blue stripes); 2nd column, cloud duration (median value in blue); 3rd column, cloud starting hour (median value in blue); 4th column, average number of events per day considering only days with events. 85
Figure 4.4. Characterization of cloud shading periods in Lisbon. Cloudy days represented in grey, sunny days in blue, and days with cloudy periods represented in grey and blue stripes. 85
Figure 4.5 Total electrical load and occupation of the open space. 86
Figure 4.6 Air temperature measured during the demand flexibility event and simulated using the two modelling approaches 88
Figure 4.7 Results of the four demand flexibility scenarios for the 14th and 15th of May: Air temperature in the ground floor of South open space (1st row); fan coil cooling setpoint (2nd row); BIPV production by building floor area (3rd row); Electric grid demand (4th row); and accumulated electric grid demand (5th row). Gray areas corresponds to unoccupied periods. 90

List of Tables

Table 2.1 Weighting factors in different TMY methods [] 15
Table 2.2 Morphing transformation applied to the different weather variables. 17
Table 2.3 Differences between the standard office and the optimized office buildings. 19
Table 2.4 MAPD, MAD and bias of the average future seasonal temperatures (ºC): DJF (December, January, February), MAM (March, April, May), JJA (June, July, August), SON (September, November, December). 27
Table 2.5 MAPD, MAD and bias of the different temperature intervals between F-10Y and the four climate data files. 28
Table 2.6 MAPD, MAD and bias in heatwaves number, length and total number of days in a heatwave between multi-year data and the other climate data files. Average of the multi-year data is in brackets. 29
Table 2.7 MAPD, MAD and bias of annual heating energy consumption (Townhouse buildings) and annual HVAC electric energy consumption (Office buildings) between the multi-year data and the four climate data files 32
Table 2.8 MAPD, MAD and bias of peak heating energy consumption (Townhouse buildings), peak HVAC electric energy consumption (Office buildings) and the 99.6 percentile of the office buildings' electric cooling load between the multi-year data and the four climate data files 34
Table 2.9 MAPD, MAD and bias of the percentage of overheating hours during the occupied hours between the multi-year data and the other four climate data files. 36
Table 2.10 Interannual variability of the three BES outputs of the multi-year data of the historical and future data-sets for the four different buildings. 37
Table 3.1 EURO-CORDEX regional climate models considered in the present chapter, along with the responsible institution, the forcing global climate model, and the number of days in each model 45
Table 3.2 Impact of the daytime and nighttime shapes on different seasons, buildings, and regions. . 55
Table 3.3 Differences in the number of weeks in each temperature interval between past and future climates, averaged for each cluster regions. 59
Table 3.4 Average relative CDH reduction due to wind driven and night cooling ventilations in the four clusters for past and future climates. 60
Table 4.1 Building constructions and materials 76
Table 4.2 Internal mass objects, quantity, and material characteristics. 77
Table 4.3 EN 16798-1:2019 [49] thresholds for CO2 concentration, indoor operative temperature intervals, and ASHRAE Standard 55-2017 [50] thresholds for Drifts/ramps duration and respective operative temperature change. 82
Table 4.4 Capacitance of the Internal mass objects identified during the measurement campaign. 87
Table 4.5 Total and HVAC: electric energy demand, electric grid energy demand, and self-consumption for the four simulated models. Total BIPV production: 21 $Wh/m^2/h_o$. 90
Table 4.6 Percentage of time out of limits for the four comfort categories of indoor operative temperature and CO_2 concentration 92

Chapter 1 - Introduction

Climate change is one of the biggest challenges of contemporary society [1]. Between 1880 and 2020 the global average temperature has raised 1.2 ºC [2]. During the last decades, the warming rate and the number of heatwaves has increased [3]. The ongoing changes in air temperature and precipitation in different parts of the globe are already having consequences in worldwide energy use, economy and human health [1]. In Western Europe, the frequency of hot days has tripled, and the duration of heatwaves has doubled between 1880 and 2005 [3]. Future climate scenarios project an aggravation of these tendencies, projecting variable warming rates that result from different anthropogenic greenhouse gas (GHG) emission scenarios. In a business as usual scenario, a further increase of 4 °C is expected by the end of this century [4], accompanied by an increase in extreme temperature events [5]. This increase varies between regions of the globe, seasons [6] and time of day [7].

Existing future climate simulations indicate that existing annual and diurnal temperature cycles [8] will be reshaped, leading to increased air temperatures farther away from the typical summer months, occurring both earlier and later in the year [9,10]. To compound the problem, continuous urban development accentuates the effects of climate change in large urban areas due to the urban heat island effect [11, 12]. Buildings are one of the main GHG emitters, accounting for 50 % of the CO_2 emissions in the European Union (EU) [13], 43 % in the United States of America (US) [14] and over 50 % in China [15]. Buildings use approximately 40 % of the world's total final energy consumption [16]. In developed countries almost half of this energy is used in building heating, ventilation and air conditioning (HVAC) [17,18].

During the typical lifespan of 50 years or more, contemporary buildings will be subjected to a climate that will be progressively warmer and more volatile [19,20]. The combination of increased temperatures and continuously increasing building occupant comfort expectations and standards will lead to a higher cooling energy demand in commercial [21] and residential buildings [22]. To limit this increase, building designers are encouraged to use passive design strategies and passive cooling systems such as natural ventilation (NV), night cooling (NC), optimal control of solar gains, increased thermal insulation, airtightness and exposed thermal mass [23,24,25]. These strategies use the outdoor climate as a source of free or low energy cooling [26]. Unsurprisingly, the performance of these systems is highly dependent on weather, in particular air temperature, wind, solar radiation and humidity [27]. Thus, if buildings are not prepared and correctly designed for the changing climate there can be significant health risks

for the occupants, with exposure to high indoor temperatures potentially leading to heat strokes [28] or even death [29].

The impact of climate change on buildings has been studied for a wide variety of climates and building types [30,31]. Most studies focused on HVAC energy consumption and energy demand changes [20]. In most cases, these studies predict a decrease in heating and an increase in cooling energy consumption or demand [31]. In most regions around the globe, the total building HVAC energy consumption is expected to decrease in cold climates, remain constant in regions with cold winters and hot summers, and increase significantly in warm climates [30]. Most existing studies use simulation models of current buildings with current technologies in future climate. This approach may be inadequate since expected technology advances during 21st century (e.g. increase of the coefficient of performance (COP) of air-conditioning systems [32]) may have a higher impact than the calculated changes in energy consumption. The lifespan of building energy systems is 15-30 years [33] and most studies analyse the impact of climate change in the next 50-100 years with simulation models that use constant HVAC energy system efficiencies [34].

When studying the effects of climate change in buildings, building energy simulation (BES) is an essential support tool in the design and energy labelling/certification of new buildings. BES typically requires one year of hourly weather data which represents the climate in the building's location. Ideally, this one-year local weather data should be obtained from a long period of record (30 years), so that it can reflect the year-to-year weather variability. There are several methodologies for the difficult task of assembling a representative one-year hourly climate file from historical climate records [35]. The most commonly used methodology to produce current climate data files is called Typical Meteorological Year (TMY) [36]. TMY data are assembled by compiling the individual months which best correspond to the long-term monthly means of different climate variables. Typical meteorological year of future climate (F-TMY) is a TMY file obtained using a database of future climate.

Even though the use of single year weather data files is the common practice in BES, it often does not represent the long-term climate variability [37] but only the long-term monthly means. To reflect the full range of climate variability some studies recommend constructing more than one TMY, thereby encompassing the representation of climate extremes [38], or the creation of a range of synthetic weather time series from a base TMY that can evaluate the effects of climate variability in BES [39]. Single year weather data, like the TMY, should be created considering its end use. Several studies indicate that different weighting factors should be applied to

different weather variables depending on the application domain (e.g. global solar radiation for solar applications, wind profile for wind turbines [40] or, maximum and minimum temperatures for peak energy demand [41]). Further, since each month is chosen individually, TMY's are typically composed of months from different years, consequently discrepancies in the transition between months can occur. Still, several studies indicate that typical building operation is adequately simulated by single TMY file [38, 41 ,42].

In the short to medium term, and to reduce the environmental impact of the building sector, the EU wants to increase energy efficiency and onsite generation of renewable energy (RE), in particular, building integrated photovoltaic (BIPV). Unfortunately, increased use of RE creates new challenges to grid and building operators [43]. In the current context, grid stability concerns and existing economic interests create unattractive conditions for grid-injection of excess RE production. As a result, building integrated RE systems tend to be sized to meet a part of the building equipment and daytime lighting electrical loads, failing to use the full capability of onsite RE sources to also meet the full building electrical demand, including the variable energy demand for space heating, cooling and ventilation. An effective approach to increase the size and market penetration of BIPV systems is minimizing interaction between the building and the grid by increasing consumption of locally produced RE through a combination of building demand flexibility and building integrated energy storage [43].

There are several solutions for energy storage in buildings. The most common electrical energy storage approach, chemical batteries, is still too expensive for widespread application in buildings [44]. Alternatively, electric energy can also be converted into thermal energy and stored in two different systems: discrete/active storage (water tanks, passive change materials (PCM) and solid heat storage [45]), and in the building thermal mass (passive storage [46]). The first, uses excess energy to pre-heat or pre-cool thermally isolated water tanks (usually for short-term events) or PCMs (for longer events), to be used for intraday energy storage [45]. The second, building thermal mass as a battery (BaB), consists in thermal energy storage in the building thermal mass, typically performed by pre-heating the building interior. Energy stored in the BaB system can be released to meet short to medium term space heating energy demand. BaB systems can also be pre-cooled to meet space cooling energy demand in moments when the cooling system is turned off. Due to its widespread availability and nearly zero cost, BaB may be the most effective approach to activate building energy flexibility [47].

Flexible energy demand strategies defer or anticipate intraday building energy demand. Ideally, the shifts should have limited or no impact on occupant comfort and building operation. Services that must meet constant occupant demand such as lighting and office equipment, cannot be shifted [45]. As a result, the most commonly shiftable energy demands are domestic hot water (DHW) and space heating, ventilation and air conditioning. HVAC based flexibility is limited by thermal comfort and indoor air quality requirements of the occupants [48]. During flexibility events it is necessary to avoid excessively low or elevated indoor temperatures, sudden changes in temperature (drifts/ramps), and low indoor air quality (high concentration of pollutants, such as CO_2) [49, 50]. BaB energy storage can be used in combination with HVAC based flexibility to limit indoor temperature variations. There are two commonly used control strategies to activate building energy flexibility: rule-based controls (easier and simpler to implement) and model predictive control (more complex and costly but with potentially better results [51]). Demand flexibility can achieve different objectives: load shifting, peak shaving, reducing energy costs or increase consumption of RE. The energy flexibility potential of a given building, just like RE generation, depends on the climate. Existing studies show that buildings located in hot climates have higher RE generation capacities but shorter timespans for flexibility events, while buildings in cold climates have lower RE power generation capacities but may support longer events [52].

Thermal energy storage and demand flexibility can be combined to increase onsite RE use. Thus, when there is a surplus of BIPV production buildings can increase its HVAC consumption and store energy in the thermal mass (by pre-heating or pre-cooling the indoor space, within the limits of thermal comfort range), so that when a shortage of BIPV production occurs (e.g. by shading by passing clouds) reduce its HVAC consumption and allow the stored energy to be released without compromising thermal comfort. Clearly, the duration of flexibility events is limited by the ability to maintain acceptable indoor comfort conditions. Combining BIPV production with heat pump electric energy consumption benefits the building operators by increasing building self-consumption, decreasing exported energy to the grid (avoiding curtailments [53]) and grid consumption, and, last but not least, reducing energy costs [54]. In an ideal scenario the building is able to adjust HVAC consumption to better match BIPV production without compromising occupant comfort.

1.1 Research questions

This thesis addresses three complementary research topics that require high-resolution state-of-the-art climate data for both historical and future climate. In the first, a comparison of two methodologies used to produce future climate hourly data files for BES is performed, by simulating 2 residential and 2 office buildings in 14 cities in Iberia. Then, a detailed analysis of upcoming changes in temperature, their interaction with solar radiation, and the consequent impacts on passive building strategies is presented for the 43 most populated cities in EU. Finally, the effectiveness of using building thermal mass energy storage to offset temporary reductions in BIPV output due to passing clouds is analysed by measuring a demand flexibility event in a cooling dominated office building, modelling a calibrated thermal energy simulation, and simulating the office building during the cooling season in Lisbon. Additionally, cloud shading periods are analysed for different climates.

More specifically, this thesis investigated the following research questions:

1. Are the most commonly available climate data files, methodologies, and tools adequate for BES of future climate?
2. Can BES of future climate be performed using simple one-year climate data files?
3. What are the upcoming changes in the shape of the diurnal temperature cycle and their possible impact on thermal energy consumption in Europe?
4. When, where, and how passive design strategies (NV, NC, and solar shading) will be affected by changing climate, going beyond season or yearly effectiveness?
5. Can demand flexibility events (HVAC system turn off) be efficiently used to offset temporary reductions in BIPV production due to passing clouds?
6. What are the climate differences in the duration and time of occurrence of passing clouds that can impact BIPV production and trigger demand flexibility events?

1.2 Thesis structure

This thesis is divided in five chapters. The first chapter presents the introduction. Chapter 2 presents a comparison of different methodologies used to produce future climate data for BES, and is based on paper 1. Chapter 3 presents an analysis of the impact of upcoming climate change especially on passive building design strategies, and is based on paper 2. Chapter 4

presents a study to enhance building self-consumption, which will be necessary to achieve building energy positiveness on both present and future climates, by using BIPV production fluctuations, caused by passing clouds, to trigger building demand flexibility events (based on paper 3). The last chapter, Chapter 5, presents the final general conclusions of this thesis.

Chapter 2 - Comparison of methodologies for generation of future weather data for building thermal energy simulation

2.1 Introduction

The most commonly used method to produce future climate data files for BES is Morphing [55]. This approach uses the changes in future weather monthly averages to stretch, shift, or stretch and shift existing TMY files, creating Morphed TMYs. This method relies on delta change in monthly averages to characterize future weather, yet, several studies indicate that weather variability and extreme events are not reproduced by variations in monthly means [56]. Further, Morphing and F-TMY are different in their treatment of temporal coherence between weather variables. Due to its simplified approach Morphing introduces the effects of climate change independently between variables, while F-TMY files use unmodified simulated data that maintains temporal coherence between the different weather variables. In light of these limitations, it is important to evaluate the suitability of Morphed TMY files for future BES studies.

This chapter presents a comparative study of two methodologies used to produce future climate hourly data files for BES: Morphing (the simplest approach), and F-TMY. The study includes a sensitivity analysis of applying Morphing to different data files and climate projections, and is unique in its comparative approach and in the use of a high-quality regional climate model database, spanning 10 years of historical and future hourly data (the 90's, in the 20th and 21st centuries), as the reference approach for BES of future weather. This future simulated weather database was produced using a high-resolution (9 km) Weather Research and Forecasting (WRF) atmospheric model, covering the Iberian Peninsula with a RCP8.5 emissions scenario. This database is used to produce a F-TMY and a high-quality Morphed file. In addition, the comparison included two Morphed data files produced using publicly available weather data files and a commonly used morphing tool. The first uses the WRF simulation of future climate to Morph common available TMY files from the EnergyPlus database [57]. The second uses the same TMY files from the EnergyPlus database and applies them to the CCWorldWeatherGen tool [56], which is the most commonly used tool to produce Morphed TMY files.

This chapter analyses the impact of each type of future weather file in the BES predictions of annual energy and peak energy consumption for space heating, cooling and ventilation of 2

office buildings and 2 townhouse buildings for 14 cities in Iberia. Furthermore, it compares the variability of the BES results between the historical and future datasets. This chapter has two main objectives: to determine if BES of future climate can be performed using simple one-year climate data files; and investigate if morphed climate data files produced using commonly available climate data files and tools are adequate for BES of future climate.

The next section (2.2) presents a literature review of the weather data used in building energy simulation. The following section (2.3) presents the methodology used to produce the weather data files and the BES. The last two sections present the results and the discussion (2.4), and the conclusions (2.5).

2.2 Weather data for building energy simulation

This section begins with a brief discussion of the methodologies used to generate TMY files. The following subsection presents future climate projections used in this chapter. The next section reviews existing studies that used Morphed TMY files for BES. The final subsection focuses in other studies that use outputs from future climate projections for BES.

2.2.1 Typical Meteorological Year

The TMY methodology was introduced in 1978 [36] and consists of the selection of twelve typical months from 30 years of hourly data to assemble one year of representative weather data for a given location. The twelve typical months are selected by statistical analysis of 9 different variables using different weighting factors used to rank the 30 months that are available for each month. In 1994, the TMY method was updated (TMY2 [58]), with the introduction of a new variable and adjusted weighting factors. In 1997, an initiative called International Weather Year for Energy Calculations (IWEC) created climate data using the TMY methodology with updated weighting factors. [59]. This dataset was updated in 2008, TMY3 [60], using 15 years of data to assemble the files. Recently, a new set of TMY were created for Europe, with two different baseline periods: the first considering the whole period of record, and a second considering the most recent 15 year (2003-2017) [61].

2.2.2 Future climate

Current state-of-the-art approaches to produce future global climate projections are based on the General Circulation Models (GCMs). This model is used by several research groups in coordinated climate model numerical experiments. This research effort is known as the Coupled Model Intercomparison Project (CMIP5) and is currently in its fifth generation. In CMIP5 different simulations of past and future climates are performed to advance and increase the robustness of climate change knowledge [62]. CMIP5 projections are grouped according to the emission and concentration scenarios used to represent the 21st century. These scenarios, called Representative Concentration Pathways (RCPs), are based on socio-economic, technological, energy, land use and cover, emissions of GHG and air pollutant assumptions [63]. There are four RCPs, representing a full range of concentration scenarios existing in the literature. Using different climate models and RCPs, different scenarios are simulated from 1850 to 2100 and, in some cases, until 2300 [63]. In each of the four RCPs a radiative forcing, or increase from background radiation, is defined for the year 2100: 8.5 W/m^2, 6 W/m^2, 4.5 W/m^2 and 2.6 W/m^2. In light of the increasingly effects of climate change and the difficulties in emission reduction, RCP 8.5 is often used in long-term climate change impact studies [64, 65].

The result of CMIP5 is a dataset of future global climate with a typical horizontal resolution of ~100km. GCMs are able to capture well the large-scale atmospheric variability but unable to represent well finer scale processes, which are crucial to simulate local climate, precisely where climate change is mostly felt. To overcome this discrepancy, GCM results are used to force regional climate models (RCMs), at much higher resolutions (~10 km), for smaller regions of the world [66]. The use of dynamically downscaled data given by RCM's allows for increased ability to capture smaller scale processes and to study the effects of climate change at local scales, indoor [67] and outdoor [68]. The output of the different GCM and RCM constitute a wide range of climatological results with different spatial and time resolutions [69]. The output of the GCM and RCM have been used in the last years to produce future weather data that can be used in BES [35]. However, BES requires hourly data and the great majority of the output of GCM and RCM are daily averages of changes in weather variables, compared to a baseline period.

2.2.2.1 Morphing

The most common methodology used to produce future weather data for BES is called Morphing [55]. Several BES studies have been performed using Morphing for residential and commercial buildings [70]. The methodology consists in using predicted future monthly changes outputted by GCM to shift, stretch, or shift and stretch the present weather data, usually an existing TMY file. A tool, named CCWorldWeatherGen, was developed to facilitate the application of the Morphing procedure to current weather data files [71, 56]. This tool has been used in BES based studies of future climate [72, 73]. However, climate change projections used in this tool are not state-of-the-art and are based on the previous Intergovernmental Panel on Climate Change (IPCC) report (fourth assessment report) [74]. The Morphing methodology can reflect changes on the average weather conditions but is unable to model changes in the weather patterns (daily, weekly, monthly or yearly) and extreme events of the different weather variables are not available in a Morphed file. To address the lack of variability, a recent study [75] applied Morphing to individual years. The study concluded that the year-to-year variability in the Morphed data files was large, which is in line with the current understanding of climate change [75]. However, the approach of Morphing several years was not able to capture extremes and changes of atmospheric patterns. A study using results of an RCM with a 25 km grid for a city in Denmark, compared the effect of using the Morphing methodology based on annual, monthly and hourly changes in values of air temperature [76]. This concluded that there were no significant differences in the energy consumption of a building using three different time resolutions as inputs to the Morphing methodology.

2.2.2.2 Generating weather data files from RCM outputs

The use of RCM simulations to generate weather data for BES has been previously reviewed [77, 78]. RCM are expected to provide an accurate representation of the atmospheric processes that are affected by local topography and thermal contrasts, and therefore describe the spatial and temporal variability of local climate [79]. These variabilities are typical associated with microclimates, which can have significant impact on BES in urban environments, where differences between city centres and rural areas are commonly accentuated [80]. A study focused on the importance of spatial resolution concluded that the need for high-resolution grids is location dependent since different regions show different spatial weather variabilities [81]. A comparison of BES predicted temperatures inside and outside an attic using RCM data with 25 km and 50 km grids, concluded that the increased spatial resolution had only a significant

impact on the extreme values of temperature [82]. A similar study comparing the impact of using a 60 km grid GCM or a 2 km grid RCM concluded that using the finer grid allowed the representation of both regional characteristics and local climate change for the two variables studied (temperature and specific humidity [67]). With the goal of reducing the number of simulations of future climate without neglecting year-to-year variability, a study proposed a method to synthetize three different weather data files based only on air surface temperature: one representing the typical climate and two representing the extremes (one cold and one warm) [78]. The study concluded that using the three weather data files enables the consideration of the extremes and the variations of the original data [78]. More recently, the same methodology was used and compared against other future weather data, for the city of Genève and using 16 ASHRAE buildings. The study showed that all methods (including Morphing) were able of capturing the long-term average impacts of climate change. Although, peak energy consumption associated with cooling demand was only correctly assessed when using the three weather data files [83].

2.3 Methodology

This section begins with a description of the reference WRF climate data set used in this chapter. The following subsections describe the methodologies used to produce the climate data files used. The section ends with a description of the BES models, data analysis methodology and limitations of the present study.

2.3.1 Climate data

This chapter focuses on Iberia, a region that encompasses very diverse climates, from the cold and wet northern regions to the semi-arid warm and dry areas in the south [84]. Furthermore, the Mediterranean, and in particular Iberia, were identified as highly vulnerable to global warming, with projections of large increases in temperature and reductions in precipitation [85]. The data used in this work focus on 14 of the 15 most populated metropolitan regions in Iberia [86]: Madrid (MAD), Barcelona (BAR), Lisbon (LIS), Valencia (VAL), Sevilla (SEV), Alicante (ALI), Porto (POR), Malaga (MAL), Murcia (MUR), Bilbao (BIL), A Coruña (COR), Oviedo (OVI), Zaragoza (ZAR), and Granada (GRA) (Figure 2.1), Vigo was excluded due to

the nonexistence of a TMY on the EnergyPlus database [57]. Although, most cities are located in coastal areas, they represent different climate regions in Iberia. The climate data used in this chapter can be divided into two different categories: data from the high-resolution climate simulations, and data commonly available for building energy simulation (Figure 2.2). The high-resolution climate simulation dataset resulted in the following five weather data files:

1. P-10Y: a 10-year file of past hourly data (1990-1999);
2. P-TMY: a past TMY file, produced using P-10Y (1);
3. F-10Y: a 10-year file of future hourly data (2090-2099);
4. F-TMY: a future TMY file, produced using F-10Y (3);
5. M-TMY: a morphed TMY file, produced using P-TMY (2), and differences between F-10Y (3) and P-10Y (1).

The second group of data uses freely available climate data files and a morphing tool that are commonly used for BES of future climate, resulting in three weather data files:

6. EPL-TMY: past TMY download from EnergyPlus weather database [57];
7. M-EPL: a morphed EPL-TMY, produced using EPL-TMY (6), and differences between F-10Y (3) and P-10Y (1).
8. M-CCT: a morphed EPL-TMY, produced using EPL-TMY (6), using the CCWorldWeatherGenerator tool [56];

The high-resolution climate simulations were performed using the WRF atmospheric model [87] with 9 km spatial resolution. The model set up description is detailed in [79, 88, 84]. The boundary lateral forcing for the climate change runs are taken from an EC-EARTH v2.3 [89] climate simulation, in agreement with the RCP8.5 scenario, and encompassing two periods: 1971–2000 and 2071–2100. The present and future simulations constitute the highest resolution and finest temporal sampling available to study the Iberian climate [66]. The hourly temporal resolution of present and future climates provided by the WRF model is a valuable and rarely available output of RCM.

The WRF simulations were performed using the following set of physical parameterizations: the microphysics WSM 6 class single-moment (mp6) scheme by [90], the planetary boundary layer scheme of Mellor-Yamada-Janjic [91], the Betts-Miller-Janjic cumulus scheme [92, 93, 94, 95, 96], the Noah LSM 4-layer soil temperature, soil and canopy moistures model [97] and

the radiation scheme used relies on the shortwave and longwave schemes [98] of the NCAR Community Atmospheric model. The land use and land cover data were taken from the U.S. Geological Survey.

The WRF model results were extensively validated for inland surface variables, namely, temperatures and precipitation in Portugal [79], Iberian precipitation [84], and wind [99]. In the present chapter, two different periods, historical (1990-1999) and future (2090-2099) are used. The simulation grid point from the RCM chosen to represent each city was the inland point closest to the city centre. The model outputs used to create the weather data for BES were (hourly data): dry-bulb temperature, wind speed and direction, specific humidity, and radiation (direct and diffuse).

Figure 2.1 Fifteen biggest metropolitan regions in Iberia [100]

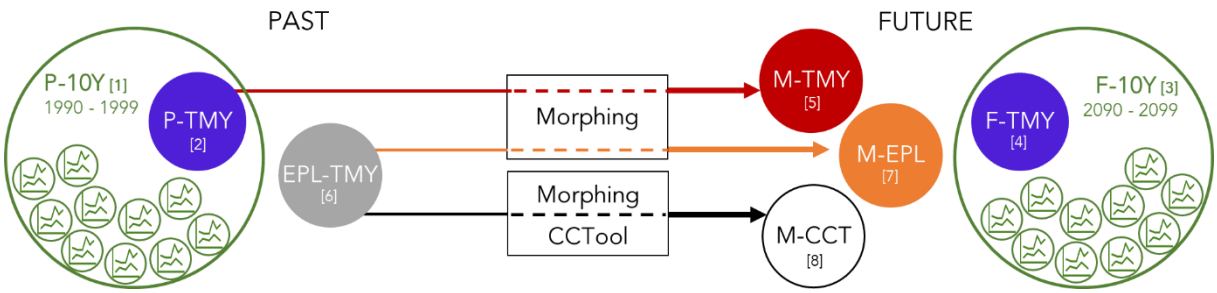

Figure 2.2 Schematic representation of the different climate data files

2.3.1.1 TMY

For a given location and range of available weather data, 10-30 years, a TMY weather file is obtained by assembling a set of representative calendar months, typically taken from different years in the multi-year dataset. The selection of the representative month is based on statistical analysis of nine weather variables: daily maximum, minimum and mean dry bulb temperature and dew point temperature, daily maximum and mean wind speed, and daily total global horizontal radiation for everyday of the data set. These variables are separated by month and, for each variable, a long-term cumulative distribution function (CDF) and short-term CDFs are calculated. The long-term CDF uses one month of the full set of years, while the short-term CDF uses data from one month of just one year. The CDF for each variable is calculated by:

$$S_{ne}(x) = \begin{cases} 0, & x < x_{(1)} \\ \frac{ko-0.5}{ne}, & x_{(ko)} \leq x \leq x_{(ko+1)} \\ 1, & x \geq x_{(ne)} \end{cases} \qquad (2.1)$$

where ne is the total number of elements and ko is the ranked order number (ko=1, 2, 3, …, ne-1). Next, the difference between the short-term CDFs and the long-term CDFs is measured and calculated using Finkelstein-Schafer statistics (FS):

$$FS = \frac{1}{m}\sum_{ko=1}^{m} \delta_{ko} \qquad (2.2)$$

where m is the number of days during the month and δ_k is the absolute difference between long-term CDF and short-term (month under study) CDF at x_i.

For each month of each year, 9 different FS are obtained, one for each weather indices. A weighting factor (W) is applied to each variable (j) of the month, resulting in the weighted statistics (WS) for the month:

$$WS = \sum_{j=1}^{9} W_j (FS)_j \qquad (2.3)$$

This chapter uses the weighting factors proposed by IWEC [59], shown in Table 2.1.

Table 2.1 Weighting factors in different TMY methods [101]

Weather Index	TMY [36]	TMY2 [58]	IWEC [59]
Maximum dry bulb temperature	1/24	1/20	5/100
Minimum dry bulb temperature	1/24	1/20	5/100
Mean dry bulb temperature	2/24	2/20	30/100
Maximum dew point temperature	1/24	1/20	2.5/100
Minimum dew point temperature	1/24	1/20	2.5/100
Mean dew point temperature	2/24	2/20	5/100
Maximum wind speed	2/24	1/20	5/100
Mean wind speed	2/24	1/20	5/100
Total horizontal solar radiation	12/24	5/20	40/100
Direct normal solar radiation	-	5/20	-

In the next step of the process, the five candidates for each month are chosen by selecting for every calendar month, the five months with the lowest WS values (the lowest deviation from the long-term CDFs). In the case of February, only non-leap years are used as typical meteorological months, although leap years are considered for the calculation of the long-term CDF, as recommended [60]. The long-term mean and median of the WS are calculated and the five candidate months are ranked according to its closeness to the statistical values.

Next, six criteria related with persistency are calculated for the five candidate months: consecutive days with mean daily dry-bulb temperature above the 67th percentile, consecutive days with mean daily dry-bulb temperature below the 33rd percentile and consecutive days with daily total solar radiation below the 33rd percentile. For each of the criteria two values are obtained: the length of periods of consecutive days and the number of periods of consecutive days. With this information, the month with the longest period, the month with the largest number of periods, and months with zero periods of consecutive days are eliminated. If two or more months are equal, both are eliminated. The month chosen as the typical month is then selected, from the remaining months, considering the one that is closest to the long-term mean and median of the WS. If all candidate months are eliminated by the persistency criteria, the closest to the long-term mean and median of the WS is the one selected.

Finally, the 12 selected months are assembled to obtain one-year TMY file. To avoid discontinuities and large changes between the beginning and ending of the months, a cubic

spline curve fitting technique is applied to the last and first 6 hours of each month. Using this methodology two different TMY were created for each city using the high-resolution climate data: one for the historical (P-TMY) and another for the future (F-TMY).

The EnergyPlus website presents an extensive database of climate data files for BES [57]. However not every file was constructed following the same TMY methodology, and different files can be based on different baseline periods. For Iberia, the climate data files available in the EnergyPlus database are based on the same methodology [102] or are IWEC data files [59]. For each city understudy a TMY climate file was downloaded (EPL-TMY) to be used in the creation of M-CCT and M-EPL climate files.

2.3.1.2 Morphed TMY

To generate a Morphed TMY file [55] it is necessary to use the calculated TMY for the historical period (P-TMY) and the monthly climate change signal of different variables. In this chapter, the signal is obtained by calculating the monthly differences between future (F-10Y) and historical (P-10Y) climates. Morphing consists of shifting, stretching or a combination of both, of the weather variables in an existing TMY file. The shifting and stretching magnitudes are based on the predicted variations in future mean values of each climate variable. A shift is applied when, for a given variable, absolute changes are predicted to occur:

$$x = x_0 + \Delta x_m \qquad (2.4)$$

where x is the morphed climate variable, x_0 is the present-day climate variable, Δx_m is the projected absolute change in monthly mean for the month, m.

A stretch is applied when relative changes are predicted to occur:

$$x = x_0 \times \alpha_m \qquad (2.5)$$

where α_m is the fractional change in the monthly mean.

A combination of shift and stretch is applied when both relative and absolute changes are predicted to occur:

$$x = x_0 + \Delta x_m + \alpha_m \times (x_0 - \langle x_0 \rangle_m) \qquad (2.6)$$

where $\langle x_0 \rangle_m$ is the monthly mean value of the climate variable. Table 2.2 shows the transformation used in each weather variable.

Table 2.2 Morphing transformation applied to the different weather variables.

Weather Variable	Shift	Stretch	Shift and stretch	From morphed variables
Dry bulb temperature	-	-	✓	-
Dew point temperature	-	-	-	✓
Horizontal radiation	-	✓	-	-
Diffuse radiation	-	✓	-	-
Direct radiation	-	-	-	✓
Relative humidity	-	✓	-	-
Atmospheric pressure	✓	-	-	-
Wind speed	-	✓	-	-
Cloud cover	✓	-	-	--
Illuminances	-	-	-	✓

After morphing each variable, a cubic splines curve fitting technique is applied on the last 12 hours and the first 12 hours of each month to eliminate discontinuities created with the Morphing procedure.

The morphing procedure, based on the monthly differences between the high-resolution historical (P-10Y) and future (F-10Y) databases, is applied to both Past TMY (P-TMY), the one created based on the high-resolution historical data (P-10Y), and the TMY downloaded from EnergyPlus database (EPL-TMY), resulting in the M-TMY and M-EPL, respectively.

2.3.1.3 CCWorldWeatherGen tool

The CCWorldWeatherGen tool [56] uses the previous described morphing methodology to produce future weather data files for locations all over the world. This tool uses the UK Met Office Hadley Centre Coupled Model 3 (HadCM3) [103] GCM simulations as input for the morphing procedure. The HadCM3 is based on the A2 (business as usual) climate projections of IPCC fourth assessment report [74], which correspond to a previous version of the RCP8.5 projections [1, 104]. HadCM3 uses a grid resolution of 2.5º x 3.75º, corresponding to a total of

8 grid cells in Iberia. The climate delta changes outputted by the climate model are available for three different periods: 2020, 2050 and 2080, considering a baseline climate between 1961-1990. The input TMY files used in this study with the CCWorldWeatherGen tool are the TMY files downloaded from EnergyPlus database (EPL-TMY) and the CCWorlWeatherGen tool is used to produce morphed files for the year 2080 (M-CCT).

2.3.2 BES methodology

The BES were performed with the US DOE open source software EnergyPlus. BES results depend on many parameters and, it is beyond the scope of this chapter to analyse the impact of the weather data files on all possible BES scenarios. In this context, this chapter used four models that span two building types and two levels of envelope quality:

1. Standard office building
2. Optimized office building
3. Standard townhouse
4. Optimized townhouse.

2.3.2.1 Office Buildings

The standard office building consists on a variant of the Medium Office Model of the Standard United States Department of energy Commercial Reference Buildings dataset [105]. This model was validated in a previous study [106]. The optimized version of this model office building was based on the methodology used by [106] and is shown in Figure 2.3. Regarding the use of these office buildings in Europe, globalizations means that the designs are, to some extent, generic across the globe and the same model has been used in previous studies [83, 107, 108]. The building complies with the American legislation, but not all the building input parameters are exclusive of this country. Furthermore, the origin of the office buildings is California, which has a climate similar to Iberia (Mediterranean [109]).

The standard office building was optimized to enhance its passive thermal behaviour and the equipment efficiency, resulting in a decrease of the HVAC energy consumption between 60 % and 75 % [106]. Table 2.3 shows the changes between the standard office and the optimized office buildings.

The building management system alternates between NV or mechanical ventilation during working hours (8 h to 18 h from Monday to Friday). NV is used to cool the building when the outside temperature is above 10 ºC and below the zone temperature. NV is modelled using the EnergyPlus ZoneVentilation:WindandStackOpenArea model, which considers both wind and stack effect. The opening area (A_{open}) is calculated as function of the outdoor air temperature (T_{out}) for each timestep using Equation 2.7 [110,106] with a maximum window openable area ($A_{open,max}$) of 5 % of the gross floor area. Mechanical ventilation (HVAC) is only used when the outside conditions do not allow NV. NV is also available during unoccupied hours with the same constrains of the occupied hours in order to perform night cooling. The air renewal is 8.5 m^3/hour/person and 1.1 m^3/hour/m^2. An average fan efficiency of 50.1 % and a heat pump efficiency of 40 % are considered. The coefficient of performance (COP) varied with the outside temperature in each simulation timestep. The heating and cooling setpoints are 20 ºC and 26 ºC, respectively. A heat recovery system with 80 % efficiency is installed in this optimized building [108].

$$A_{open} = A_{open,max} \times (0.0242 \times (T_{out} - 273.15) - 0.037) \quad (2.7)$$

The infiltration rate consider is 0.0136 m3/(s m^2), when HVAC is turned on it is only 25 % of its original value. In the office zone occupation is 11.6 m^2 per person. The furniture internal mass is 2*0.1 cm/m^2. The office equipment power density during the occupied hours is 9.74 W/m^2 and on unoccupied hours of 2.80 W/m^2. The lighting power density consider is 8.07 W/m^2 in the office zones and 6.46 W/m^2 in the other zones. During unoccupied periods the light power density is 25 % of the occupied hours.

Table 2.3 Differences between the standard office and the optimized office buildings.

	Standard office	Optimized office
Hybrid Natural Ventilation	✗	✓
Shading fin	✗	✓
Windows	Default	Double glazing w/ low emissivity
Lighting	Default	8.07 W/m^2
Fan efficiency	40. 0 %	50.1 %
Heat pump efficiency	30 %	40 %
Heat recovery system	✗	80 %

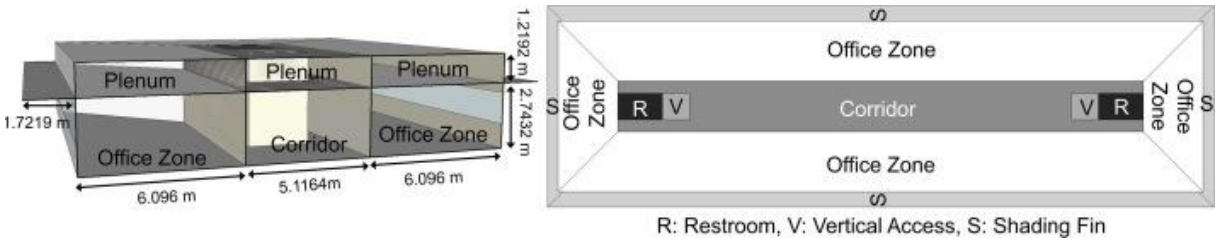

Figure 2.3 Building simulation model section cut and zones [106].

2.3.2.2 Townhouse Buildings

The residential building used in this chapter is a townhouse (Figure 2.4) with total floor area of 141 m^2, 3 bedrooms and a total of 5 occupants. The building model used was previously validated [111]. The main characteristics of the standard townhouse are the windows with 3 mm double glazed with 13 mm of air cavity, internal shading in the living room, kitchen and in the bedrooms, and the infiltration is 0.65 air change per hour (ach). Heating is provided by a boiler with 85 % efficiency. The heating setpoint is 20 ºC during the day and evening, and 15 ºC overnight. In fact, townhouse buildings are not as common in Iberian as in the Netherlands (22 % of the residential building stock in Spain, 17 % in Portugal and 35 % in the Netherlands [112]) and do not have exactly the same building construction specification. However, considering buildings built in the 70's in the Netherlands and the one's built in Portugal and Spain in the 70's and 80's, the U-value requirements are quite similar [113]. So, to some extent, buildings built during these periods in the three countries have some commonalities.

The optimized townhouse building was developed by [111]. The optimization consists in four modifications of the original standard townhouse. The first, is the refurbishment of the building envelope, with the addition of thermal insulation on the walls and roof (50 mm thick insulation with 0.03 W/(m k) of thermal conductivity) and upgrading of the windows with the addition of a low emissivity coating on the outside part of the inner glass (light transmittance of 55 % and infrared emissivity of 0.06). The second, consist in the increase of the airtightness of the building by adding mechanical ventilation and heat recovery system which allows the reduction of the infiltration to approximately 0.06 ach, which is similar to the Passive House standards. The third modification is the substitution of the existing boiler by a newer and more efficient one with 98 % actual performance. The fourth is the assumption of a more efficient occupant behaviour, which implies the reduction of the number of NV periods during winter. The first and second modifications combined allowed a reduction of the heating gas consumption of 59 %. Adding the third modification (boiler replacement) allowed a heating gas consumption

reduction of 65 %. Including the fourth modification allowed a total reduction of 86 % of the heating gas consumption [111].

Figure 2.4 Townhouse building and floor plan [111].

2.3.3 Data analysis

Quantitative evaluation of BES simulation results are based on bias (Equation 2.8), mean absolute difference, MAD, (Equation 2.9) and mean absolute percentage difference, MAPD, (Equation 2.10):

$$bias = \frac{1}{n} \times \sum_{i=1}^{n} (\hat{Y}_i - Y_i) \qquad (2.8)$$

$$MAD = \frac{1}{n} \times \sum_{i=1}^{n} \left| \hat{Y}_i - Y_i \right| \qquad (2.9)$$

$$MAPD(\%) = \frac{\sum_{i=1}^{n} |\hat{Y}_i - Y_i|}{\sum_{i=1}^{n} Y_i} \times 100 \qquad (2.10)$$

Where n is the number of cities, and Y_i and $\hat{Y}_i$ are, respectively, the reference value (multi-year average, F-10Y) and the value obtained with the other methodology (F-TMY, M-TMY, M-EPL or M-CCT). The first parameter gives information about systematic differences (systematic underprediction or overprediction) and the last two parameters give information about the mean difference between the methods.

Climate analysis begins with a comparison of the mean outdoor season temperatures. Then, the outdoor temperature during the day (between 9 am and 6 pm) was assessed by dividing the outdoor temperature into four different intervals:

- Cold hours ($T \leq 10$ ºC);
- Suitable for natural ventilation/fresh air supply ($10 < T \leq 16$ ºC);
- Suitable for ventilative cooling ($16 < T \leq 26$ ºC);
- Warm hours ($T > 26$ ºC).

This threshold for cold hours, 10 ºC [114], is the minimum temperature in which people start to open windows for fresh air. The last group, too warm, is defined as the temperatures when is too warm outside to use the external conditions for natural ventilative cooling. The temperature limit considered was 26 ºC [115]. Inside the temperature band (10 ºC to 26 ºC), the temperatures were divided into two different categories. The first was named NV and is between 10 ºC and 16 ºC (inclusive) and was considered the range when the outside air could supply the interior of the building with fresh air to keep a good indoor air quality (AIQ). The temperatures between 16 ºC and 26 ºC (inclusive) were considered as ventilative cooling. This means that outside conditions could be used to provide fresh air (e.g. through the opening of windows, [116, 114] state that the percentage of window opening starts to increase at 15 ºC, conservatively we used 16 ºC) which can be considered natural ventilation or using mechanical ventilation which can be used to provide IAQ, remove heat gains and/or maintain/increase the thermal comfort [117]. For the calculations of the different temperature groups, a typical working hour of a commercial building was considered, between 9 am and 6 pm. The focus is on commercial buildings because there has been a rising tendency in the cooling energy demand, during the last decades, especially in these type of buildings [118].

The number of daytime hours in each interval were calculated for the multi-year data, and for the four climate data files for all cities. The multi-year data was then averaged to calculate the average potential in these cities. Next, for each city, the multi-year average was compared against the F-TMY, M-TMY, M-EPL and M-CCT climate data files and the differences were calculated.

After the temperature analysis, the number and persistency of heatwaves was assessed. This analysis uses the World Meteorology Organization [119] definition: more than five consecutive days with local maximum temperature above the 90^{th} percentile of the historical dataset. For

each single year future weather file, the number of heatwaves, the average duration in days (persistency), and a combination of both named total heatwave days were calculated and compared against the multi-year data average; acknowledging the simplification linked to the computation of heatwaves in a single year setting.

To compare the BES results from the different weather data files for the two office buildings the predicted electric energy consumption associated with heating, cooling, and ventilation of the building on an annual basis and the peak energy consumption were used. Additionally, building cooling load at the 99.6 percentile was calculated. This value is used for sizing of HVAC units and is an alternative to the cooling design day method proposed by ASHRAE [120]. Ideally, the 99.6 percentile peak cooling load should be obtained using multi-year simulations. Yet, in the present case the calculation of this peak cooling load method will, in most cases, use single year weather data files. This approximation will allow for a comparative assessment of the impact of the different weather generation methods on this design parameter. For the townhouses, the comparison used the annual energy consumed and the peak energy consumption of the boiler. Since these buildings do not have a cooling system the number of overheating hours was calculated for the summer months during the occupied hours (between May and September). The overheating hours were assessed using operative temperature obtained as an output of EnergyPlus and considering the adaptive comfort levels for naturally conditioned spaces defined by ASHRAE's standard 55 [50]. The overheating hours were calculated for the living room, kitchen, bedrooms and the west room of the attic, which is considered a bedroom, during the occupied period. In order to better analyse the results, the overheating hours in percentage were calculated. The degree of overheating was not calculated in this study. In this chapter only the thermal energy consumption is assessed since the remaining energy consumption of the four buildings is not weather dependent (including lighting, which functions independently of the available daylight).

Finally, using the same BES results, the year-to-year variability of the multi-year data was assessed, both for historical and future datasets. To quantify the variability, the coefficient of variation (CV) was calculated. CV is a ratio between standard deviation and the mean value for each city. For each variable and building type, this coefficient was calculated using the following expression:

$$Coefficient\ of\ variation\ (\%) = \frac{1}{n} \times \sum_{i=1}^{n} \frac{\sigma_i}{Y_j} \times 100 \qquad (2.11)$$

Where n is the number of cities, and σ_i and Y_j are the standard variation and mean values of the multi-year data.

2.3.3.1 Limitations of the present chapter

This chapter has three main limitations. The first is the choice of reference and its implications in the level of agreement found in the results. The reference is the output of a state-of-the-art RCM for Iberia, which had the highest resolution and finest temporal sampling available [66]. Two of the weather data files (F-TMY and M-TMY) are directly obtained from the reference dataset, consequently a better agreement between these two weather files and the reference is expected.

The second limitation is the use of CCWorldWeatherGen tool to morph commonly available TMY files (EPL-TMY). This means that the resulting morphed files (M-CCT) are produced considering a different baseline than the one used by the tool (up to 1999 instead of 1961-1990), and for a different future than the reference data (2080's vs 2090's). However, this limitation is often ignored in climate change BES studies where the morphing method is used without an adequate reference climate.

The third limitation is the use of 4 different buildings (2 offices and 2 townhouses), that do not represent the full spectrum of commercial and residential buildings, and do not consider the impact of different use patterns, changes in solar heat gains and in internal heat gains independently. However, consistent results in the considered buildings can be the basis for a future extensive study spanning wider building types. Such study could focus on the impact of building usage patterns and heat gains across different climates.

2.4 Results and discussion

This section presents and compares the results of the climate analyses and BES. The analysis focuses on the differences (MAPD and MAD) and bias of the four different future climate data files, to the reference (multi-year data, F-10Y). The analysis of the projected changes for climate and energy consumption for the future is out of the scope of this chapter, since it has previously been assessed in other studies [121, 122].

A preliminary validation analysis using the historical dataset (P-10Y) was performed focused on the TMY produced using this dataset (P-TMY). This analysis revealed a good agreement between the two datasets (MAPD below 10 % except for the cold hours, which have high

percentage differences but small absolute differences) and BES (average MAPD of 7 %). This agreement gives a good indication that the TMY method is correctly applied and that it is appropriate for BES use with historical climate data.

2.4.1 Temperature analysis of future climate data files

Since air temperature is one of the variables that most affect building thermal energy consumption and is one of the most affected by climate change, the objective of this section was to assess differences in air temperature in the weather data files. With this analysis it is possible to better understand the BES results that are presented in the following section (2.4.2). Furthermore, preliminary studies focusing on the building site climate are often performed before BES [123] and can impact design choices by engineers and architects.

The results of the seasonal temperature analysis of the end of the 21st century are shown in Figure 2.5 and the differences in Table 2.4. From these results it can be seen that F-TMY, M-TMY and M-EPL are capable to reproduce the mean seasonal temperatures across all cities, while M-CCT cannot. Both F-TMY, M-TMY and M-EPL use the multi-year data (P-10Y and F-10Y) to produce the future climate data files, while M-CCT is based on a different dataset with a coarser grid resolution, older climate models and a different baseline climate. However, such an agreement between the F-10Y and M-EPL is unexpected, since the morphing procedure was applied to an existing TMY file (EPL-TMY) that was not created with the same database and/or timeframe of the multi-year data. The biggest differences to F-10Y are found with M-CCT climate data files with a significant overprediction bias (over 2 ºC in JJA and SON), leading to systematic higher seasonal temperature across all cities. According to the current understanding of climate change, M-CCT temperatures are expected to be lower to the temperatures in F-10Y, since M-CCT projections are for the 2080's considering a baseline 1961-1990 (even considering that the EPL-TMY already has some climate change incorporated, since it uses data up until 1999), while multi-year projections are for 2090-2099. The reason why we can expect temperature underestimation is that the RCP8.5 scenarios project higher rates of temperature increase in the last decade of 21st century compared with the 20th century [1]. However, this does not occur, and there is temperature overestimation by M-CCT. A possible explanation can be the previously mentioned incorporation of climate change in the EPL-TMY files relative to the baseline (1961-1990). Additionally, the coarser grid resolution, which is less capable of reproducing the influence of the ocean, namely thermal driven circulations, and the older climate change projections (A2 scenario). The multi-year data uses

a high-resolution grid with the most advanced climate change projections, while M-CCT uses a low-grid resolution (each cell represent hundreds of km) with outdated climate projections.

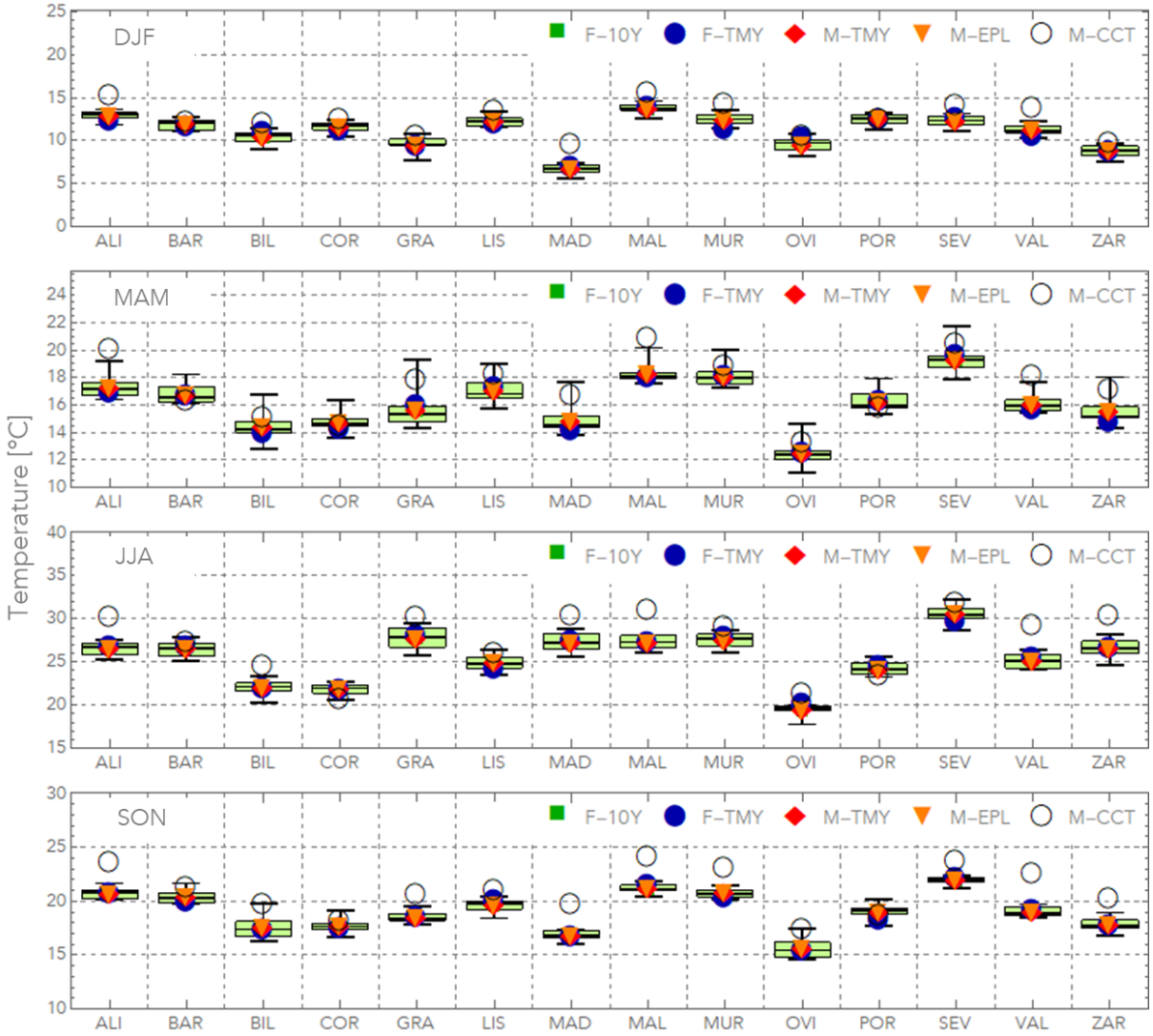

Figure 2.5 Average future seasonal temperatures (ºC): DJF (December, January, February), MAM (March, April, May), JJA (June, July, August), SON (September, November, December). Boxplots of F-10Y with green dark dots representing the mean of F-10Y, in blue F-TMY, in red M-TMY, in orange M-EPL and in white M-CCT.

Table 2.4 MAPD, MAD and bias of the average future seasonal temperatures (ºC): DJF (December, January, February), MAM (March, April, May), JJA (June, July, August), SON (September, November, December).

	DJF (ºC)			MAM (ºC)			JJA (ºC)			SON (ºC)		
	MAPD	MAD	Bias	MAPD	MAD	Bias	MAPD	MAD	Bias	MAPD	MAD	Bias
F-TMY	3 %	0.4	+ 0.0	2 %	0.3	- 0.1	2 %	0.4	+ 0.2	1 %	0.2	+ 0.0
M-TMY	0 %	0.0	- 0.0	0 %	0.0	- 0.0	0 %	0.0	- 0.0	0 %	0.0	- 0.0
M-EPL	0 %	0.0	- 0.0	0 %	0.0	+ 0.0	0 %	0.0	- 0.0	0 %	0.0	+ 0.0
M-CCT	14 %	1.5	+ 1.5	8 %	1.4	+ 1.2	9 %	2.4	+ 2.1	11 %	2.0	+ 2.0

Table 2.5 shows the MAPD, MAD and bias for each of the temperature intervals and future climate datasets. As expected, F-TMY has the best performance in predicting the different potentials, followed closely by M-TMY. M-EPL performs poorly than the previous two methods, especially in the too cold interval, while M-CCT has the worst performance in all the indicators. The highest MAPD are found on the cold potential. However, the high MAPD verified can be justified by the reduced availability of this temperature interval (on average 6.3 % in the F-10Y data), meaning that small differences in the number of hours lead to high percentage differences (MAPD). Regarding bias, M-TMY overpredicts ventilative cooling (+1.3 %, equal to MAD) and underpredicts warm potential (-1.5 %, equal to MAD). In line with the seasonal temperature analysis, the M-CCT shows a negative bias in the cold, natural ventilation and ventilative cooling intervals, and a positive bias in the warm interval. While the M-EPL only shows a clear bias to overpredict the cold (+1.4 %) and underpredict the warm (-1.9 %) temperature intervals.

Table 2.5 MAPD, MAD and bias of the different temperature intervals between F-10Y and the four climate data files.

	Too Cold (T ≤ 10 ºC) (6.3 %)			Natural Ventilation (10 < T ≤ 16 ºC) (22.4 %)			Ventilative Cooling (16 < T ≤ 26 ºC) (44.9 %)			Too Warm (T > 26 ºC) (26.4 %)		
	MAPD	MAD (%)	Bias (%)	MAPD	MAD (%)	Bias (%)	MAPD	MAD (%)	Bias (%)	MAPD	MAD	Bias (%)
F-TMY	13 %	0.8	- 0.4	6 %	1.3	+ 0.3	3 %	1.5	- 0.2	3 %	0.9	+ 0.3
M-TMY	15 %	1.0	- 0.6	6 %	1.4	+ 0.8	3 %	1.3	+ 1.3	6 %	1.5	- 1.5
M-EPL	27 %	1.7	+ 1.4	7 %	1.6	+ 0.5	4 %	1.8	+ 0.1	9 %	2.3	- 1.9
M-CCT	30 %	1.9	- 1.5	16 %	3.6	- 2.8	9 %	3.9	- 2.1	28 %	7.4	+ 6.4

Regarding extreme temperatures, Table 2.6 shows the MAPD, MAD and bias in number of heatwaves per year, its duration and the total number of days in heatwave, between the multi-year data and the four future climate results. It is observable that MAPD values are high (superior to 23 %) for the number and duration of heatwaves with all four climate data files. There is no significant bias in the number of heatwaves and heatwave duration, except for the heatwave duration with M-EPL (+ 4.2 days) and M-CCT (bias of +11.4 days). However, since heatwave duration and number of heatwaves are related, it is important to check the total number of days in heatwave. Considering this variable, MAPD diminish considerably in the F-TMY (7 %), M-TMY (9 %), M-EPL (13 %). M-CCT is the exception (MAPD is equal to 52 %), confirming the previous two climate analysis. These results indicate that number and length of heatwaves can be different between the different climate data files and F-10Y, but the total number of days is similar. However, these results should be interpreted with caution, since 1 heatwave with 20 days can have a significant higher impact than 4 heatwaves with 5 days each, stretching along the cooling season.

Table 2.6 MAPD, MAD and bias in heatwaves number, length and total number of days in a heatwave between multi-year data and the other climate data files. Average of the multi-year data is in brackets.

		MAPD	MAD	Bias
Number of heatwaves per year (4.7 per year)	F-TMY	25 %	1.2	+ 0.2
	M-TMY	28 %	1.3	- 0.4
	M-EPL	23 %	1.1	- 0.2
	M-CCT	31 %	1.5	- 0.2
Heatwave duration (days) (20.9 days)	F-TMY	35 %	7.3	+ 0.8
	M-TMY	27 %	5.6	+ 0.5
	M-EPL	36 %	7.6	+ 4.2
	M-CCT	66 %	13.9	+ 11.4
Total heatwave days (days) (85.8 days)	F-TMY	7 %	5.7	+ 2.3
	M-TMY	9 %	7.3	- 4.0
	M-EPL	13 %	11.1	+ 11.0
	M-CCT	52 %	45.0	+ 43.5

2.4.2 Impact on building energy consumption

The annual boiler energy consumption for the townhouse buildings and the annual HVAC energy consumption for the two office buildings, along with the MAPD, MAD and bias between the four different climate data files and the multi-year data are shown in Figure 2.6 and Table 2.7. Relevant differences are observable between the four climate data files, with F-TMY and M-TMY unsurprisingly having the lowest differences to the multi-year average, and M-EPL and M-CCT showing substantial differences.

The results show a clear overprediction of the annual boiler energy consumption of the townhouse buildings by the M-EPL especially in the cities with the lowest minimum temperatures (Bilbao, Madrid, Oviedo and Zaragoza). M-CCT shows no specific trend to overpredict or underpredict the results, although presenting high MAPD and MAD values. On the other hand, F-TMY and M-TMY show an underprediction trend, especially M-TMY, confirmed by the bias analysis. Regarding the HVAC energy consumption of the office

buildings the differences between the multi-year data and the climate data files are considerable smaller compared with the townhouse buildings, which may be justified by the order of magnitude of the results (kWh for the townhouses and MWh for the offices). M-EPL shows an underestimation of the energy consumption, F-TMY and M-TMY show no specific trend with reduced differences, while M-CCT clearly overestimates the energy consumption, confirmed by the bias analysis. However, in the M-CCT results, there are two cities that show an opposite signal: Coruna and Porto. Both cities are located at the North-West coast of Iberia and are the only cities that have a negative bias in the seasonal temperature analysis, in particular in the warmer seasons. This difference can be justified by the grid cell where both cities are located in the HadCM3 climate simulations, which reveals an underestimation of the temperature change. If these cities are not considered, bias is practically equal to MAD, confirming a systematic difference previously observable in the climate temperature analysis.

As seen before in the climate analysis, it is observable that M-EPL is able to represent the average seasonal temperatures. Although it does not reproduce accurately the daily variation of the climate, either due to different changes in minimum and maximum temperature either due to changes in other key variables such as solar radiation. This can be justified by the fact that the historical TMY used to produce M-EPL (EPL-TMY) has a different source of the multi-year data. It is also interesting to notice that the M-CCT has a significant positive bias on the mean seasonal temperature analysis, and the results of the annual heating energy consumption of the townhouses do not reflect this persistent bias, with some cities underpredicting and others overpredicting the energy consumption. The reason for a higher energy consumption may be the differences in solar radiation. An analysis of the total horizontal and direct normal radiations of M-CCT shows that these weather data files constantly present lower total daily values compared with the multi-year data. Furthermore, a seasonal analysis (similar to the temperature analysis presented in section 2.4.1), shows that the largest differences occur in Barcelona, Bilbao, Coruna, Oviedo and Zaragoza, which are exactly the cities that display higher energy consumption compared with the F-10Y in both townhouse buildings.

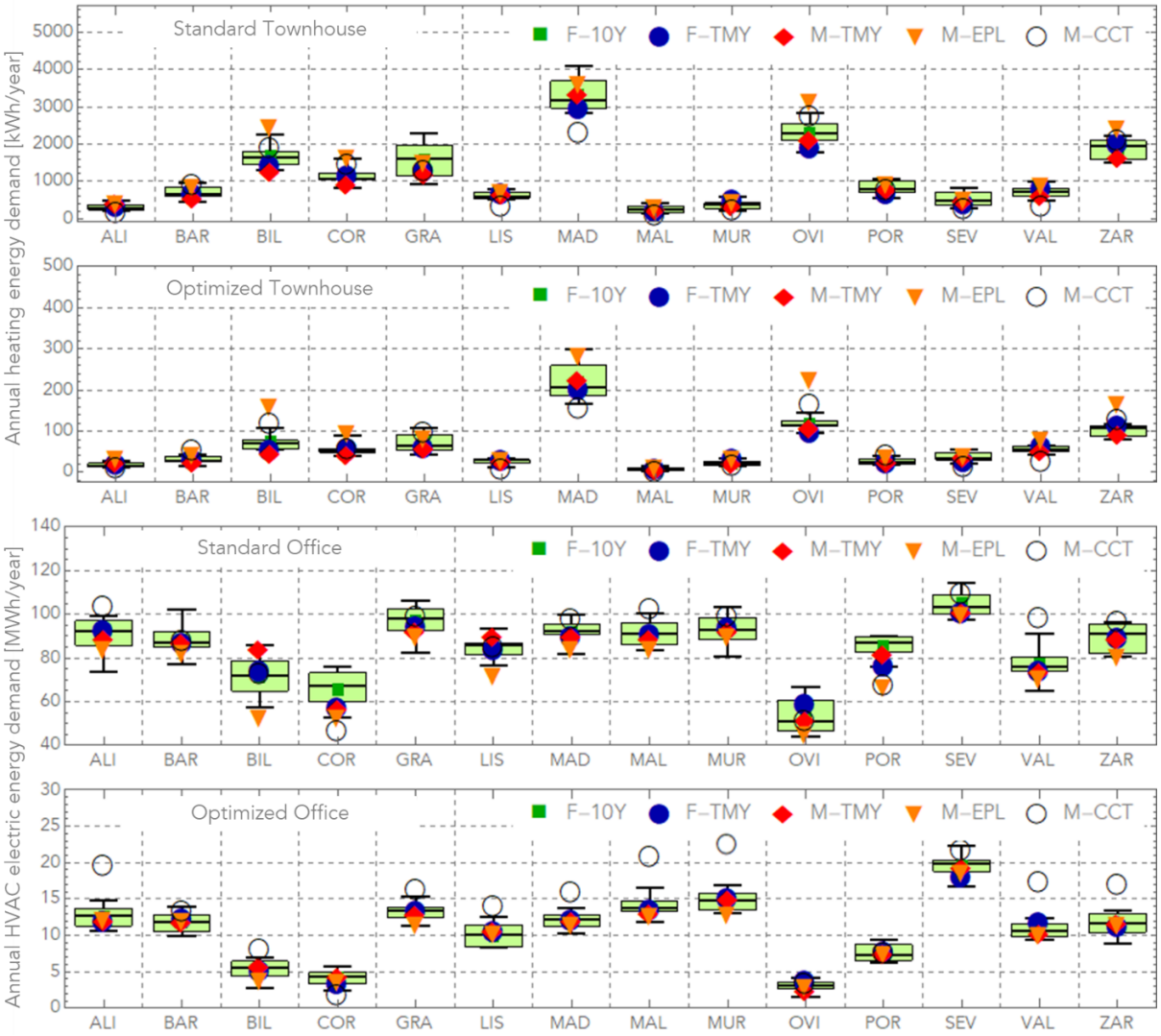

Figure 2.6 Annual heating energy consumption (Townhouse buildings) and annual HVAC electric energy consumption (Office buildings). Boxplots of the F-10Y with green dark dots representing the mean of F-10Y, in blue F-TMY, in red M-TMY, in orange M-EPL and in white M-CCT.

Table 2.7 MAPD, MAD and bias of annual heating energy consumption (Townhouse buildings) and annual HVAC electric energy consumption (Office buildings) between the multi-year data and the four climate data files.

		Annual energy consumption		
		MAPD	MAD	Bias
Standard townhouse (kWh)	F-TMY	13 %	149	- 82
	M-TMY	12 %	140	- 122
	M-EPL	23 %	269	+ 254
	M-CCT	27 %	307	- 83
Optimized Townhouse (kWh)	F-TMY	13 %	8	- 3
	M-TMY	13 %	8	- 6
	M-EPL	51 %	32	+ 32
	M-CCT	39 %	24	+ 2
Standard office (MWh)	F-TMY	4 %	3.1	- 1.5
	M-TMY	5 %	3.9	- 1.4
	M-EPL	11 %	9.4	- 9.4
	M-CCT	10 %	8.1	+ 2.5
Optimized Office (MWh)	F-TMY	5 %	0.5	- 0.0
	M-TMY	3 %	0.4	- 0.2
	M-EPL	7 %	0.8	- 0.7
	M-CCT	36 %	3.8	+ 3.5

The results of peak energy consumption for the difference cities are shown in Figure 2.7. In Table 2.8 the MAPD, MAD and bias are presented for the peak energy consumption of the four buildings, as well as the 99.6 percentile of the office buildings' electric cooling load. As anticipated, F-TMY and M-TMY show the best results, followed by M-EPL. M-CCT shows the biggest differences to the F-10Y average. A systematic underprediction occurs in the townhouse buildings across all climate data files, which is a sign of underprediction of the coldest period of the year. Regarding the office buildings, the peak energy consumption occurs during the cooling season, therefore the results are similar to the 99.6 percentile of the building cooling load. Significant bias is only found with M-EPL, which underpredicts the peak energy consumption and 99.6 percentile of the building electric cooling load. Since these variables are related with maximum outdoor temperature, the systematic bias can be justified by the fact that M-EPL are the only data files showing a negative bias on the maximum temperature analysis (-2.2 ºC) compared with F-10Y data.

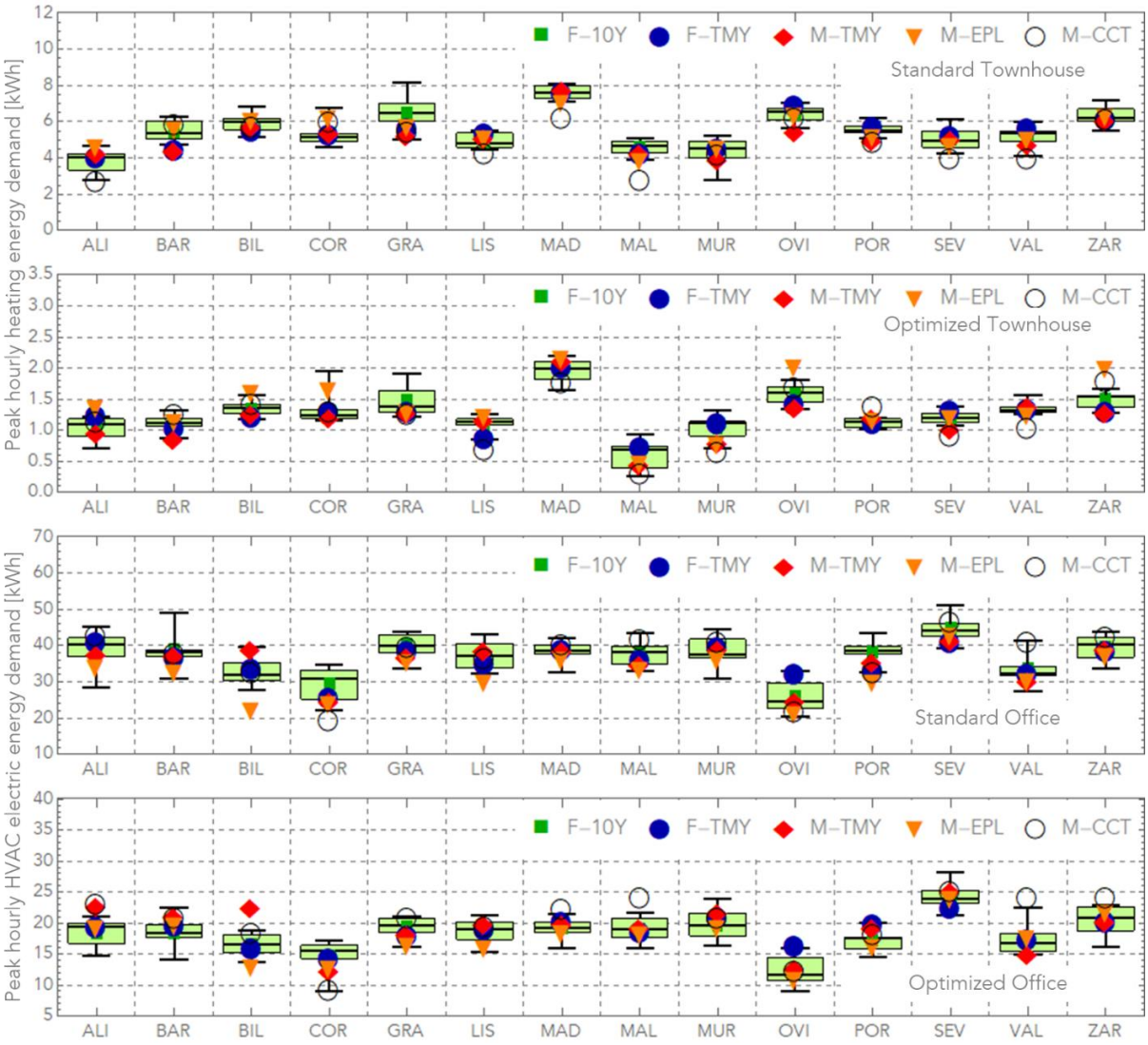

Figure 2.7 Peak hourly heating energy consumption (Townhouse buildings) and peak hourly HVAC electric energy consumption (Office buildings). Boxplots of F-10Y with green dark dots representing the mean of F-10Y, in blue F-TMY, in red M-TMY, in orange M-EPL and in white M-CCT.

Table 2.8 MAPD, MAD and bias of peak heating energy consumption (Townhouse buildings), peak HVAC electric energy consumption (Office buildings) and the 99.6 percentile of the office buildings' electric cooling load between the multi-year data and the four climate data files.

		Peak energy consumption			99.6 percentile of the electric building cooling load		
		MAPD (%)	MAD (kWh)	Bias (kWh)	MAPD (%)	MAD (kWh)	Bias (kWh)
Standard townhouse	F-TMY	6 %	0.3	- 0.1			
	M-TMY	9 %	0.5	- 0.4			
	M-EPL	7 %	0.4	- 0.1			
	M-CCT	14 %	0.8	- 0.7			
Optimized Townhouse	F-TMY	9 %	0.1	- 0.0			
	M-TMY	12 %	0.2	- 0.1			
	M-EPL	16 %	0.2	+ 0.1			
	M-CCT	18 %	0.2	- 0.1			
Standard office	F-TMY	7 %	2.4	- 1.0	4 %	2.8	- 2.5
	M-TMY	7 %	2.6	- 1.5	6 %	3.9	- 2.9
	M-EPL	14 %	5.2	- 5.2	12 %	7.3	- 7.3
	M-CCT	9 %	3.3	- 0.0	10 %	6.4	+ 1.2
Optimized Office	F-TMY	6 %	1.2	+ 0.4	5 %	2.0	- 0.4
	M-TMY	10 %	1.8	+ 0.9	7 %	2.5	- 0.3
	M-EPL	8 %	1.5	- 1.0	8 %	3.0	- 1.8
	M-CCT	15 %	2.7	+ 1.8	18 %	6.9	+ 4.9

Finally, since the townhouse buildings do not have cooling systems, the percentage of overheating hours were investigated during the occupied hours. In Figure 2.8 and in Table 2.9 are shown the summer overheating hours in percentage, and MAPD, MAD and bias, between F-10Y and the four climate data files. Again, as expected, F-TMY and M-TMY show the best results and have the smallest differences to the multi-year data. Both climate data files show a tendency to underpredict the results, especially in the standard townhouse. M-EPL and M-CCT climate files present significant differences to the multi-year data. Aligned with the temperature

potential analysis and the annual energy consumption, M-CCT shows a positive bias of the overheating hours, while M-EPL shows a systematic underprediction across all cities.

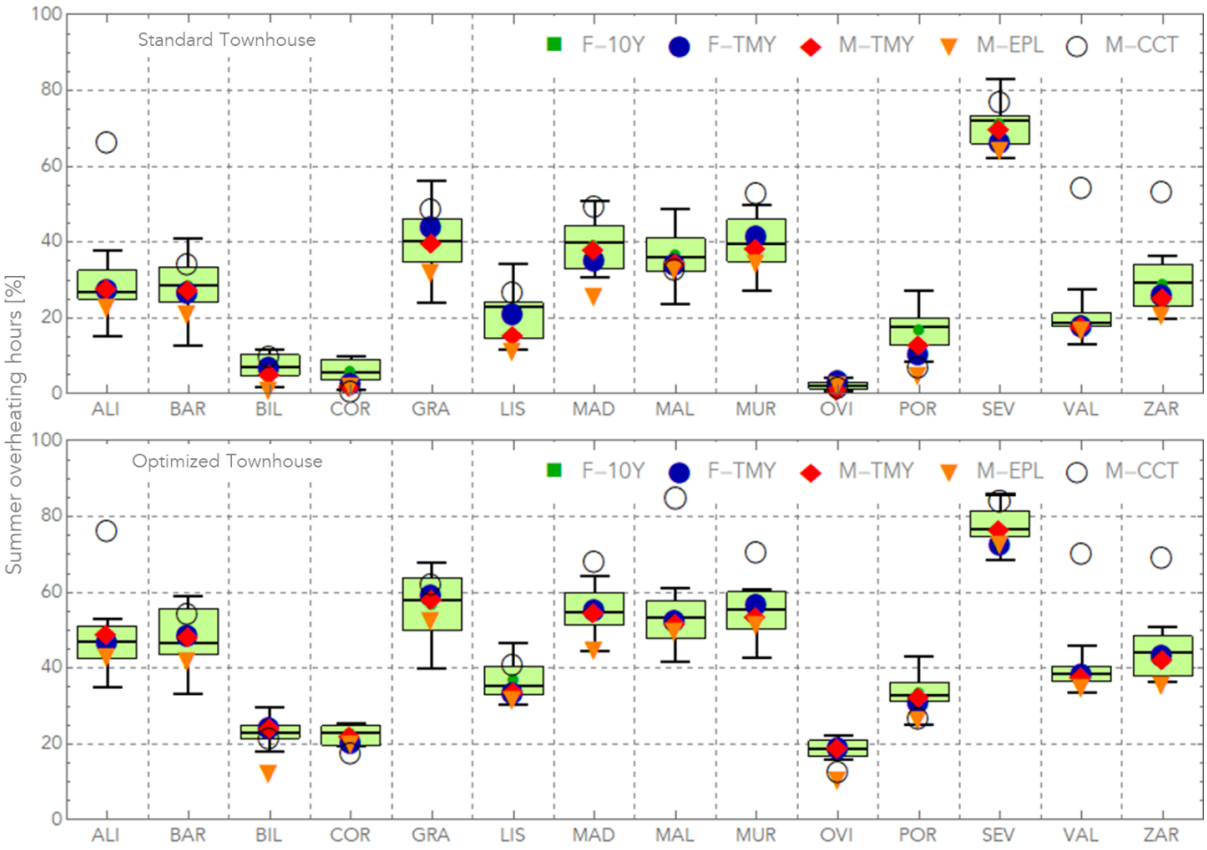

Figure 2.8 Summer overheating hours (%) of the standard townhouse building (top) and optimized townhouse building (down) calculated for all the cities and methods: boxplots of the multi-year data with green dark dots representing the mean of the multi-year data, in blue F-TMY, in red M-TMY, in orange M-EPL and in white M-CCT.

Table 2.9 MAPD, MAD and bias of the percentage of overheating hours during the occupied hours between the multi-year data and the other four climate data files.

		MAPD (%)	MAD (%)	Bias (%)
Standard townhouse	F-TMY	9 %	2	- 2
	M-TMY	8 %	2	- 2
	M-EPL	24 %	7	- 7
	M-CCT	44 %	12	+ 9
Townhouse Optimized	F-TMY	4 %	2	- 0
	M-TMY	2 %	1	- 0
	M-EPL	13 %	6	- 6
	M-CCT	31 %	14	+ 11

2.4.3 Impact of inter-annual variability

Table 2.10 shows the coefficient of variation (equation 2.10) of the BES outputs (annual and peak boiler energy consumption and overheating hours for the townhouse buildings and the annual and peak HVAC energy consumption for the two office buildings) analysed in this chapter. The results reveal two different features, one for each building type. The townhouse buildings show an increase in relative variability of the annual energy consumption, peak energy consumption and overheating hours between historical and future data. The office buildings show an opposite trend, with a decrease of the relative variability of annual and peak energy consumption. In the townhouse buildings, there is a decrease of the annual energy and peak energy consumption, corresponding to an increase of the coefficient of variation. While on the office buildings, the annual and peak energy consumption increase from the historical to the future datasets and the coefficient of variation diminish.

Current BES state-of-the-art uses a single weather year. According to the results of this chapter, for the four different buildings studied, the impact of weather variability on the results of BES will not increase in the future. The relative variability is important to understand if, in the future, simulation using a single year would be as representative of the climate as it was in the historical dataset. These results indicate that a F-TMY may also be adequate when simulating with future climates, despite the predicted increase in future weather variability. However, these results

should be analysed with caution, since only 10 years were used and in climatological studies 30 years are needed to draw more conclusive statements.

Table 2.10 Interannual variability of the three BES outputs of the multi-year data of the historical and future data-sets for the four different buildings.

		Coefficient of variation		
		Annual	Peak	Overheating
Standard townhouse	Historical	17 %	8 %	17 %
	RCP8.5	25 %	10 %	18 %
Optimized townhouse	Historical	20 %	13 %	9 %
	RCP8.5	28 %	13 %	12 %
Standard office	Historical	10 %	11 %	-
	RCP8.5	9 %	10 %	-
Optimized office	Historical	22 %	15 %	-
	RCP8.5	14 %	11 %	-

2.5 Conclusions

This chapter assessed the impact of various future climate data files on BES. Different data sources as well as different methods for building one-year climate data files were considered. The assessment used as reference high-resolution RCM climate simulations of Iberia (historical and future hourly data for 1990-1999 and 2090-2099). This multi-year data was used as a reference to compare the impact of two simplified methodologies commonly used to produce one-year representative weather data files for BES: typical meteorological year of future climate (F-TMY) and morphing of current TMY. Three different morphing data files were created: one using the past and future high-resolution reference data (M-TMY); a second using a publicly available TMY and morphed using the high-resolution reference data (M-EPL); and a third using the commonly used CCWorldWeatherGen tool to morph a publicly available TMY (M-CCT) file. Since M-TMY and F-TMY are produced using the reference dataset (while the other data files are not), there is an inherent bias in the improved agreement found for these data files.

The results show that BES differences are similar in both past and future TMY files compared to the references. P-TMY has MAPD between 4 % and 11 % and F-TMY between 4 % and

13 %, both 7 % on average, depending on building type and BES result considered. Inter-annual variability is similar in past and future datasets. For BES applications, using multiple years of future hourly data outputted by RCM increase computational and time demand while failing to provide a significant advantage compared to a TMY analysis.

The M-TMY file has a similar performance as the F-TMY file, with a MAPD from 3 % to 13 % (average 8 %) versus 4 % to 13 % (average 7 %). The Morphing method seems to be a good simplified solution for BES of future climate since differences between F-TMY and M-TMY are small and future monthly averages are more widely available than hourly data. However, using morphing with commonly available climate data files and tools may lead to high BES errors. The incorrectly morphed TMY file (M-EPL) results in a MAPD up to 39 % (average 16 %), while combining an incorrect TMY with outdated climate data and lower grid resolution (M-CCT) results in a MAPD up to 51 % (average 20 %), making these data files unsuitable for BES.

Chapter 3 - The shape of days to come: effects of climate change on low energy buildings

3.1 Introduction

The performance of passive design strategies is expected to be less sensitive to technological developments and more sensitive to climate change. There are several studies of the impact of climate change on passive buildings and passive strategies [75]. One study that focused on changes in NC effectiveness in European cities showed that, by 2085, in southern and central Europe, it will not be possible to achieve thermal comfort in a passive building with NC, whereas in north and other central European cities NC will become increasingly effective [118]. In the UK, by 2050, an office building will still benefit from NV use, although additional passive and active strategies will be necessary to keep comfortable indoor conditions [71]. In Greece, a study in three office buildings found that, by 2080, NV will be insufficient and additional cooling systems will be necessary [124]. Another study in Greece predicted that cooling degree-hours will increase between 152 % and 4200 % by 2095, depending on the climate region [125]. In Stockholm by 2090, natural cooling will still be effective for residential buildings even in the warmest scenario [126]. For residential buildings in the Netherlands [127] and UK [128] solar shading and NV are the best passive strategies to reduce energy demand in future climate (considering as representative of future climate conditions the year of 2100 for the Netherlands and the warmer year of 2003 for the UK). Switzerland's heating season will be 53 days shorter by 2075, and solar protection and NC will become key elements in effective building design [129]. By 2050, in low-income housing in Seville, climate change will increase the importance of controlling solar gains through façades and roofs, as well as performance differences due to building orientation [130]. A recent study showed that in the end of the current century passive cooling will still be effective for residential buildings located in San Francisco and Seattle [70]. In residential bioclimatic buildings in Slovakia, by 2050, overheating prevention (particularly shading and NV) will become key elements in successful building designs [131].

Passive buildings often use a combination of NV, shading and, when needed, passive solar heating [22, 23]. One common solution is the use of fixed horizontal overhangs on the south façade (north hemisphere) [132] that allows solar radiation into the building in the winter

season, and, when the sun position is higher in the summer months, blocks the direct incidence of solar radiation on the windows. As global temperatures rise, higher temperatures will occur earlier in the year, farther from summer solstice, creating a longer season where shading is required. This longer shading season incorporates periods with lower maximum daily solar altitude, compromising the efficacy of overhang and increasing the incidence of solar radiation. Further, daily variations in maximum solar altitude are not constant, changing with solar declination. Solar altitude daily variation is maximum at equinox, and minimum at solstices. Simultaneously, higher temperatures will reduce the local climate potential for NV use and the periods when NV can be effective will shift farther from yearly peak temperature, occurring both earlier and later in the year. In some cases, this shift in NV potential overlaps with the increased solar radiation, affecting the overall performance of passive buildings. This temperature shift changes existing correlations between temperature and solar altitude and makes existing horizontal window shading overhangs undersized (Figure 3.1a).

In addition, passive building strategies, such as NV and NC, are also dependent of the diurnal temperature cycle. Consequently, analysing the average upcoming temperature increase is not enough to understand the effect of climate change on passive buildings, and changes at a sub-daily scale must be analysed to capture the extension of changes in the efficiency of passive design strategies. Sub-daily changes will reshape existing diurnal temperature cycles, as different warmings will occur in different times of the day. This reshape of the diurnal temperature cycle will modify the daily temperature range (DTR), a fundamental driver of NC (Figure 3.1b). Therefore, the analysis of the sub-daily variations are essential to have a broad understanding on how passive strategies will be affected and how they could be efficiently designed for future climates.

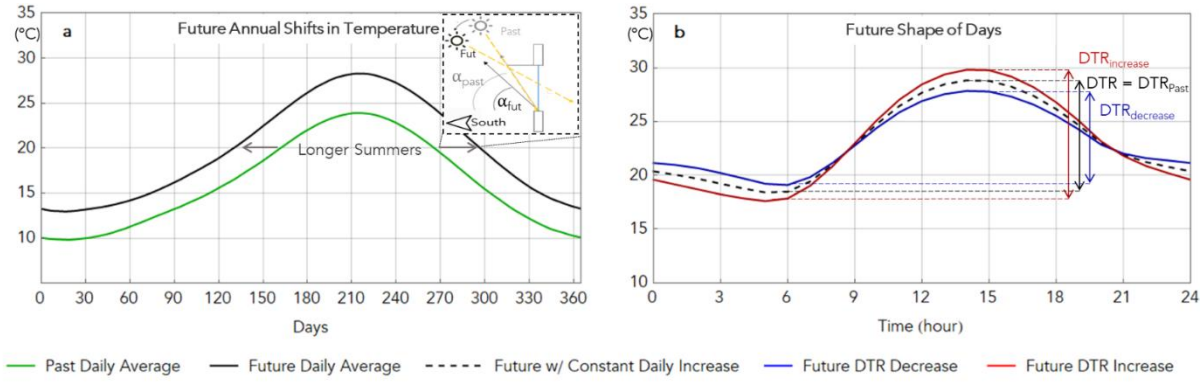

Figure 3.1 Representation of future annual shifts in daily average temperature and changes in future shape of days

Currently, there is no study that performs a detailed analysis of upcoming changes in temperature, their interaction with solar radiation, and the consequent impacts on passive building strategies. This chapter addresses this knowledge gap, by focusing on daily and annual temperature variations, and analysing when, where and how passive design strategies are affected. This chapter uses high spatial and temporal resolution modelled climate data from 11 different regional climate models (RCMs) for two 30-year periods of past (1971-2000) and future (2071-2100) data under a business-as-usual emission scenario (RCP8.5), to perform the analysis in the 43 most populated urban areas in the European Union (EU) [86]. This analysis approach allows for a detailed understanding of the temporal behaviour of passive design strategies in future climate, going beyond season or yearly effectiveness.

There are two major analysis in this chapter. The first analyses upcoming changes in the shape of the average diurnal temperature cycles, for each month, and their possible impact on thermal energy consumption and in night cooling and daytime NV potential in residential and commercial buildings. The second analysis focus on annual shifts in temperature distribution and how they impact the effectiveness of passive design strategies (NV, NC and solar shading) with emphasis on the correlation between solar gains and outdoor air temperature. Other passive building strategies (thermal insulation, air tightness and thermal mass) are not assessed in this chapter since these are much more dependent on the building construction than on the local weather conditions. The next section presents the methodology, in which the climate data and the different analysis are displayed. The following section presents the result and discussion of the changes in shape of days and annual shifts in temperature. The final section presents the conclusions.

3.2 Methodology

This chapter will compare past (1971-2000) and future (2070-2100) climates in the 43 most populated cities in the EU [86]. This choice ensures adequate representativeness of Europe, its different climate regions and urban population. The terms “compare” and “changes” are used in this chapter to refer to the variations of different climate variables and passive design strategy performance metrics between past and future climates in the 43 cities.

The methodology of this chapter is shown schematically in Figure 3.2. The climate data used in this chapter is presented in Section 3.2.1. The analysis is performed in two scales: daily and annual. The daily scale, named Shapes, compares time plots of temperature (y-axis) with time (x-axis) in equivalent past and future 24h periods. The shape analysis will focus on changes of the diurnal temperature cycle, particularly on DTR and its impacts on building energy demand (Section 3.2.2 and item 1. in Figure 3.2). The annual scale, named Shifts, will compare the variations of temperature throughout the year, such as the occurrence of early and late summers, and how this phenomenon affects solar radiation, wind and passive building strategies.

The shift analysis is divided in three sub-sections shown in the Figure 3.2 (items 2-4). NV potential (Section 3.2.3 and item 2. in Figure 3.2) is assessed by calculating the changes in annual cooling degree hours (CDH) and by comparing frequency distributions of air temperature in four intervals (from too cold to too warm for NV). Item 3 in Figure 3.2 (Section 3.2.4) compares days with similar maximum temperature. Finally, item 4 (Section 3.2.5) compares optimal overhang sizes and solar incidence in south facing windows.

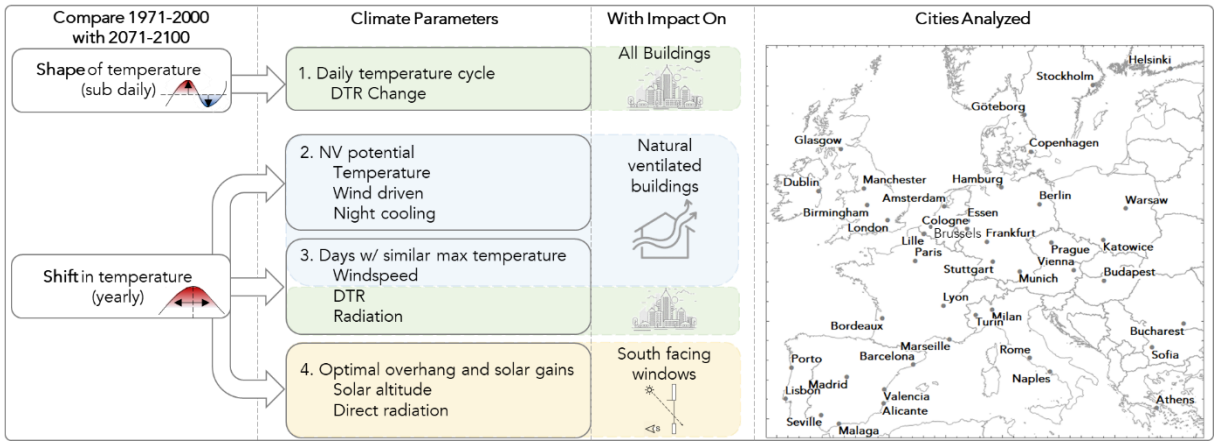

Figure 3.2 Schematic representation of the different analysis and spatial distribution of 43 most populated cities in the EU.

3.2.1 Climate data

The General Circulation Models (GCMs) that are used to produce future climate projections, have been proven accurate for prediction of the temperature changes that occurred during the last 50 years [133]. GCM models are currently used in an ongoing coordinated effort by several research groups, known as Coupled Model Intercomparison Project (CMIP5), to simulate past and future climates based on four emission and concentration scenarios for the 21st century [62]. These scenarios are known as Representative Concentration Pathways (RCPs) and are based on socio-economic, technological, energy, land use and cover, emissions of GHG and air pollutant (e.g. SO_2 or NO_x) projections [63]. Each RCP uses a different imbalance between incoming and outgoing radiation on a global annual average (known as radiative forcing) for the year 2100 relative to pre-industrial era. There are four standard average annual values of this radiative forcing: 8.5 W/m^2, 6 W/m^2, 4.5 W/m^2 and 2.6 W/m^2.

The CMIP5 simulations use GCM with a horizontal resolution of approximately 100 km. This resolution can represent large-scale atmospheric variability but is unable to simulate local climate processes, as changes in land-cover distribution, coastlines, or complex topographies [134]. To improve the representation of local climate changes, Regional Climate Models with finer grid resolutions are used with dynamic boundary conditions produced by the GCM [66]. In Europe, the EURO-CORDEX project provides freely available RCM simulation results of a wide range of climatological variables for the 20th and 21st centuries at 12 km (0.11°) and 3-hour resolution [69].

This chapter uses weather data from 11 different RCM simulations of the EURO-CORDEX climate database that follow the RCP8.5 forcing/emission scenario (business as usual, see Table 3.1). The data has 12 km x 12 km and 3-hour of spatial and temporal resolutions, respectively, and includes air temperature at 2 meters, wind velocity and total solar shortwave downwelling radiation. There are eleven model outputs with 30 years of past (1971-2000) and future (2071-2100) climate data.

There is a known bias in the RCA4 climate models that leads to underestimation of temperature in northern Europe and in the Mediterranean region in winter, and overestimation in south-eastern Europe in winter and in Mediterranean in Summer [135]. This problem has a limited effect in the present chapter since it compares simulated future and past data, thereby removing the impact of observation bias [136]. In addition, this analysis combines all model outputs, a multi-model ensemble approach that reduces the impact of errors in individual models [137].

Table 3.1 EURO-CORDEX regional climate models considered in the present chapter, along with the responsible institution, the forcing global climate model, and the number of days in each model

Institution	Reference	RCM	Forcing Model
Swedish Meteorological and Hydrological Institute	Samuelsson et al. [135]	RCA4	1. CNRM-CERFACS-CNRM-CM5; 2. ICHEC-EC-EARTH; 3. IPSL-IPSL-CM5A-MR; 4. MOHC-HadGEM2-ES; 5. MPI-M-MPI-ESM-LR; 6. NCC-NorESM1-M; 7. ICHEC-EC-EARTH2
Climate Limited-area Modelling Community	Rockel et al. [138]	CCLM4-8-17	8. CCCma-CanESM2; 9. MIROC-MIROC5
Centre National de Recherches Meteorologiques	Daniel et al. [139]	ALADIN63	10. CNRM-CERFACS-CNRM-CM5
Climate Service Center Germany (GERICS)	Jacob et al. [140]	REMO2015	11. NCC-NorESM1-M

3.2.1.1 Capability of RCM to represent urban heat island

To verify that the resolution of the climate models reproduces the effects of the urban landscape, known as urban heat island (UHI) effect, the temperature variations in a five-by-five grid is analysed for London and Paris. Since the focus of this chapter is not extensively analyse the UHI effect, only two cities are analysed. The annual mean, minimum and maximum temperatures differences between the city centre and the surrounding are calculated, in both past and future climates. This chapter defines the location of each city by the grid cell closest to the city centre coordinates [141]. The analysis of UHI effect focuses on the 25 grid points that are closer to the city centre of these two cities.

3.2.2 Changes in shape of days

This section presents the methodology to analyse changes in the diurnal temperature cycle and their effects on DTR and thermal energy demand of buildings. Changes in monthly diurnal temperature cycle, ΔT_h, are defined as a numerical array of 24 values of temperature change between past and future days that are evaluated in the four sequential steps shown in Figure 3.3:

1. Calculate the monthly diurnal temperature cycle for past climate ($T_{P,h}$, Figure 3.3a).
2. Add the monthly average temperature difference between past and future climates $(T_{F,m} - T_{P,m})$ to $(T_{P,h})$. This step generates the monthly diurnal temperature cycle of future climate that would occur if there is a constant increase in temperature throughout the day. If this is the case, there would be an equal DTR in future and past climates (also shown in Figure 3.3a).
3. Calculate the monthly diurnal temperature cycle of future climate ($T_{F,h}$), similar to step 1 but using future data instead of past data. These future diurnal temperature cycles are located in the gray area shown in Figure 3.3b. Future diurnal temperature cycles have the same average temperature increase as step 2 but a different shape, as shown by the difference between the dashed (2), blue (4N, representative of higher nighttime temperature increase) and red (4D, representative of higher daytime temperature increase) lines in the figure.
4. Subtract $(T_{F,m} - T_{P,m})$ to $(T_{F,h} - T_{P,h})$ in order to obtain the monthly diurnal temperature cycle difference (ΔT_h). In this step, the hour when ΔT_h maximum occurs is calculated. If the maximum ΔT_h occurs during the day, a daytime shape is obtained (shown in red in Figure 3.3c), and DTR increases in the future (shown in red in Figure 3.3b). If the maximum ΔT_h occurs during the night, a nighttime shape is obtained (shown in blue in Figure 3.3c), and DTR decreases in the future (shown in blue in Figure 3.3b).

The diurnal temperature cycle difference results in values above and below the future average temperature increase (represented by the dashed line in Figure 3.3). The daily integral value of the shapes is zero. The hour when ΔT_h maximum occurs indicates when the monthly temperature increase is highest. The amplitude of ΔT_h is calculated to understand the magnitude of changes in the shape of days.

$$\Delta T_h = \left(T_{F,h} - T_{P,h}\right) - \left(T_{F,m} - T_{P,m}\right) \qquad (3.1)$$

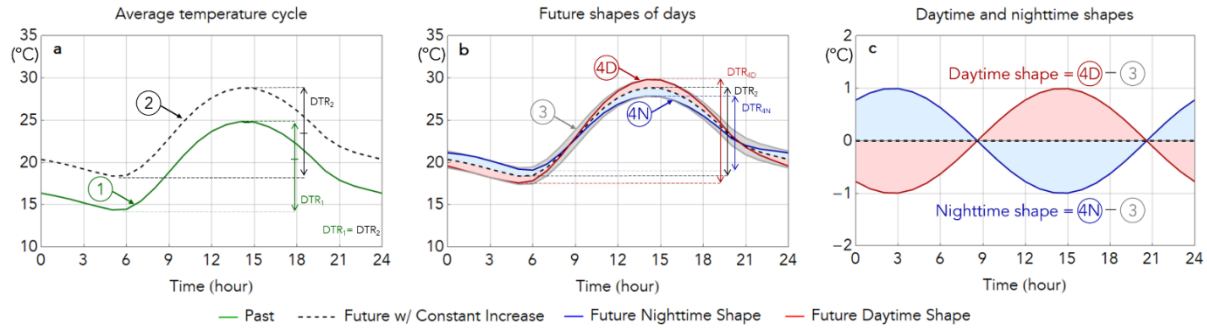

Figure 3.3 The four steps used to obtain the diurnal temperature cycle difference and the two shapes patterns.

3.2.3 Shifts in NV potential

In this section the two methodologies used to study the impact of upcoming temperature shifts are presented. The first (section 3.2.3.1) compares the distribution of air temperature in four different intervals, defined according to the suitability of temperatures for NV. The second (section 3.2.3.2) focuses on changes in total annual cooling degree hours (CDH) and the capabilities of wind driven NV and NC as NV strategies to reduce CDH.

3.2.3.1 Suitability of air temperature for NV

This analysis groups the outdoor temperature in four different intervals, associated with the availability of outdoor conditions for NV, and, on a weekly basis, comparing past and future climates. This chapter considers that the outdoor air temperature can be used to increase the indoor air quality (IAQ) and thermal conditions [142] between 10 °C and 26 °C. Below the lower limit, temperatures are too cold (TC) to provide fresh air [114], and above 26 °C temperatures are too warm (TW) to be used as natural ventilative cooling [115]. Between the temperature limits, two additional intervals are defined: natural ventilation (NV) from 10 °C to 16 °C, and ventilative cooling (VC) between 16 °C and 26 °C. User operated window opening area has been shown to start to increase at 15°C [116, 114], conservatively, a 16°C is used in this chapter. The NV range considers that IAQ can be achieved using fresh outside air through window openings. While the VC range is able to remove heat gains, and improve or maintain

thermal comfort [117], either by increasing window opening areas or by mechanical ventilation. The four outdoor temperature intervals used in this chapter are:

- TC - Too Cold for NV ($T \leq 10$ °C);
- NV - Suitable for NV/fresh air supply (10 °C $< T \leq 16$ °C);
- VC - Suitable for NV based ventilative cooling (16 °C $< T \leq 26$ °C);
- TW - Too Warm for NV ($T > 26$ °C).

This analysis considers a schedule between 9am and 6pm, typical of commercial buildings, which are buildings that expect more than 80 % increase in energy demand by 2050, specially driven by cooling energy demand [21].

3.2.3.2 CDH and CDH reduction by wind driven and night cooling natural ventilations

Cooling degree hours (CDH) are a widely used climate metric for sensible cooling energy demand [143]. CDH are defined as the sum of temperature differences above a fixed threshold (Equation 3.2). In this chapter, the threshold is set to 26 °C, the lower limit of the TW class discussed in section 3.2.3.1 and [143]:

$$\mathrm{CDH} = \sum_{n}(\mathrm{DBT} - 26) \times \mathrm{dt}\,, \text{if } \mathrm{DBT} \geq 26\ ^{\circ}\mathrm{C} \qquad (3.2)$$

Where n is the number of hours, DBT the dry bulb temperature, and dt is the time interval of the data (3 hour).

Both wind driven NV and NC by NV, due to the DTR, can reduce CDH [143]. When the effect of these strategies is considered during CDH calculation, two lower CDH indicators are obtained: residual CDH due to wind-driven NV ($CDH_{res\text{-}WD}$); and residual CDH due to NC NV ($CDH_{res\text{-}NC}$). The first, $CDH_{res\text{-}WD}$, assumes that airflow generated by wind reduces the skin temperature due to convective heat exchange with the air. For this simplified analysis the relationship between air velocity and the temperature decrease perceived by the occupants ($\Delta T_{v,air}$) is given by Equation 3.3:

$$\Delta T_{v,air} = 2.139\, v_{air} + 0.4816\ [^{\circ}\mathrm{C}] \qquad (3.3)$$

$$v_{air} = v_{wind} \times f_{rw}\ [\mathrm{m/s}] \qquad (3.4)$$

Where V_{air} is the indoor air velocity and is calculated using Equation 3.4, where V_{wind} is the wind speed, and f_{rw} the reduction factor applied to replicate the discharge coefficient of a

conventional window opening (0.6) [144]. This approach considers air speeds between 0.25 and 1.5 m/s. Lower speeds have no effect on the temperature perceived by the occupants and, thus, are ignored. On the other hand, higher speeds can lead to draft induced discomfort, so their effect are considered equivalent to 1.5 m/s. The $CDH_{res\text{-}WD}$ are then calculated using Equation 3.5:

$$CDH_{res-WD} = \sum_n((DBT - \Delta T_{v,air}) - 26) \times dt, \text{if } DBT \geq 26\,°C \quad (3.5)$$

The $CDH_{res\text{-}NC}$ considers that a building can be cooled during nighttime through buoyancy-driven ventilation, when outdoor temperatures are lower. The building thermal mass is cooled during the night and absorbs heat during the day, allowing the building to be within the thermal comfort range for longer periods. The $CDH_{res\text{-}NC}$ are calculated using the following expression:

$$CDH_{res-NC} = \sum_{day}(\sum_{nday,cd}(DBT - 26) + (\sum_{nday,nc}(DBT - 26)) \times EF) \times dt, \text{if } DBT \geq 26\,°C \quad (3.6)$$

Where day is the number of days, nday,cd the number of hours with cooling demand, nday,nc the number of hours with night cooling potential, and EF the exploitation factor (0.7) [143].

3.2.4 Days with similar maximum temperature

In order to compare the past and future climates, daily records are grouped according to the daily maximum air temperature (in 1 °C intervals). This variable has been shown to be correlated with the increase in peak urban electricity demand driven by a higher usage of air-conditioning systems [145]. Additionally, only days with maximum temperatures above 15 ºC are considered, since this is the typical temperature beyond which building cooling demand is triggered [145]. The number of days in each 1 ºC-interval and when such days occur in the year (earlier and later) are assessed, as well as changes in DTR, wind speed, maximum solar altitude, total daily radiation and direct solar radiation on a south facing façade at solar noon.

As a pre-processing step, the variables under study are first subjected to a moving average. The average for each day consists of that same day and the previous and following 15 days (i.e. a 31-day centred moving average). All the climate variables are outputted by the EURO-CORDEX models, except for direct solar radiation at solar noon, which is calculated using the 3-hour averages of downwelling shortwave radiation outputted by the models. The two data values closest to solar noon are taken (corresponding to the average of the periods 9h-12h and 12h-15h) and the clearness index (k_t) is calculated for both. The two values are averaged to

obtain an average k_t at noon. Total solar radiation (I_{global}) at solar noon is computed considering the average k_t and the horizontal extra-terrestrial radiation. Then, the diffuse horizontal solar radiation ($I_{diffuse}$) is calculated (Equation 3.7) [146]:

$$\frac{I_{diffuse}}{I_{global}} = \begin{cases} 1.020 - 0.254k_t + 0.0123\ \sin(\alpha),\ 0 \le k_t \le 0.3;\ \frac{I_{diffuse}}{I_{global}} \le 1.0 \\ 1.400 - 1.749k_t + 0.177\ \sin(\alpha),\ 0.3 \le k_t \le 0.78;\ \frac{I_{diffuse}}{I_{global}} \le 0.1 \\ 0.486k_t + 0.182\ \sin(\alpha),\ 0.78 \le k_t;\ \frac{I_{diffuse}}{I_{global}} \le 0.1 \end{cases} \quad (3.7)$$

The direct horizontal solar radiation (I_{direct}) is the difference between I_{global} and $I_{diffuse}$. Finally, the direct solar radiation incident on the south facing façade ($I_{direct,façace}$) is calculated using Equation 3.8:

$$I_{direct,façade} = \frac{I_{direct}\sin(\alpha+90)}{\sin(\alpha)} \quad (3.8)$$

In the next step, days are allocated to intervals of 1 °C according to daily maximum air temperature (such as $20 \le T < 21$ °C) and the first and last appearance of each temperature interval in the year is calculated. Finally, for each maximum temperature interval, the average DTR, average wind speed, average maximum solar altitude, average total daily radiation and average direct solar radiation incident on a south facing façade at solar noon are calculated.

3.2.5 Optimal overhangs and solar gains

This section presents the methodology to design a fixed horizontal overhang and to calculate changes in direct solar radiation incident on a south facing façade and window.

To understand how optimal overhang dimensions change in future climate and the consequent impact in building solar gains, a south facing horizontal overhang is sized for past and future climates using a degree-day selection method [147]. This method identifies periods of possible overheating, through Cooling Degree Days (CDD), and periods where solar gains are desired, through Heating Degree Days (HDD). The perfect overhang design should shade the whole period when CDD are higher than HDD. However, this shading period is usually asymmetric around summer solstice, with fewer days requiring shading before summer solstice than after, while a fixed simple horizontal overhang provides symmetric shading before and after solstice. Since designing an overhang that covers the whole shading period is unfeasible, a compromise is found between the first and last day (in absolute value around solstice) when shading is required:

1. Calculate HDD (Equation 3.9) and CDD (Equation 3.10) for a base temperature (T_{base}) of 18.3 °C [148], obtaining a total of 365 values after averaging daily all models and years.
2. Calculate the daily difference between CDD and HDD.
3. Find day of symmetry around summer solstice when the difference between CDD and HDD is higher than the difference between HDD and CDD. That day is defined as the optimal overhang day when shading is required at solar noon.

$$\mathrm{HDD} = \sum_{i=1}^{day}(T_{base} - \overline{T}_i) \text{ [only positive values]} \quad (3.9)$$

$$\mathrm{CDD} = \sum_{i=1}^{day}(\overline{T}_i - T_{base}) \text{ [only positive values]} \quad (3.10)$$

Considering $\overline{T}_i$the mean daily temperature calculated as the average between daily maximum and minimum temperatures. Then, the ratio between the window height and the overhang length (named overhang length ratio - OLR), and the relative window area that is shaded by the overhang (named overhang obstruction ratio on the window plane, OOR_{Future}) are calculated through the following steps:

1. Calculate the daily solar altitude at solar noon (α).
2. Calculate the OLR (Equation 3.11) for the optimal overhang day, for past and future climates.
3. Calculate daily OOR_{Future} (Equation 3.12) for future climate considering an overhang designed for the past climate (OLR_{Hist}). OOR_{Future} is limited to a maximum value of 1, i.e. full obstruction of the window plane.

$$\mathrm{OLR} = \frac{1}{\tan\alpha} \quad (3.11)$$

$$\mathrm{OOR_{Future}} = \tan\alpha \times \mathrm{OLR_{Hist}}; \mathrm{OOR_{Future}} \leq 1 \quad (3.12)$$

Finally, the direct solar gains incident on a south facing façade at solar noon (Idirect,façace) are calculated using Equation 3.7 and Equation 3.8 for four scenarios:

1. Optimal overhang day Past, climate Past (PP).
2. Optimal overhang day Future, climate Future (FF).
3. Optimal overhang day Past, climate Future (PF).
4. Optimal overhang day Future, climate Past (FP).

3.3 Results and discussion

3.3.1 Capability of RCM to represent urban heat island

This sub-section presents the results of the UHI analyses for London and Paris. Figure 3.4 shows that, as expected, the models capture that the city centres are consistently the warmest place in Paris and the second warmest in London, confirming the existence of an UHI. The UHI magnitude is approximately 1°C, similar to the magnitude measured in previous studies in Paris [149] and London [150,151]. These results confirm that urban landscapes (cities) are represented on the land-cover assumptions of the RCM used and have an effect on near-surface temperatures [141].

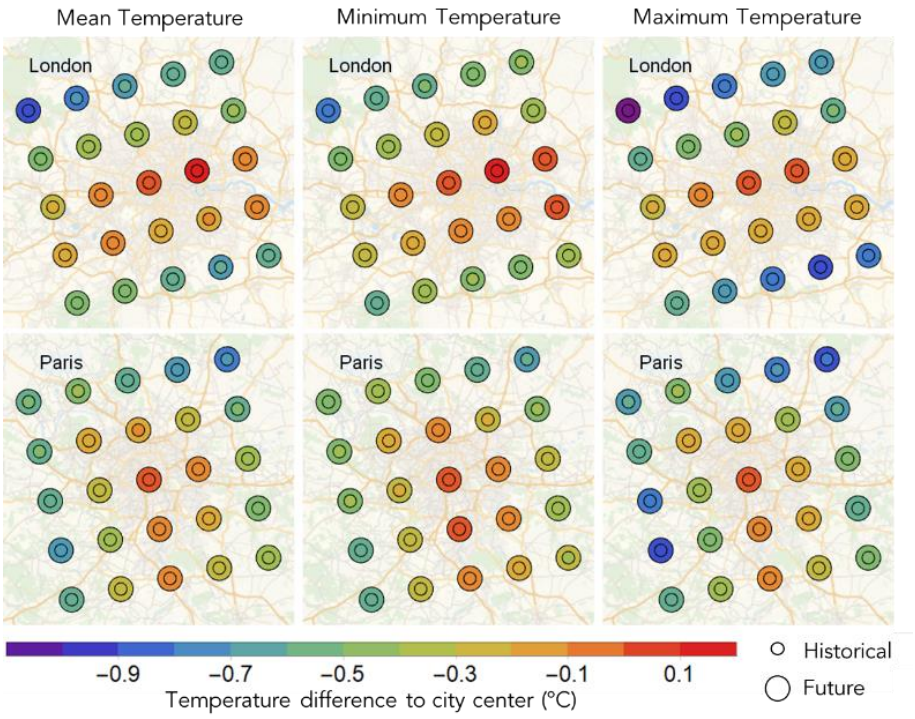

Figure 3.4 Mean, maximum, and minimum temperatures differences between the city centre and the surrounding grid points for past and future climate at Paris and London.

3.3.2 Changes in shape of days

This sub-section analyses the changes in the diurnal temperature cycle and their effects on DTR and thermal energy demand of buildings. In order to have a better understanding of the magnitude of the changes analysed in this section, the predicted future average season temperatures and the average season temperature increase are plotted in Figure 3.5. The

expected temperature increase is higher during the summer in low latitude regions (below 48°N, including Budapest), and during the winter in Scandinavia and eastern Europe.

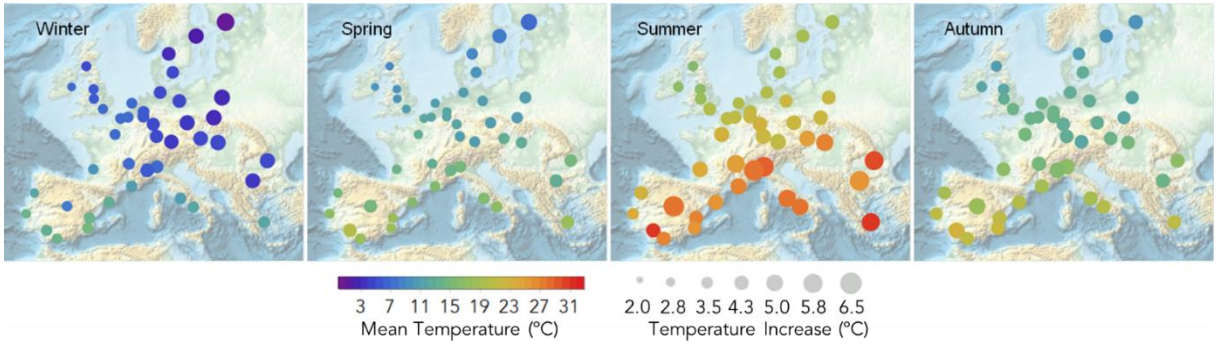

Figure 3.5 Average season temperature of future climate (colour scheme) and average season temperature increase between future and past climates (circle size).

Figure 3.6 shows the DTR change in function of the hour of maximum temperature increase (maximum of the difference between future and past diurnal temperature cycles) calculated for all cities and months. The results reveal that, on average, there is a relation between the hour of maximum temperature increase and changes in DTR:

- Daytime maximum increase leads to higher DTR (here referred to as daytime shape).
- Nighttime maximum increase leads to lower DTR (here referred to as nighttime shape).

In light of this relation, it is likely that simplified analysis based on average monthly temperature increase in the future, ignoring variations of the shape of diurnal temperature cycle and, consequently, DTR, will not be able to estimate the effects of climate change in energy savings from NV and NC strategies. The size of the error that results from this oversimplification is expected to depend on location, season, and building type. The remainder of this section will look for the presence of these two shapes in the data and investigate their impact in low energy building systems.

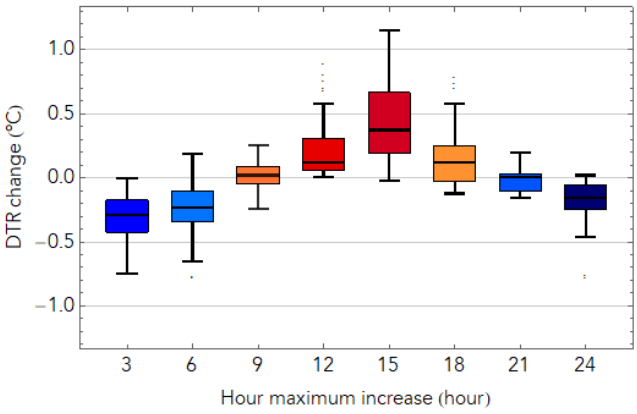

Figure 3.6 Boxplots of DTR change function of the hour of maximum monthly temperature increase calculated for all cities and months.

Figure 3.7 shows the hour of maximum temperature increase (hour when ΔT_h maximum occurs) and the amplitude of the shape for each month. The highest amplitudes, in absolute and relative values, occur between May and September for most cities. However, in northern Italy (Turin and Milan) and in south-eastern Europe (Sofia and Bucharest), the highest amplitudes occur during winter, when the amplitudes relative to the maximum average temperature increase are higher than 20 %. As observed in Figure 3.6, the hour when maximum temperature increase occurs impacts the DTR. When it occurs during the day there is a DTR increase (e.g. Bordeaux). Conversely, when it occurs during the night there is a DTR decrease (e.g. Helsinki from April to October). These two shapes have different impacts depending on the season, region and building type, and a summary of the possible impacts is shown in Table 3.2.

In locations that will have daytime shapes, relevant increases in DTR are expected to occur in both winter and summer, impacting either heating or cooling thermal energy demand. During winter in cities in northern Italy, south-eastern Europe and Madrid, daytime temperatures will increase significantly due to a combination of average temperature increase (Figure 3.5) and DTR increase (daytime shape). In commercial buildings, the increase can result in lower space heating demand than expected if the shape is ignored, since higher temperatures occur during the occupied period. On the other hand, in residential buildings the heating energy demand can be higher than expected because most of the demand occurs at the beginning and end of the day [152], when temperatures are lower than the average monthly temperature increase. During the summer, in France, Germany and Belgium, the increase in DTR can reduce the daytime NV usage and increase NC ventilation usage (thru the exploitation of thermal mass), compared with a climate with a constant temperature increase. In western Iberia, the DTR increase in addition to high monthly average temperatures, can result in higher cooling energy demands than expected and, where possible, increase the use of NC by efficient use of exposed thermal mass.

Nighttime shapes decrease the DTR, by combining lower daytime temperatures and higher nighttime temperatures. Nighttime occur mostly during the cooling season (from May to September) in northern Europe and in the Mediterranean coast. In May and June in northern Europe, the DTR decrease can increase the daytime NV usage and reduce NC usage. However, NC usage may not be much affected, because the low average outdoor temperatures verified in this region do not require high cooling energy demands. During summer in the Mediterranean coast, high temperatures make the use of NV and NC unfeasible, hence the decrease in DTR do not impact natural ventilated buildings. However, maximum daily temperatures will be lower than expected, resulting in lower cooling and peak energy demands than if only mean temperature is considered.

On the other hand, if the temperature increase occurs at a different time of maximum or minimum temperature it may also impact the building capacity to use the external environment conditions. If the increase occurs during the morning, the temperature increase rate is faster and consequently unsuitable conditions can be reached earlier in the day, reducing the periods of ventilation. The opposite occurs if the increase occurs during the afternoon.

Table 3.2 Impact of the daytime and nighttime shapes on different seasons, buildings, and regions.

Season	Climate Type	Shape of Days	Building Type	Heating	Cooling	NV	NC (thermal mass)	Occurs in
Heating season	Cold winters	Daytime	Commercial	-				Northern Italy, South-eastern Europe, Madrid
			Residential	+				
Cooling season	Mild summers	Daytime	With NV			-	+	France, Belgium, Germany
		Nighttime	With NV			+	-	Northern Europe (May, June)
	Hot summers	Daytime	All		+		+	Western Iberia
			With NV					
		Nighttime	All		-		-	Mediterranean Coast
			With NV					

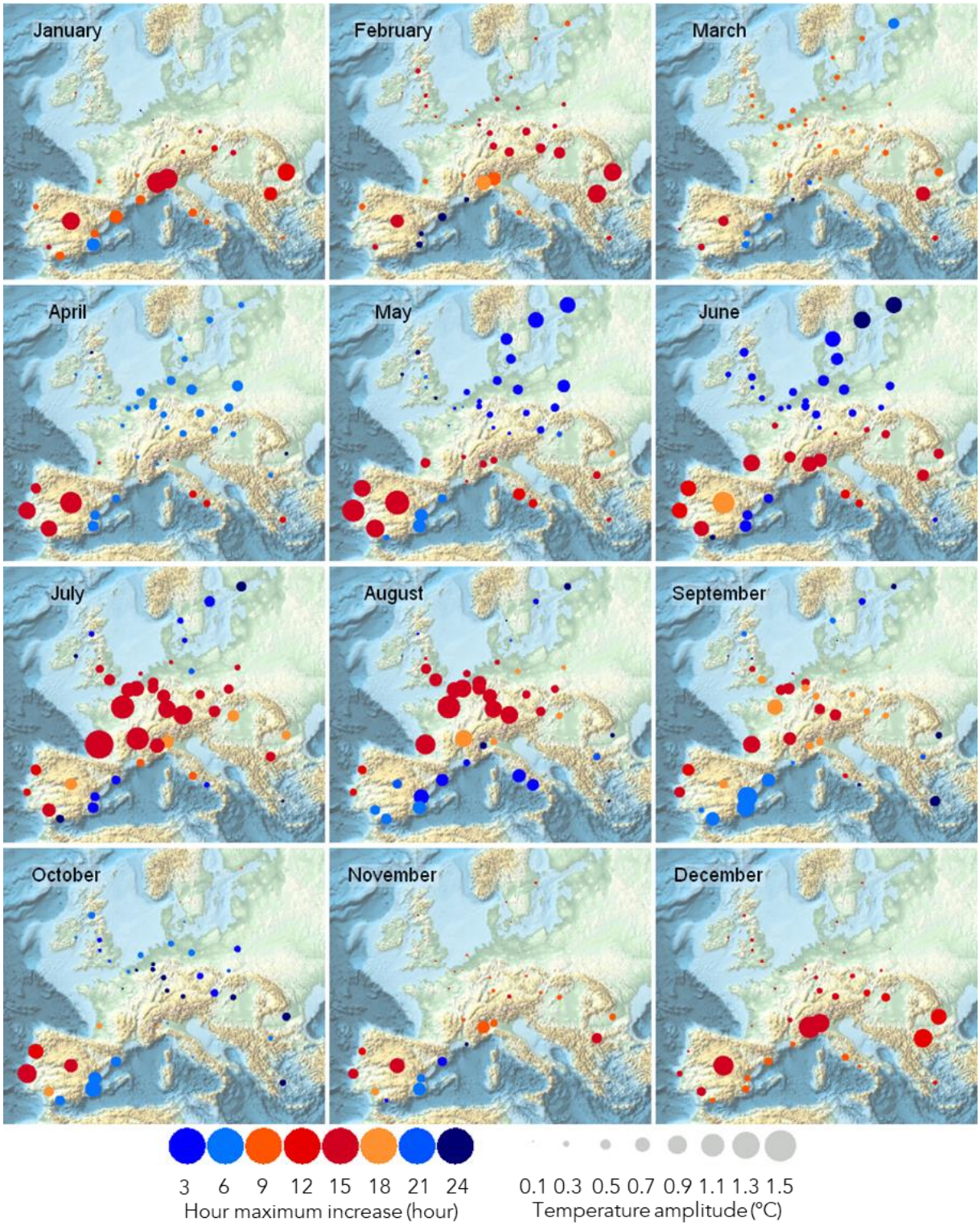

Figure 3.7 Hour of maximum monthly temperature increase and amplitude of the monthly diurnal temperature cycle.

3.3.3 Shifts NV potential

In this section, the results of the impact of upcoming temperature shifts are assessed using two different methods: suitability of air temperature for NV (section 3.3.1); and CDH and CDH reduction by wind driven and night cooling natural ventilations (section 3.3.2).

3.3.3.1 Suitability of air temperature for NV

Figure 3.8 shows differences in the number of weeks in each temperature interval between the past and future climates. As expected, climate change temperature shifts cause an extension of the periods of higher temperatures and a reduction of the colder periods. The results show four latitude-dependent clusters:

- North (from Helsinki, 60°N, to Lille, 51°N): cities without TW weeks either in the past and future dataset;
- Mid-North (from Katowice, 50°N, to Munich, 48°N): cities with TW weeks and with an increase in number of weeks of NV plus VC;
- Mid-South (from Budapest, 48°N, to Rome, 42°N): cities with a small decrease in the NV plus VC weeks;
- South (from Barcelona, 41°N, to Malaga, 37°N): cities with a considerable decrease in the NV plus VC weeks.

Table 3.3 shows the differences in number of weeks in each temperature interval between future and past climates, averaged for each cluster.

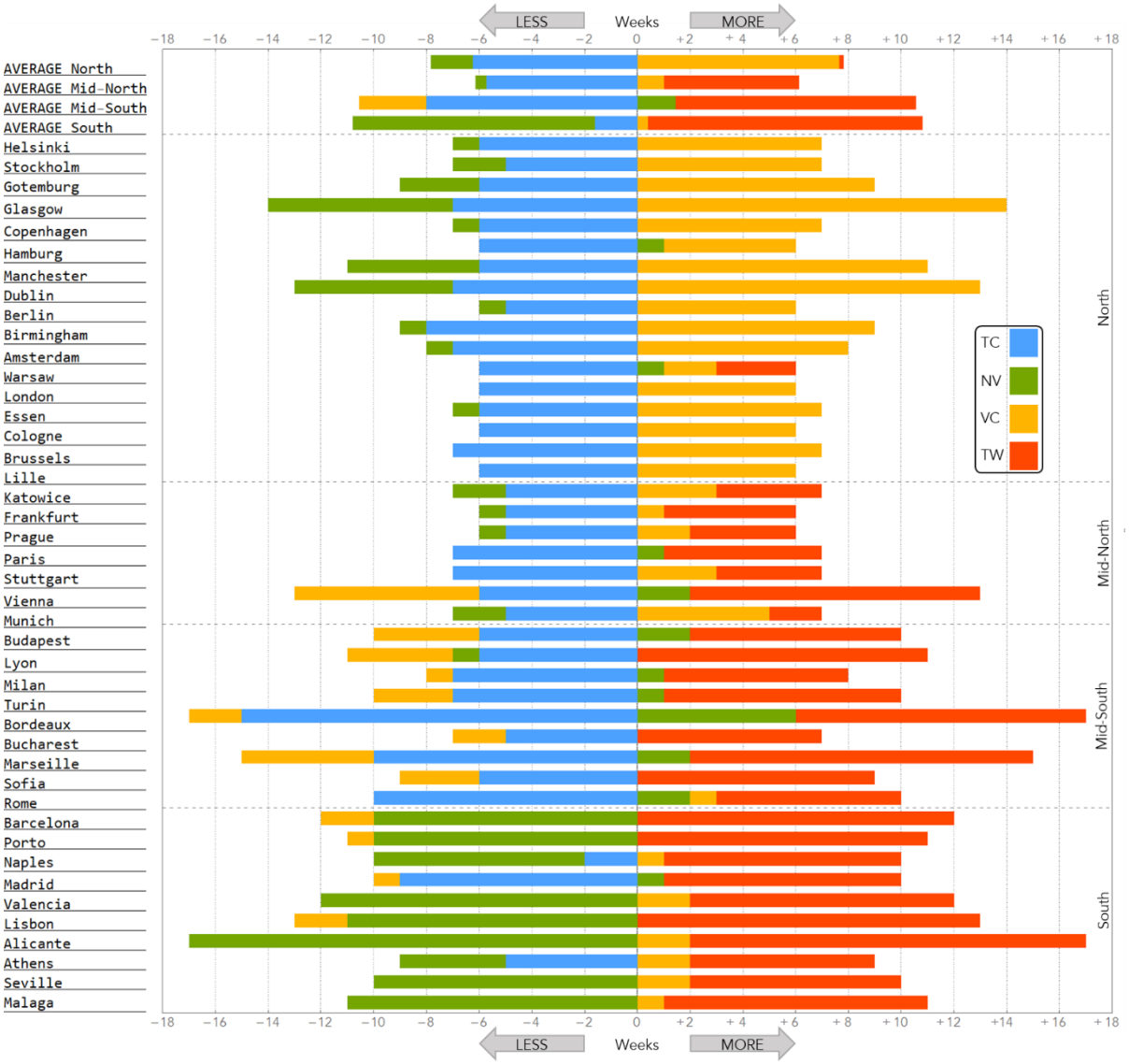

Figure 3.8 Difference in the number of weeks in each temperature interval, between past and future datasets.

For the cluster of Northern cities, future temperature increase will result in the extension of the periods when outdoor air can be used for building VC. The exceptions are Hamburg and Warsaw, which increase both VC and NV weeks. There is a 6 week increase in suitable outside conditions for NV and VC in this cluster. In the Mid-North cluster of cities there is a shift from heating to cooling demand with no significant increase in NV and VC in this cluster. The Mid-South cluster displays an even stronger shift between too cold and too warm hours with a negligible increase in NV hours. The largest variations are found in the South cluster that suffers from an initial weather that is mild and there are no TC weeks, except at Naples, Madrid and Athens. The upcoming temperature increase decreases NV weeks (9 weeks) and increases in TW weeks (10 weeks). As a result, there is a reduction of nine weeks with suitable outdoor temperatures for NV and VC. The average of the 43 cities shows that there is a five-week shift

from too cold to too warm hours, and the suitable outdoor temperatures for NV and VC remains constant.

Table 3.3 Differences in the number of weeks in each temperature interval between past and future climates, averaged for each cluster regions.

Cluster	TC (weeks)	NV (weeks)	VC (weeks)	TW (weeks)	Total NV+VC (weeks)
North	- 6	- 2	+ 8	-	+ 6
Mid-North	- 6	-	+ 1	+ 5	+ 1
Mid-South	- 8	+ 1	- 3	+ 9	- 1
South	- 2	- 9	-	+ 10	- 9
43 cities	- 5	- 3	+ 3	+ 5	-

3.3.3.2 CDH and CDH reduction by wind driven and night cooling natural ventilations

Figure **3.9** shows the CDH in past and future climates. A considerable increase in CDH is observable across Europe, with the exception of the British Isles, Amsterdam and Scandinavia where CDH increase is below 500. The largest CDH increases occur at latitude regions below 48°N, which are the regions with the highest average season temperatures and temperature increases (Figure 3.5). Considering the cluster regions defined in the previous section, the CDH increases by a factor of five and a half in the North (49 to 317 CDH), five in the Mid-North (168 to 1016), three in the Mid-South (675 to 2776 CDH), and two and a half times in the South (836 to 2828).

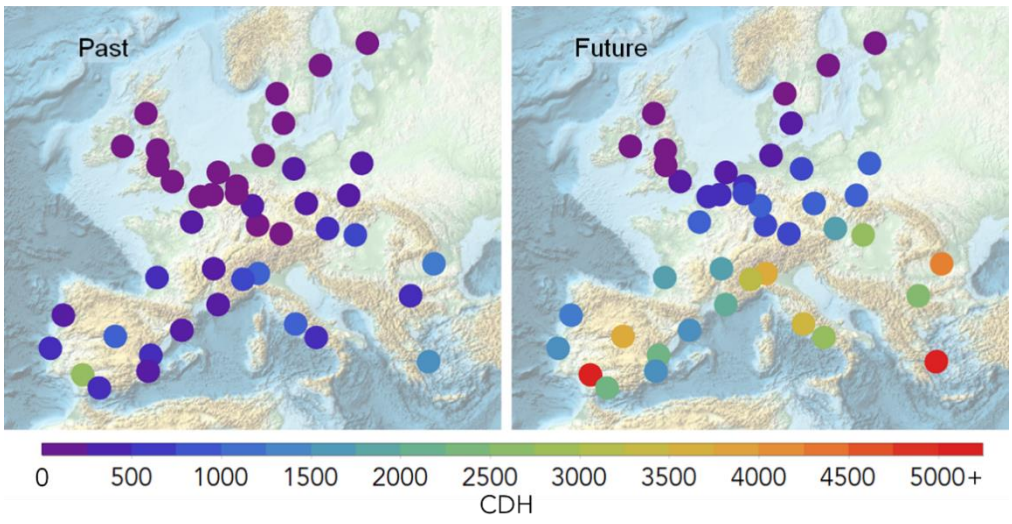

Figure 3.9 Cooling Degree Hours (CDH) for past and future climates

Figure 3.10 and Figure 3.11 show the relative reduction of CDH due to wind driven NV and NC. Table 3.4 presents the average relative CDH reduction due to wind driven, and NC for the four cluster regions. Wind driven NV relative reductions on CDH are higher in past climate than in future climate. Furthermore, cities with the lowest CDH are the ones with highest relative reductions due to wind driven NV. In opposition, cities in the Mid-South cluster show the lowest wind driven NV CDH relative reductions in both past and future climates. In future climate, this results in higher number of $CDH_{res\text{-}WD}$ in Mid-South (1767 CDH) than in South cluster (1645 CDH), due to lower average wind velocities during the $CDH_{res\text{-}WD}$ periods (2.7 m/s and 3.2 m/s for Mid-South and South cities). Additionally, differences between coastal and continental cities are observable, with coastal cities having greater reductions due to lower averages temperatures (Figure 3.5) and higher wind velocities.

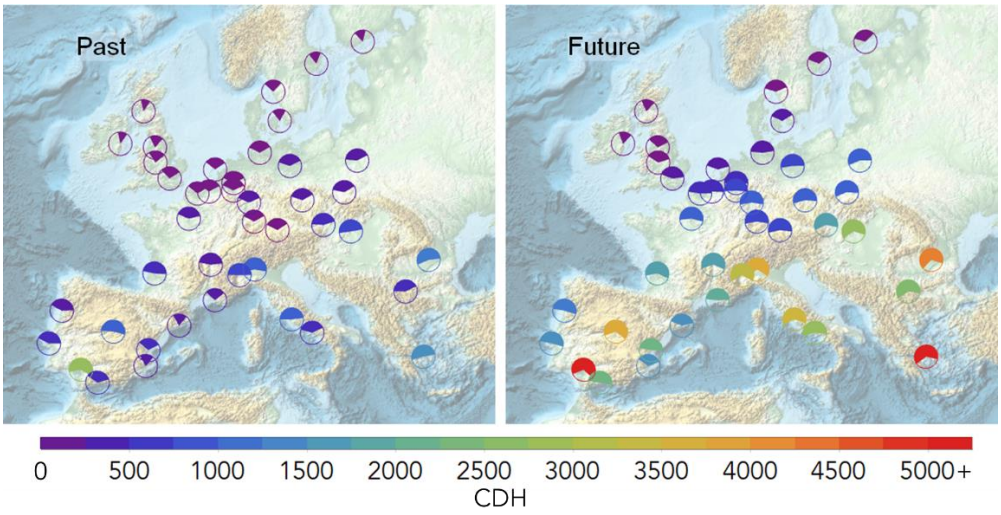

Figure 3.10 CDH (colour scheme) and CDH relative reduction due to wind driven NV (%)

Table 3.4 Average relative CDH reduction due to wind driven and night cooling ventilations in the four clusters for past and future climates.

Cluster	CDH wind driven NV reduction		CDH night cooling reduction	
	Past	Future	Past	Future
North	73 %	60 %	88 %	58 %
Mid-North	62 %	44 %	84 %	39 %
Mid-South	53 %	38 %	67 %	23 %

South	61 %	47 %	70 %	27 %

Regarding NC, in past climate, the great majority of CDH are reduced using this ventilation strategy. In future climate, the effectiveness of NC is reduced to less than half, except for North cluster. In Mid-South and South clusters, the capacity to reduce CDH using NC is reduced to just 23 % and 27 %, respectively, and is a consequence of a considerable increase in the minimum temperature (3 °C in both clusters) and a reduction of the DTR (1 °C in both clusters) during $CDH_{res\text{-}NC}$. Further, differences between Mediterranean and Atlantic coast cities are observable. Mediterranean cities have substantially less capability to use NC to reduce CDH, in contrast with the cities in the Atlantic coast (Bordeaux, Porto and Lisbon), where lower <temperatures (Figure 3.5) and an increase in DTR is expected (Figure 3.7).

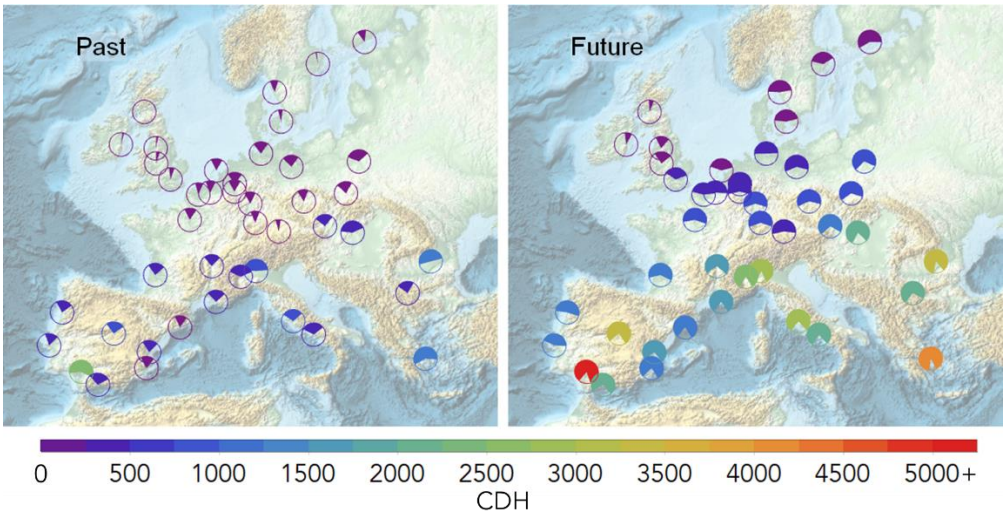

Figure 3.11 CDH (colour scheme) and CDH relative reduction due to night cooling (%)

3.3.4 Days with similar maximum temperature

This section compares daily records of past and future climates grouped according to the daily maximum air temperature (in 1 °C intervals). Figure 3.12 show the cluster average changes of the first and last day, DTR, total daily radiation and direct solar radiation. The results of the average maximum solar altitude are shown for the most populated city in each cluster region in Figure 3.13. The average wind speed changes are almost inexistent (slight increase), and therefore are not presented.

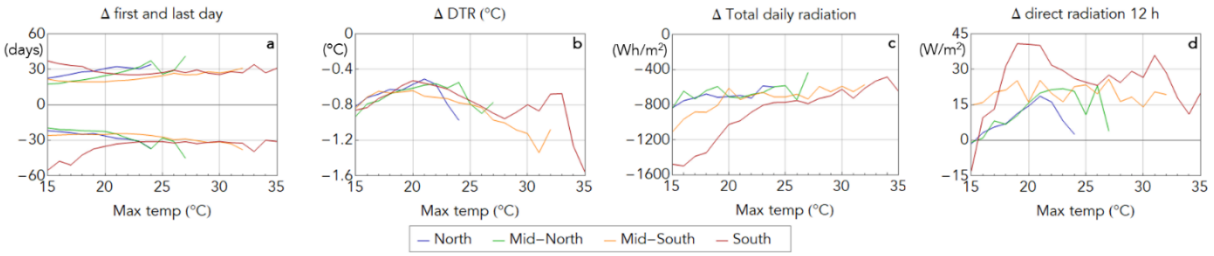

Figure 3.12 Average first and last day, DTR, total daily radiation, and direct solar radiation at solar noon incident on a south facing façade differences between future and past climates for days with similar maximum temperature.

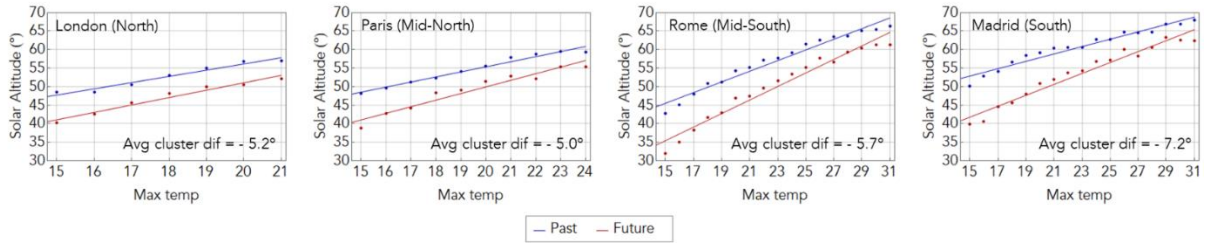

Figure 3.13 Average maximum solar altitude at London (North), Paris (Mid-North), Rome (Mid-South) and Madrid (South) for days with similar maximum temperature.

The first and last day in each temperature interval are shifted almost symmetrically, occurring approximately 1 month earlier and later. The exception are cities in South cluster, where days occur earlier (35 days) by a higher magnitude than the postponement of the last day (29 days). The preponing and postponing of days with similar maximum temperature is important, for example, for the design of shading devices (see Section 3.3.5). A decrease of the DTR occurs in all clusters, confirming the analysis of $CDH_{res\text{-}NC}$ (which expect a reduction of efficacy of NC ventilation), especially in Mid-South and South clusters where the DTR reduces significantly with the increase of mean maximum temperature. The results of the DTR and wind speed support Section 3.3.3.2's results of higher reduction due to wind driven NV than NC in future climate. Solar altitude and total daily radiation decrease considerably, as similar maximum temperatures occur earlier and later in the year. However, the decrease in solar altitude increases the incidence of direct solar radiation on south façades. This increase results in additional solar gains, which may disturb the designed energy balance.

3.3.5 Optimal overhangs and solar gains

In this section, a fixed horizontal overhang is designed for past and future climates, and changes in direct solar radiation incident on a south facing façade and window are analysed.

Figure 3.14 shows the OLR of past and future climates. In past climate, cities north of the latitude of Budapest (except for Vienna) do not require any shading. On the other hand, cities

south of Budapest (except for Porto) require the use of an overhang, with an average OLR of 0.54 for Mid-South cluster and 0.59 for South cluster (excluding Porto). In future climate, only Scandinavia and the British Isles (excluding London) have no need for a fix horizontal overhang. The rest of Europe shows an increasing need of shading devices in their building design and an enlargement of OLR. Future average OLR in North (excluding the 8 cities which do not need an overhang) and Mid-North clusters are respectively 0.69 and 0.72, which are higher than those of southern Europe in past climate. In Mid-South and South clusters, the shading season starts and ends on average 38 days earlier and later. However, the maximum solar altitude varies differently in the two clusters (decreasing 12° in Mid-South, and 15° in South), due to different starting shading season dates. These results in average increases of 60 % and 69 %, corresponding to future average OLR of 0.86 and 1.00, in Mid-South and South clusters. The increase in overhang length is difficult to add to existing buildings and can be impracticable to implement due to architectural constraints.

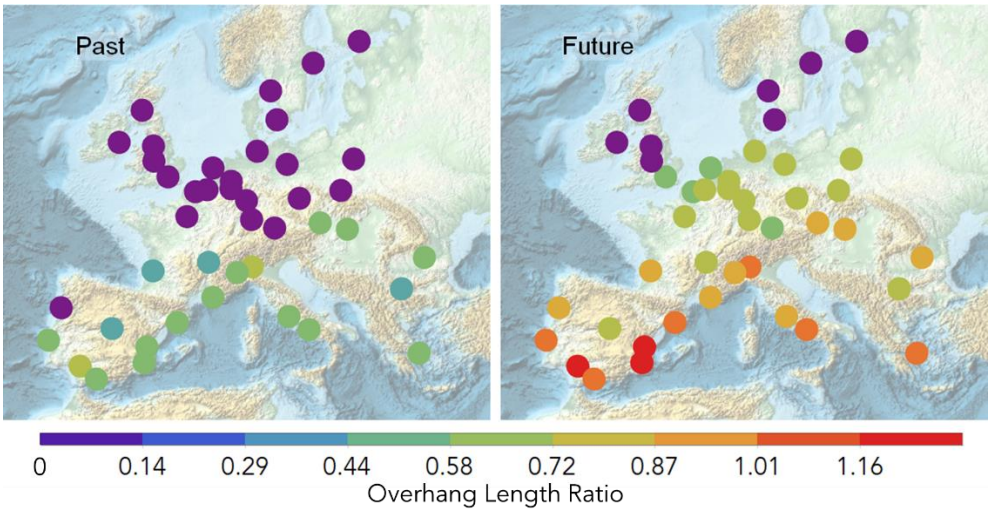

Figure 3.14 Overhang length ratio (OLR) for past and future climates

Figure 3.15 show the $I_{direct,façace}$ results of PP and FF scenarios. Direct solar radiation on a south facing façade increases on average 35 % from PP to FF, despite FF occurring on average 38 days earlier/later and solar altitude is on average 13.5° lower than in PP. The increase in direct solar radiation is almost exclusively due to changes in solar altitude (average increase of 29 % between FF an PF), while solar radiation changes are almost inexistent (average increase of 5 % between FF and FP, except in Lille, Brussels and Stuttgart which increase 20 %).

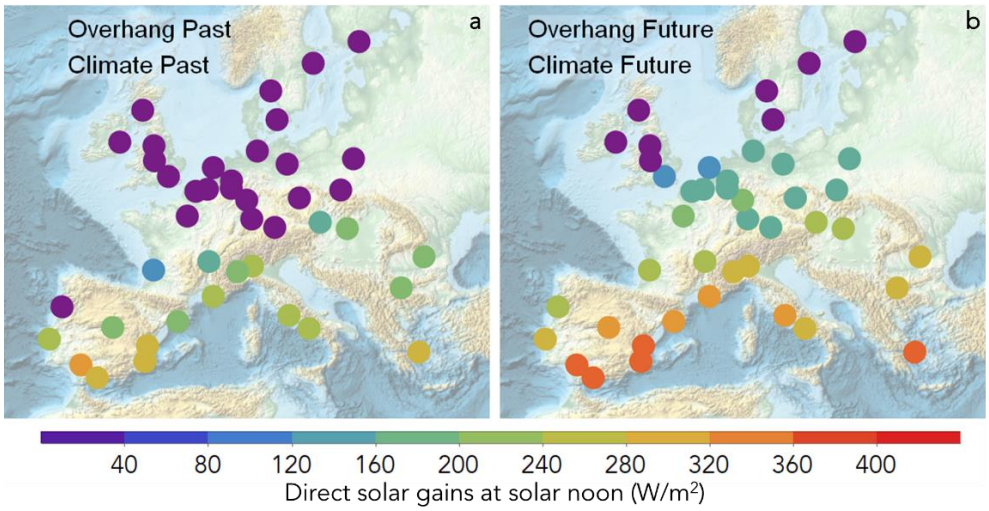

Figure 3.15 Incident direct solar radiation on a south facing façade at solar noon in the optimal overhang day of past climate, PP (a); and future climate, FF (b).

3.4 Conclusions

This chapter assessed climate change effects on end-of-century air temperature, wind and solar radiation and its impacts on passive building strategies. The analysis focused on upcoming changes in the shape of days and annual shifts in air temperature. Overall results show that, with the exception of Scandinavia and the British Isles, all off Europe will suffer from reduced effectiveness of passive building strategies. In the rest of Europe, and especially in Mid-South European cities, the temperature increase will lead to more overheating and cooling energy demand, which will be exacerbated by a growth in direct solar gains in increasingly warm early spring and autumn periods. The main conclusions of this chapter are:

- Climate change will affect the shape of the diurnal temperature cycles, either increasing (daytime shape) or decreasing (nighttime shape) the DTR depending on the season and region.
- Daytime shapes occur during the heating season, resulting in the increase of heating demand in residential buildings and decrease in commercial buildings (Northern Italy), and during the cooling season, reducing the NV and increasing the NC availabilities in mild summer climates (France and Germany), and increase the cooling demand in hot summer climates (Western Iberia).

- Nighttime shapes occur mostly during the cooling season, resulting in more NV and less NC effectiveness in mild summer climates (Northern Europe), and less cooling demand in climates with hot summers (Mediterranean coast).
- Upcoming shifts in the annual temperature distribution will increase in 6 weeks the number of suitable weeks for NV and VC in Northern Europe. In contrast, in South European cities, there will be a 9 week shift from NV to warm weeks. In the rest of Europe, there is a shift from heating to cooling demand, with the number of NV and VC weeks being almost constant.
- The effectiveness of passive building cooling strategies will change, shifting the most effective strategy from NC to wind driven NV. Still, the potential of wind driven NV to reduce CDH will be reduced to less than 50 % in most of Europe.
- By the end of this century days with similar maximum temperature will occur one month earlier/later and will have increased direct solar radiation on south facing windows.
- South facing horizontal overhangs will become less effective because the shading season will increase by approximately 2.5 months and have a reduced average maximum solar altitude (13.5° lower). As a result, there will be a 35 % increase in direct solar gains incident on a south façade.

Chapter 4 - Using building thermal mass energy storage to offset temporary BIPV output reductions due to passing clouds in a cooling dominated office building

4.1 Introduction

There are several comprehensive reviews on building demand flexibility [45, 153], as well as a reviews focused on heat pump-based flexibility [51]. More pertinent to the present work are studies that analyse the combination of onsite PV production and building demand flexibility. In Oslo (Norway), a nearly zero energy residential building with a heat pump was simulated with a control strategy that operates the heat pump when PV production surpasses existing non-heating electrical loads, resulting in an RE self-consumption improvement of 40 %, reducing the purchased grid energy by 20 %, with a reduction of 30 % in the hours of peak exchange with the grid (periods when grid import/export surpass a defined threshold [154]). In a residential building in Finland, the simulation of a control strategy to consume PV excess production increased PV self-consumption by up to 70 % with direct electric heating and up to 40 % using a heat pump for space heating and DHW [155]. A study in Denmark focusing on two low-energy buildings in the heating season (a single-family house and an apartment block) used dynamic simulation to analyse periods of excess (storage) and shortage (curtail) of RE production and found that buildings can maintain thermal comfort for several hours. In these buildings the potential for storage was found to be higher than the potential for curtail. The results show that the flexibility potential is governed by heat loses, with internal walls having a higher contribution to the thermal capacity than exterior walls [156]. This study also compared cloudy and clear sky days, finding that increased solar gains result in lower flexibility both in storage and curtail events. In Germany, a simulation-based study analysed the energy flexibility of a single-family house equipped with a heat pump and a buffer storage device [157]. The system demand flexibility was triggered by external signals from RE production. Results show that, in this case, load shifting causes an increase in electric energy consumption up to 19 % (with no impact on comfort). In Belgium, a simulation study of 33 nearly zero energy single-family dwellings equipped with heat pumps and PV systems showed that, using very basic control strategies, curtailment can be reduced by up to 74 %, with thermal energy storage in DHW tanks proving to be very effective [158]. Another simulation study in Belgium used 15-minute weather data of a single-family dwelling equipped with PV and a heat pump to conclude

that structural storage capacity has the potential to shift heating demand to off-peak hours (up to 94 %), and heavy weight buildings with heated floors have the highest potential for peak shaving [48]. In Italy, a simulation based study of a residential building with a heat pump powered by a PV system showed that imported energy can be reduced by up to 22 % and exported energy by 12 % [54], compared to a baseline case with no demand flexibility actions. In Portugal, an experimental study of three living rooms in three buildings with different thermal insulation levels tested the potential of preheating during the afternoon (using excess PV production) to avoid heating demand in the evening hours. The results of this study show that rooms with high thermal mass and high envelope insulation have BaB thermal storage efficiencies up to 80 %, while in poorly insulated buildings BaB is only effective in short term applications (two hours or less [159]). In Scotland, the lobby of an office building heated by a heat pump that uses RE energy from a wind turbine was simulated for a period of four winter days. Results showed that, although energy consumption increased, operation costs and carbon emissions were reduced [160]. In Portugal, numerical simulations of the flexibility provided by battery energy storage systems in a passive office building with a PV system were performed using onsite measured consumption and generation data [161]. This study found that the battery system improved load matching and grid interaction. In Italy, the simulation of an industrial building with thermal energy storage charged by heat pumps showed that shifting energy demand for space cooling to weekends to use surplus PV production and purchasing electricity with low prices, resulted in increased energy use and significant cost savings [162]. In Washington D.C. (US), a demand response in a medium-sized office building with a PV system was simulated for one summer day, resulting in the reduction of peak load in 64 % and overall energy consumption in 33 % [163]. In Austria, a simulation-based study of a standard office building with a PV system and shiftable loads, using 15-min data, indicated that the energy demand during high-tariff periods can be reduced by 35 % [164].

An interesting opportunity for energy flexibility occurs when clouds that are passing over a building shade its BIPV system. In this scenario, one approach to avoid increased grid demand during these events is to turn off the HVAC system. In office buildings, in the summer or even in mid-season months, this control action will result in an increase in indoor air and surface temperatures that is limited by thermal energy storage in the building internal mass (the BaB system). Once the cloud passes, BIPV production rises and the HVAC system can be turned back on, ensuring that indoor temperatures return to its original state and avoiding the up ramp in BIPV grid injection. To fully exploit this approach, there is a need to understand how long

the shading by passing clouds typical lasts. In most climates cloud occurrence varies greatly throughout all timescales (from day to year), still, there are very few studies that focus on yearly cloud distribution. A study in Tampere, Finland, showed that 89 % of shading periods last less than 2 minutes and only 0.6 % are longer than 10 minutes. The study also showed that, in this Nordic climate, spring months have less cloud events than summer and autumn, with an average yearly cloud velocity of 13 m/s [165]. To evaluate the potential of that system including building-grid interactions there is a need to use measured solar radiation data with high temporal resolution [166,167]. The impact of smaller cloud shading periods that last a few minutes can also be mitigated using an HVAC off approach but are clearly less of a problem from an indoor environment perspective and will have a smaller impact in the building energy budget. Further, it is important to recognize that most shading periods may be too short to justify any action on heat pumps that generally do not respond well to short term on/off actions. One known strategy that can be used to avoid excessive changes in grid injection is to limit BIPV production. Clearly this can be done for short periods (a few minutes a day) without a relevant impact in overall production. Therefore, from the perspective of HVAC off based demand flexibility the focus on shading periods should be in longer periods ranging from ten minutes up to an hour, which tend to be scarcer.

Several existing studies show that demand flexibility combined with energy storage can significantly increase onsite RE use. Yet, in the case of the most commonly available systems for RE production and storage, BIPV and BaB, there is no study of their combined performance when responding to intraday variations in solar radiation availability caused by passing clouds. In addition, there are no validated thermal energy simulation models for BaB based flexibility events in office buildings. This chapter addresses these complementary research gaps in three different tasks:

1. Characterize the duration and time of occurrence of passing clouds that can impact BIPV production and trigger demand flexibility events in different climates.
2. Produce a validated dynamic thermal energy simulation model of an open space office.
3. Analyse the potential reduction in grid energy demand and increased onsite BIPV energy consumption by using HVAC demand flexibility triggered by fluctuations in BIPV production in a large, air-conditioned office building.

The next section presents the methodology used in this chapter. The following subsections present the weather data and the flexibility event measurement campaign. Sections 4.2.2 and

4.2.3 present the open plan office and whole building energy simulation models. Section 4.3 presents the result and discussion, followed by the conclusions in section 4.4.

4.2 Methodology

The research methodology used in this chapter is composed of four sequential steps shown in Figure 4.1:

1. Using high sampling rate measured weather data, characterize, in different climates, shading periods caused by passing clouds (Section 4.2.1.1).
2. Measure a flexibility event in an open plan office space (Section 4.2.2.1).
3. Calibrate a dynamic thermal simulation model for the open space using results from step 2 (Section 4.2.2.2).
4. Simulate demand flexibility events triggered by fluctuations in BIPV production to predict grid electrical energy demand and indoor thermal comfort with different HVAC system control scenarios (Section 4.2.3).

The first step aims to characterize the duration and time of occurrence of shading by passing clouds. This characterization requires measured solar radiation data with one-minute time resolution which is not widely available. Based on data availability and the need to have a reasonable diversity in climates, five weather stations were chosen, four in the US and one in Portugal. The next section presents more details about the weather data.

The second step of the methodology consists in a real-world flexibility event in which the HVAC of an occupied open plan office space was turned off for 128 minutes during a typical mid-season weekday morning. During the event, occupation, space electric loads, indoor temperature humidity and CO_2 were measured. The measurements were performed in a large office building located in Seixal, near Lisbon, Portugal.

The third step used the results of the measurement campaign to calibrate an EnergyPlus dynamic thermal simulation model of an open plan office space. In the fourth and final step a whole building model that included a large BIPV system was used in combination with high-resolution weather data for Lisbon to assess the capabilities of BaB storage to reduce grid

electrical energy demand while maintaining indoor thermal comfort. The whole building simulation used four different scenarios:

1. No flexibility (BS-22). A reference scenario with HVAC cooling setpoint set to 22 ºC, as defined by the building manager.
2. No flexibility (BS-24). Similar to 1 but the HVAC cooling setpoint was set to 24 ºC.
3. Flexibility triggered by cloud shading periods (CL-24). The AHU was turned off whenever a cloud shading period identified in Section 4.2.1.1 occurred, while the fan coil cooling setpoint temperature was changed to 24 ºC.
4. Flexibility triggered by BIPV production shortages (PV-24). The AHU was turned off whenever HVAC energy consumption was higher than BIPV production, while the fan coil cooling setpoint temperature was changed to 24 ºC.

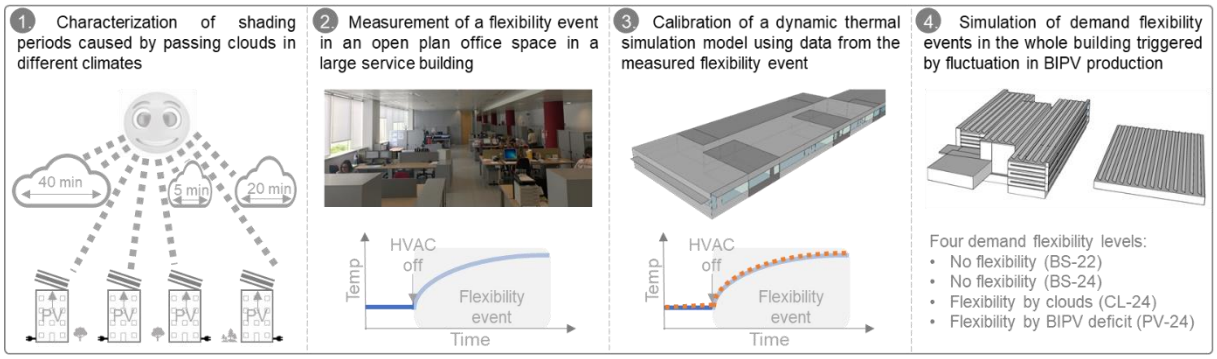

Figure 4.1 Schematic representation of the four sequential steps

4.2.1 Weather data

This chapter performed the different analysis, represented in Figure 4.1, using weather observation data from three different sources:

1. Step one in Figure 4.1, the characterization of time of occurrence and duration of cloud shading periods, used measured climate and solar radiation data of four US cities.
2. Step two in Figure 4.1, the measurement of the indoor conditions during a flexibility event in an open plan office space, used weather data that was measured in an onsite weather station.

3. The fourth step of the methodology, the whole building thermal simulation, used data from a weather station located in the University of Lisbon campus.

The data used in step 1 included four US cities and Lisbon:

1. Boulder (40º N, 105º W): January 1st 2015 to December 31st 2019 [168].
2. University of Oregon (44º N, 123º W): September 1st 2016 to August 31st 2019 [169].
3. Oak Ridge (36º N, 84º W): January 1st 2011 to December 31st 2016 [170].
4. Phoenix (33º N, 112º W): January 1st 2011 to December 31st 2012 [171]
5. Lisbon (38º N, 9º W): April 1st 2020 to October 31st 2020, this data is also used in step 3).

The study of Step 1 in Figure 4.1 focused on US cities since there is no public available data for Portugal or Europe with 1 minute resolution. The four cities were chosen from a total of eight cities analysed which had data with 1 minute resolution and a minimum record of 2 years.

The measured data used in step 2 was recorded on the 20th of November 2017. The measured parameters were dry bulb temperature, relative humidity, wind velocity and direction, global and diffuse horizontal irradiance (all with one-minute timestep). This weather data and internal indoor conditions were also used in the calibration of the dynamic EnergyPlus thermal simulation (step 3 in Figure 4.1).

Finally, the third dataset, is composed of data obtained in a weather station located in the campus of the University of Lisbon. The weather station records the following parameters, with one-minute timestep: dry bulb and dew point temperatures, relative humidity, atmospheric pressure, wind direction and velocity, global and diffuse horizontal irradiance, and direct normal irradiance. This weather dataset spans from the 1st of April 2020 to the 31st of October 2020. In this period there are 21 days (not all consecutive) with missing data, which were discarded when analysing the results. For simulation purposes, days with missing data were substituted by the previous complete day and, to avoid discontinuities and large variations in the transition between days, a cubic spline curve fitting technique was applied to the last and first 2 hours (total of 240 data points) of each replaced day. This resulted in 137 **(**out of 153) weekdays that were considered for demand flexibility events. This dataset was also used to characterize the shading periods for Lisbon (step one).

4.2.1.1 Characterization of cloud shading periods

In each weather data point, shading periods were identified quantitatively using the ratio between global horizontal radiation (G) and extra-terrestrial incident irradiance (G_0):

$$k_t = G/G_0. \quad (4.1)$$

This ratio, known as the clearness index (k_t) [172], is commonly used to identify cloudy and clear sky conditions. Unfortunately, there is a lack of scientific consensus about the thresholds [173] used to identify clear sky or cloudy conditions. A review of existing thresholds revealed the following range of values:

Clear sky for: $k_t > 0.5$ [174], 0.6 [175], 0.65 [176], 0.7 [177].

Cloudy sky for: k_t between: 0.25 and 0.5 [174], 0.2 and 0.6 [175].

In this context, this chapter defined each of the thresholds using the average value of existing studies. Clear sky conditions were defined when k_t above 0.6, and the cloudy (shading) conditions were defined as k_t below 0.4. The gap between the two thresholds ensures a significant difference in BIPV production between the two sky conditions. The present characterization of cloud shading periods is tailored for the purpose of triggering BaB activation through HVAC off events. In this context, there is a need to register the time of occurrence during the day and year as well as the type of day when it occurs (cold, mild or warm). Cloud classification was based on the following set of rules:

1. Clear sky conditions occur when kt > 0.6, and cloudy sky condition when kt < 0.4.
2. Every day, after the sun altitude rises above 10º and a period of clear sky conditions longer than 15 minutes has occurred, the system starts searching for clouds.
3. Three-minute interruptions in the clear sky conditions do not stop the registering of a clear sky event.
4. Once the system detects 5 minutes of cloudy sky conditions, a cloud event begins to be registered.
5. One-minute interruption in the sky conditions do not stop the registering of an ongoing cloud event.
6. The registering of cloud events stops when the sun altitude lowers bellow 10º.

Finally, days were classified in three different categories according to the sky conditions during the day:

- Cloudy days: days with constant cloudy sky conditions.
- Days with cloudy periods: days that registered at least a cloudy period as previous defined.
- Sunny days: days with constant clear sky conditions.

After applying the rules above to the weather data, the number of cloud periods, their duration, time of day of occurrence and number of events per day was calculated and analysed for sets of days with the same maximum daytime air temperature.

4.2.2 Office building test case

The measurement of a BaB based energy flexibility event was performed in the Seixal City Hall service building (Figure 4.2). In addition to the experiments, this building was also used as model for the whole building thermal simulation presented below.

Seixal is a city on the south banks of Tagus river, 5 km south of Lisbon (Portugal). The building has 15000 m^2 of floor area distributed in four blocks that surround a large naturally ventilated atrium [178]. The two largest blocks, named North and South buildings, have three levels of office spaces. Each floor is divided in a large open space (facing the outdoor facade) and small offices (facing the atrium). Below the ground floor sits a partially underground area composed of small offices, storage spaces and a garage. At the eastern edge of the atrium, there is a small building with two floors for storage and cafeteria. The fourth block sits in the north-western edge and houses a small auditorium that is used only in special events.

The office workspaces are heated and cooled by ceiling fan coil units. Fresh air is provided by centralized air handling units located in the roof (AHU). Centralized heating and cooling are provided by several heat pumps also located in the building roof. The South building has horizontal overhangs on the windows located on the south and west façades and on the edges of the south façade. The North building has horizontal overhangs on the windows of the west façade and on the last floor of the north façade and has vertical overhangs on the edges of the building. Currently the building does not have any BIPV. For the purpose of this study a

simulation model of the building with BIPV system was developed. The panels are located on the top of the atrium, the two main building blocks and the adjacent parking lot (Figure 4.1.4).

The BaB demand flexibility event measurements were performed on an open plan office space with a total area of 341 m^2 and 3.0 m of floor-to-ceiling height located on the western part of the 1st floor of the south building block (Figure 4.2). The open space has a raised floor with an air gap of 0.3 m, and a drop ceiling with a 0.5 m airgap. Inside the open space there are two rooms with 45 m^2 each used for meetings and storage, at the eastern edge there is another small room and a second open space, and at the northern part a wall divides the open space from a corridor and other small rooms (Figure 4.1.3).

Figure 4.2. Aerial view with the open space used in the measured campaign highlighted (left), and interior view of the measured open space (right).

4.2.2.1 Full scale measurement of a flexibility event

The demand flexibility event consisted in turning the HVAC system of the open space off for 128 minutes (starting at 9:48 a.m. on the 20th of November of 2017). During the event, indoor air temperature, humidity and CO_2 were measured every minute, using nine sensors located at different parts and heights of the open space. Additional measured quantities included space total electric load (lighting and equipment), counting the number of occupants every ten minutes, and local weather (with a portable weather station). The infiltration of the open space was measured on 17/11/2017 by monitoring the CO_2 concentration decay in the evening, after a workday (unoccupied space with HVAC off). Due to the importance of internal mass for BaB thermal response, the measurement campaign included a survey and estimation of the mass of all objects in the open space (furniture, paper stacks).

4.2.2.2 Calibration of the thermal simulation model

The dynamic thermal energy simulations were performed using EnergyPlus (version 8.7 [179]). The boundary conditions of the open space were defined by using several adjacent thermal zones. The geometry of the simulation model is shown in Figure 4.1 (column 3): two small rooms on the south facing façade, a stairway, WC and a group of offices at the northern part; a connection to the other open space and a small room at the eastern edge, the basement and the 2nd floor were also defined as different thermal zones. The raised floor and dropped ceiling were modelled as independent thermal zones. The construction and building materials used in the simulation are shown in Table 4.1. The office wall construction was used as the boundary layer between the open space and the small rooms on the south facing façade, while other interior divisions were defined using the interior wall construction. The windows were double glazed with low emissivity (U-value of 1.2 W/m^2/K, solar factor of 0.41), and internal shading was always on ("WindowMaterial:Shade") in the south facing windows.

Table 4.1 Building constructions and materials

Construction	Material	Thickness (m)	Conductivity (W/m/K)	Density (kg/m^3)	Specific Heat (J/kg/K)
Raised Floor	Wood Floor	0.04	0.14	650	1200
Exterior Wall	Plaster	0.015	1.3	1900	1000
	EPS	0.04	0.04	15	1400
	Brick	0.15	0.38	1000	1000
	Air space	0.10			
	Brick	0.11	0.41	1000	1000
	Plaster	0.015	1.3	1900	1000
Interior Wall	Plaster	0.015	1.3	1900	1000
	Brick	0.11	0.41	1000	1000
	Plaster	0.015	1.3	1900	1000
Drop Ceiling	Aluminium sheet	0.002	204	2700	890
Interior FloorCeiling	Concrete	0.25	1.35	1800	1000
Exterior Wall-Earth	Earth	0.5	0.52	2050	180
	EPS	0.04	0.04	15	1400
	Brick	0.15	0.38	1000	1000
	Concrete (lightweight)	0.04	0.57	608.7	830
	Brick	0.11	0.41	1000	1000
	EPS	0.03	0.04	15	1400
	Plaster	0.015	1.3	1900	1000
Exterior Floor-Earth	Earth	0.5	0.52	2050	180
	Earth .2	0.5	0.52	2050	180

	Concrete	0.25	1.35	1800	1000
	Concrete (lightweight)	0.15	0.38	1200	1000
	Air space	0.30			
	Wood Floor	0.04	0.14	650	1200
Exterior Floor-Ceiling-Air	EPS	0.03	0.04	15	1400
	Concrete	0.25	1.35	1800	1000
Office Wall	MDF	0.01	0.18	800	1700
	Brick	0.07	0.41	1000	1000
	MDF	0.01	0.18	800	1700

Accurate modelling of internal mass is central to BaB based demand flexibility simulation. There are two approaches for internal mass simulation in EnergyPlus [180]. The most commonly used is called "InternalMass" and requires a definition of the materials and the exposed surfaced area of the objects that contribute to the zone internal mass (furniture, internal walls, stack of paper, etc.). This information is then used to create an internal object in the zone that participates in the zone air heat balance and longwave radiant exchange but does not receive direct solar gains [180]. The characteristics of the objects that contributed to the internal mass of the open space that was analysed in this chapter are shown in Table 4.2.

Table 4.2 Internal mass objects, quantity, and material characteristics.

	Cabinet 1.7 m	Cabinet 1.5 m	Cabinet 0.8 m	Cabinet w/ wheels	Desk (Wood)	Desk Separator (Wood)	Paper (5 kg/desk)	Paper (50 % cabinets, Pen. depth 0.01 m)
Number	3	29	10	38	60	30	-	-
Specific Heat (J/kg/K)	447				1200		1400	
Density (kg/m^3)	7870				800		1200	
Thickness of the material (m)	0.002				0.04		0.07	
Conductivity (W/m/K)	72				0.15		0.042	
Penetration Depth (m)	0.9				0.08		0.03	

The second simulation approach incorporates the thermally active part of the internal mass in the zone air thermal capacity. This approach, called "ZoneCapacitanceMultiplier:ResearchSpecial" [179], relies on a temperature capacitance multiplier that adds the effective storage capacity of the internal mass to the thermal capacitance of the air in the thermal zone. For the simulation with the "ZoneCapacitanceMultiplier:ResearchSpecial", the heat capacity of the different components contributing to the internal mass of the building have to be calculated using Equation 4.2 [181]:

$$C = V\ \rho\ C_p \qquad (4.2)$$

Where C is the heat capacity, ρ the density of the material, C_p the specific heat capacity of the material, and V the volume which is calculated by multiplying the exposed surface area by the thermal penetration depth (δ_p) of the room air temperature in the material during the event (Equation 4.3) [181].

$$\delta_p = 2.3\sqrt{\frac{k\ t}{\rho\ C_p}} \qquad (4.3)$$

Where k is conductivity, and t the duration of the event. The zone capacitance multiplier (C_T) is then calculated using [179]:

$$C_T = \frac{Cz}{V\ \rho_{air}\ C_p} \qquad (4.4)$$

Where C_z is the total heat capacity of the zone (internal thermal mass plus air capacitance).

4.2.3 Whole building thermal simulation model

A whole building simulation model was developed to perform a full evaluation of the BaB demand flexibility strategy. The model geometry is shown in column 4 of Figure 4.1. In this model, each floor of the two main building blocks was divided in two zones, one for the open spaces and another zone for the single offices facing the atrium. The south building block is longer than the northern block, and, as a result, was divided into two thermal zones. The first zone has the same length of the northern block and is called South. The second, additional, smaller zone contains the western edge of the building and is called Southwest. The remaining two floors of the main building blocks are similar to the first floor.

The building weekday occupancy used the maximum occupant density measured in section 4.2.2.1 (0.14 person/m^2). The variation of the occupation throughout the day used the non-

dimensional profile recommended by [182]. People were modelled considering an activity level of 100 W/person, a radiant fraction of 0.4 and CO2 generation rate of 3.82 x 10-8 m3/(s W). The CO2 concentration was simulated using the "ZoneAirContaminantBalance" considering an outdoor concentration of 400 ppm. The office electric equipment and lighting gains were defined as 12.36 W/m^2 and 7 W/m^2 (the average recorded values during the flexibility event, section 4.2.2.1). Lighting, equipment and HVAC were on between 8 a.m. and 7 p.m.. During the night, lights and equipment were off in offices and corridors and down to 5 % of the maximum power in the atrium and garage (only lights).

The office fan coils and AHU were simulated using the "HVACTemplate:Zone:FanCoil" simulation object coupled with a "HVACTemplate: System:DedicatedOutdoorAir", set according to the installed capacity in the building that total 19.546 m3/s (cooling design air flow rate: 4.629 x 10-3 m3/(s m2) on the Southwest zone, 3.180 x 10-3 m3/(s m2) on the South zone, 3.205 x 10-3 m3/(s m2) on the North zone, and the remaining zones with an average value of 3.193 x 10-3 m3/(s m2)), with a cooling setpoint of 22 ºC (the setpoint used by the building manager, verified in the flexibility event described in section 4.2.2.1). The electric energy consumption of the fans of the AHU was calculated using the total specific fan power, the sum of inflow and exhaust values of the equipment currently installed in the building (4431 W/m^3/s). The electrical energy use of the fan coils was calculated using:

$$\mathrm{E}_{vent} = \frac{P_{vent}\ \dot{V}}{\eta_{vent}} \qquad (4.5)$$

More specifically, E_{vent} was calculated using the volume flow rate ($\dot{V}$) predicted by the simulation model, an average fan coil pressure drop (P_{vent}) of 71.5 Pa, and an average fan efficiency (η_{vent}) of 50.1 % [183]. In each timestep, the coefficient of performance (COP) of the heat pumps was calculated using the following heating and cooling COP expressions:

$$\mathrm{COP}_{heat} = \psi_{heat}\frac{T_{cond}}{T_{cond}-T_{evap}}\ , T_{cond} = 50\ °C\ and\ T_{evap} = T_{out} - 5 \qquad (4.6)$$

$$\mathrm{COP}_{cool} = \psi_{cool}\frac{T_{evap}}{T_{cond}-T_{evap}}\ , T_{cond} = T_{out} + 5\ °\mathrm{C}\ and\ T_{evap} = 0\ °\mathrm{C} \qquad (4.7)$$

Where T_{cond} and T_{evap} are the condenser and evaporation temperatures. The efficiency (ψ) for both heating and cooling was set to 40 % [184]. In addition, a 10 % thermal energy distribution loss was implemented by increasing the heating and cooling demand. Finally, the electric energy consumption by water circulation pumps was set to 10 % of the total heat pump electrical energy consumption [185]. The remaining occupied zones (Atrium, basement, cafeteria block)

used a similar HVAC system to the offices. As expected, this simulation approach results in approximately similar heating, cooling, and ventilation conditions per floor area across the whole building area that has HVAC.

The simulation model included a BIPV system that covered the top of the atrium, the two main building blocks and the adjacent parking lot. The panels use the same nearly south orientation as the building (with a 6º tilt towards East) with an inclination of 33º (defined as the optimal slope for a PV panel at the building location [186]). This study considered a commercially available PV panels [187], with an individual panel area of 1.64 m2 and an efficiency of 19.6 % [187], for the simulation of the PV System. The rows of PV panels were spaced to avoid shading between rows, which resulted in a total of 2175 PV panels. The PV system was modelled considering a DC-to-AC efficiency of 92.5 % and the simulation were performed using the EnergyPlus simulation objects "Generator:Photovoltaic" and "PhotovoltaicPerfomance:EquivalentOne-Diode".

4.2.3.1 Simulation scenarios and performance metrics

This chapter considered four simulation scenarios, two baseline scenarios without flexibility and two scenarios with flexibility based on HVAC (fan coils and AHU, which are the flexible assets available in the building) control:

- BS-22 - A reference scenario with no flexibility and with HVAC cooling setpoint set to 22 ºC, as defined by the building manager.
- BS-24 - Similar to BS-22 but the HVAC cooling setpoint set to 24 ºC.
- CL-24 - Flexibility triggered by cloud shading periods. The AHU was turned off (similar to the event of the measurement campaign) and the fan coil cooling setpoint temperature was raised from 22 ºC to 24 ºC, whenever a cloud shading period identified using the method described in Section 4.2.1.1 occurred. Once the cloud passed the setpoint was reset back to 22 ºC and the AHU was turned back on.
- PV-24 - Flexibility triggered by BIPV production shortages. The AHU was turned off (similar to the event of the measurement campaign) and the fan coil cooling setpoint temperature was raised from 22 ºC to 24 ºC, whenever HVAC energy consumption was higher than BIPV production in the BS-22 model. Once BIPV production was higher

than HVAC energy consumption the setpoint was reset back to 22 ºC and the AHU was turned back on. Additionally, flexibility events are only considered after 10 a.m. to avoid high temperatures when occupants arrive into the building, and BIPV production is reduced.

The two flexibility scenarios were simulated in EnergyPlus by using a one-minute timestep schedule file. Additionally, and in order to ensure that the HVAC systems were not constantly changing its operational status (turning on/off and shifting setpoint temperature), and considering that the system did not predict consumption and production, the following set of rules were defined:

1. A new operational status must persist for a minimum of five minutes, regardless of the conditions (clear/cloudy sky or BIPV surplus/deficit). Therefore, short term on/off actions, which are not effective in HVAC and can even be prejudicial, are avoided.
2. A change of status only occurs after two consecutive minutes with new conditions (clear/cloudy sky or BIPV surplus/deficit). This rule avoids changes with a timespan of one-minute changes (as done in the cloud analysis presented above).

The impact of the BS-24 and the two flexibility scenarios on the energy consumption and grid independence of the building was assessed by comparison with the reference BS-22 scenario. The comparison was based on the total and the HVAC (fan coils plus AHU) electric energy consumptions, the electric grid energy demand and the BIPV energy self-consumption. Two BIPV energy self-consumption ratios were calculated: Total BIPV self-consumption and the BIPV self-consumption for HVAC. The first consisted in the ratio between the total energy consumption and the BIPV production. The second expressed the ratio between the energy consumed by the HVAC system and the BIPV production. In this second ratio, it was assumed that the BIPV production was primarily consumed by the HVAC system (as in PV-24 scenario), since it was the only flexible asset present in the building (the remaining electric energy consumption must be always on).

In addition to these energy performance metrics, thermal comfort and indoor air quality (IAQ) were also analysed. The impact of turning off the AHU on IAQ was evaluated using the indoor CO_2 concentration, by calculating the percentage of time when indoor conditions were outside the four comfort categories of EN 16798-1:2019 [49] (shown in Table 4.3), labelled High, Medium, Moderate and Low for categories I, II, III and IV, respectively. The standard level is

Medium (Category III), and a Low level (category IV) decreases comfort but does not result in health risks [49]. Thermal comfort was evaluated using the number of hours of indoor operative temperature in four different intervals shown in Table 4.3. The building cooling setpoint is defined at an air temperature of 22 ºC by the building manager. The percentage of time, during occupied hours, that indoor temperature was within each range was analysed. The indoor temperature setpoint changes used in the proposed demand response strategy can generate sudden increases in indoor operative temperature (drifts/ramp). The impact of these changes in occupant comfort was evaluated according to ASHRAE Standard 55-2017 [50]. These drifts/ramps were evaluated using the four time spans and temperature changes shown in Table 4.3.

Table 4.3 EN 16798-1:2019 [49] thresholds for CO2 concentration, indoor operative temperature intervals, and ASHRAE Standard 55-2017 [50] thresholds for Drifts/ramps duration and respective operative temperature change.

	EN 16798-1:2019 [49]			ASHRAE Standard 55-2017 [50]	
	Limit of CO_2 concentration above outdoor (ppm)		Ranges of indoor operative temperature (ºC)	Drifts/ramps duration (minutes)	Maximum operative temperature change (ºC)
Cat I	550		21 – 23	15	1.1
Cat II	880		23 – 25	30	1.7
Cat III	1350		25 – 27	60	2.2
Cat IV	1350		27 - 29	120	2.8

4.3 Results and discussion

This section presents the results of this chapter. It begins with a characterization of cloud shading periods (Section 4.3.1). The following section presents the full-scale measurement of the flexibility event in the open plan office space and the calibration of the dynamic thermal simulation model (Section 4.3.2). Finally, section 4.3.3 presents and the whole building simulation focusing on the energy demand flexibility and indoor comfort conditions.

4.3.1 Cloud shading periods

The combination of different cloud shading duration and outdoor temperature has different impacts on building energy demand and flexibility potential. Cloudy periods with high temperatures can result in shorter flexibility events as indoor conditions can quickly become uncomfortable due to façade heating by warm outdoor temperatures and solar gains. Conversely, events in colder days may allow for longer flexibility. The analysis of cloud shading periods (Figure 4.3) in the four US cities resulted in the following climate classifications:

- Cloudy, dominant and constant presence of cloudy days (Boulder).
- Cloudy Cold, cloudy days diminish with increasing maximum daily temperature (Oregon).
- Cloudy Hot, increasing presence of cloudy days with increasing temperature (Oak Ridge).
- Sunny, days with clear sky dominate and cloudy days are constant (Phoenix).

Further, when analysing cloud shading periods, it is important to consider how long the periods last (Figure 4.3 2nd column), when these events occur (Figure 4.3 3rd column) and how many events happen on average per day considering only days with events (Figure 4.3 4th column).

It is observable that most cloud shading periods last up (median value) to 20 minutes in Boulder and Oak Ridge, and approximately 15 minutes in Oregon and Phoenix. The average values are higher, influenced by longer periods which are often outliers. In Boulder and Oak Ridge periods tend to shorten with increasing temperatures, in lower temperatures 25 % of events are longer than 40 minutes while at higher temperature these threshold lowers to 30 minutes. This may benefit building flexibility purposes since discomfort is expected to occur faster during an event with higher temperatures.

Regarding the time of the day most events occur after 12h, although some differences are observable between cities. For building flexibility, events occurring at midday or during the afternoon can be disadvantageous since maximum outdoor temperatures occur during this period of the day. On the other hand, maximum BIPV energy production occurs around 12h, thus the BIPV output when a cloud period is over will be close to its daily maximum, allowing the HVAC system to rebound faster without requiring additional grid demand.

Regarding the average number of events, two trends are observable which seem to be related with the number of days with events. In Boulder and Oak Ridge (in which the ratio of days with events increases with temperature) the number of events per day increase with temperature. On the other hand, in Oregon and Oak Ridge (which have a lower ratio of days with cloud shading events with increasing temperatures), the number of events per days diminishes with temperature.

Lisbon (Figure 4.4) shows similar patterns to the Cloudy Cold climate city of Oregon, with the number of days with shading periods and the number of periods per day decreasing with increasing temperatures. In Lisbon, the majority of cloud event last up to 15 minutes and happen mostly after 15h. However, these results should be analysed with caution, because the number of days considered in Lisbon were reduced due to data availability.

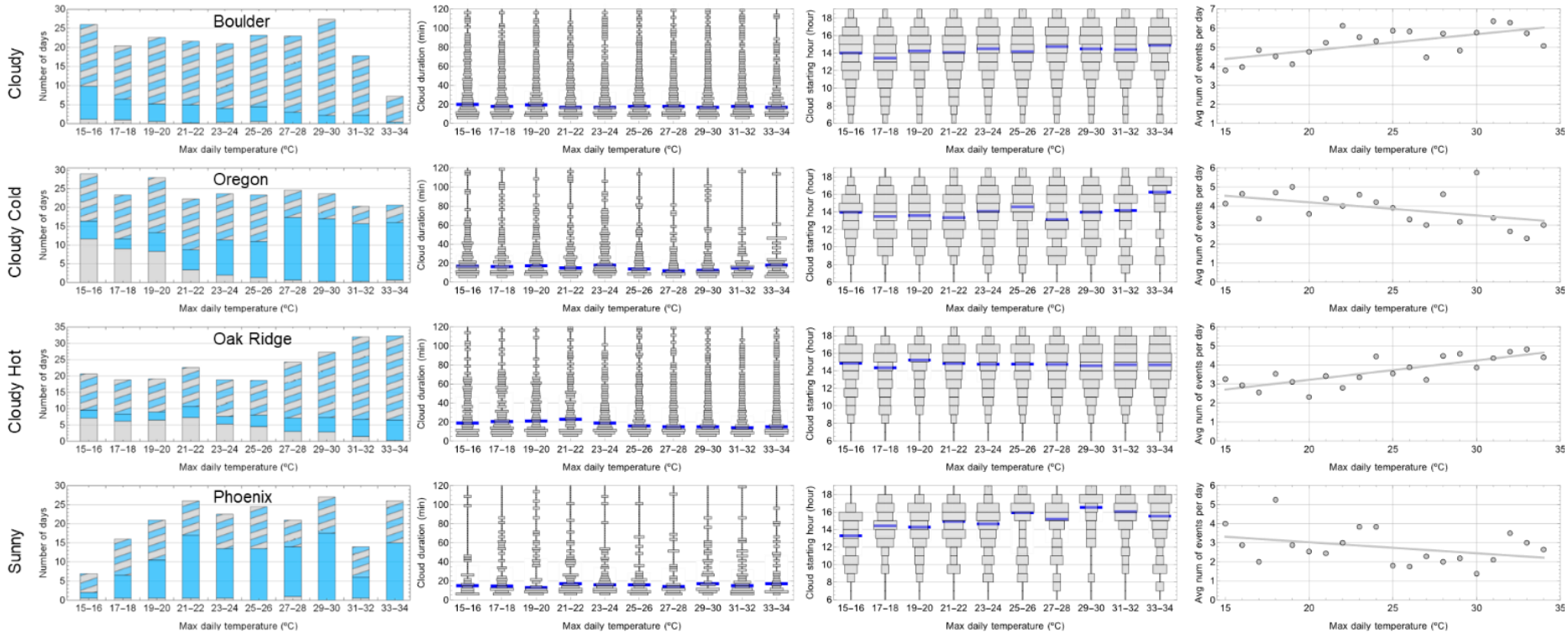

Figure 4.3. Characterization of cloud shading periods in four US cities: 1st column, number of days per year (Cloudy days represented in grey, sunny days in blue, and days with cloudy periods represented in grey and blue stripes); 2nd column, cloud duration (median value in blue); 3rd column, cloud starting hour (median value in blue); 4th column, average number of events per day considering only days with events.

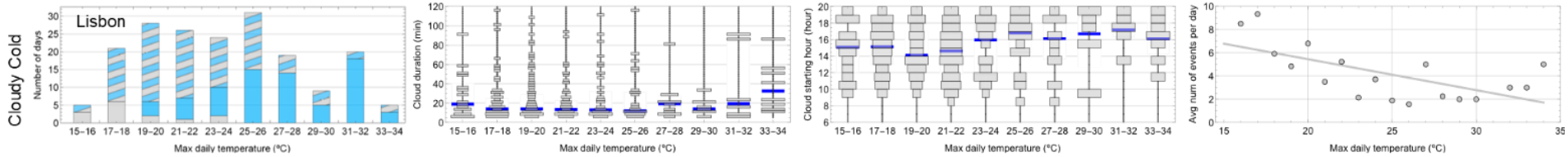

Figure 4.4. Characterization of cloud shading periods in Lisbon. Cloudy days represented in grey, sunny days in blue, and days with cloudy periods represented in grey and blue stripes.

4.3.2 Measurements and calibration of the dynamic thermal simulation model

This section presents the results of the measurements and the calibration of the dynamic simulation model of the open plan office space. During the event the average outdoor air temperature was 13 ºC. The measured equipment electric load and the number of occupants of the open space are shown in

Figure **4.5**. The lighting system was on the whole period with a consumption of 7 W/m^2. The measured outdoor air infiltration was 0.2 space air changes per hour (ACH). To accurately simulate the demand flexibility event, a survey of the objects that contributed to the internal mass of the open space was performed and the results are shown in

Table 4.4. Additionally, this table presents the calculated heat capacitance of the objects. The total heat capacitance equals 5682 kJ/K which, considering the volume of the open space, corresponds to a zone capacitance multiplier of 5.5. This value compares to the upper limit of a lightly furnish office (3 to 5 [180]) and the lower limit of a typical office (6 to 10 [180]), which is the expected range for a modern open space office.

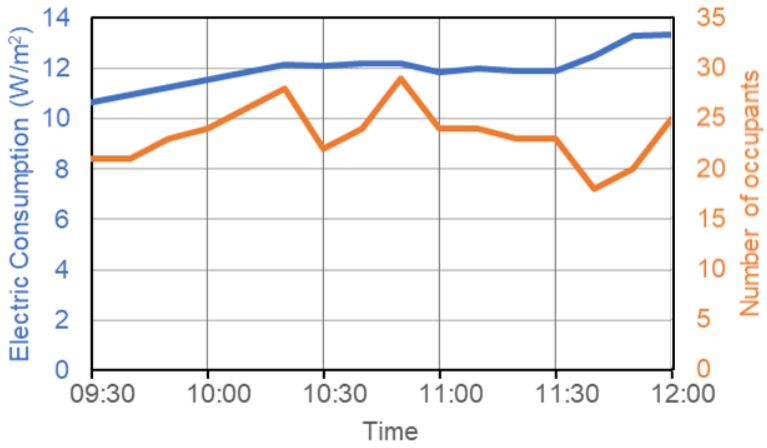

Figure 4.5 Total electrical load and occupation of the open space.

Table 4.4 Capacitance of the Internal mass objects identified during the measurement campaign.

	Cabinet 1.7 m	Cabinet 1.5 m	Cabinet 0.8 m	Cabinet wheels	Desk (Wood)	Desk Separator (Wood)	Paper (5 kg/desk)	Paper (50 % cabinets, Pen. depth 0.01 m)
Number	3	29	10	38	60	30	-	-
Area of exposed surface (m^2)	3.1	2.8	2.3	1.0	2.1	1.04	7.0	74.0
Mass exposed (kg)	148	1276	360	574	2016	499	251	8989
Capacitance (kJ/K)	66	570	161	257	2419	599	352	1259

Figure 4.6 shows the measured and simulated average space air temperature during the demand flexibility event. Additionally, it shows how long air temperature took to increase 1, 2 and 3 ºC. These results confirm that the great majority of cloud periods identified in section 4.3.1 (which last shorter than 60 minutes) have the potential to be used for demand flexibility without spoiling indoor thermal comfort. The results reveal significant differences between the "InternalMass" and "ZoneCapacitanceMultiplier" simulated models. The "ZoneCapacitanceMultiplier" modelling approach has a much better agreement with the measured results compared with the "InternalMass" approach, which overestimates indoor temperature especially during beginning of the event. This difference is related with the method

that each approach uses to model thermal mass, and especially the fact that the "ZoneCapacitanceMultiplier" considers the effective storage capacity in the zone and models it directly into the air. This chapter used the "ZoneCapacitanceMultiplier" model in the whole building simulation described in the next section.

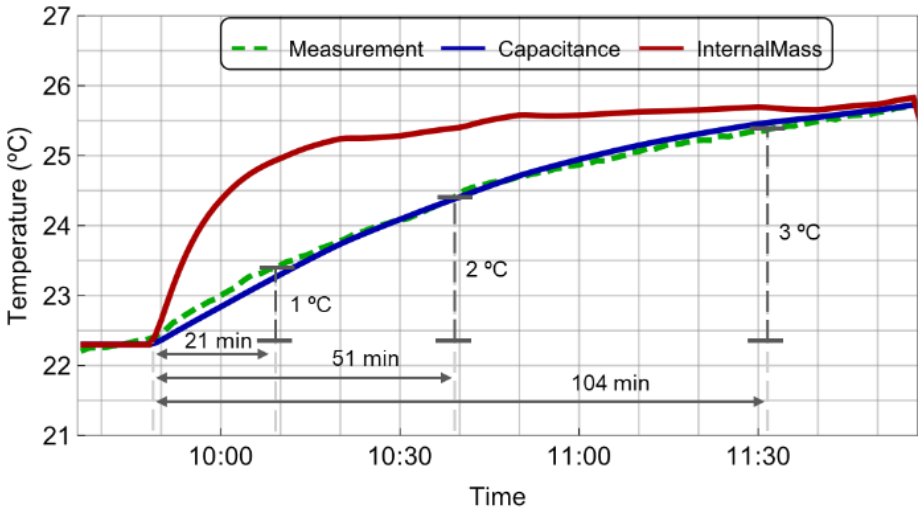

Figure 4.6 Air temperature measured during the demand flexibility event and simulated using the two modelling approaches

4.3.3 Whole building simulation

The next sub-sections present the whole building simulation results of demand flexibility events using the four flexibility scenarios (BS-22, BS-24, CL-24 and PV-24). First, the predicted energy consumption and flexibility results are presented, and proceeds with indoor comfort and IAQ analysis. The whole building model used in this analysis applies the calibrated model of the open space office definitions presented in the previous section to all occupied spaces in the building (89 % of the floor area, garage and auditorium excluded). This simulation used Lisbon weather data from University of Lisbon weather station, and a total of 137 weekdays were considered after excluding weekends and days with missing data.

4.3.3.1 Energy demand flexibility

Figure 4.7 shows the indoor air temperature, electric grid demand and accumulated daily grid demand of the four simulated models, as well as BIPV production by building floor area and changes in fan coil cooling setpoint temperature for CL-24 and PV-24 models.

Table **4.5** shows the results of the total and HVAC electric energy consumption and electric grid energy demand, normalized by building floor area and operation hours (h_o), as well as BIPV self-consumption rates for the four simulated models. The total BIPV production during occupied hours was 425 MWh (21 $Wh/m^2/h_o$). The BS-22 scenario had the highest total and HVAC electric energy consumptions and the highest grid demand, followed by CL-24, BS-24 and PV-24 scenarios. Raising the setpoint temperature to 24 ºC (BS-24 model) decreased total energy consumption by 7 %, HVAC energy consumption by 15 %, total grid demand by 12 % and HVAC grid demand by 19 %.

The two energy flexibility scenarios are active during different percentages of building operation hours: 6 % for CL-24, and 37 % for the PV-24 scenario. This large difference (31 %) in active time is visible in the impact of the two scenarios. CL-24 reduced total energy consumption in 1 % and HVAC consumption in 3 %, while PV-24 reduced in 10 % and 21 %. The reduction in electric grid energy demand, the main objective of the flexibility events, was: 4 % and 23 % for total grid demand; and 6 % and 60 % for the HVAC grid demand, for CL-24 and PV-24. Ideally, PV-24 model would have a grid consumption of 0 when the fan coil setpoint was 22 ºC (Figure 4.7). However, since this is a binary model (on or off) the HVAC cannot be modelled to consume exactly the BIPV production. Consequently, when the HVAC system was turned on after cloudy periods there were peaks in energy consumption to offset the accumulated increased indoor temperatures, resulting in grid demand in moments when in the BS-22 model there was none. Further, the 5 minutes limitation imposed to avoid constant shifts in HVAC operation, also resulted in additional energy consumption.

In terms of BIPV total self-consumption, the BS-22 model consumed 92.6 % of its production, and BS-24 90.0 %. The flexibility models increased BIPV self-consumption, with CL-24 having 92.7 % and PV-24 having 92.9 % of its energy production self-consumed. In contrast, the BIPV self-consumption rate for HVAC increased from BS-22 (76.8 %) to the other three models: 79.9 % (BS-24), 77.5 % (CL-24) and 88.3 % (PV-24). Both demand flexibility models resulted in the reduction of total electric grid energy demand, with CL-24 reducing 4 %

(corresponding to savings of 0.6 Wh/(m2.h_o)) and PV-24 reducing 23 % (corresponding to savings of 3.7 Wh/(m2.h_o)). These savings result from a combination of avoided grid demand and increased BIPV self-consumption.

The PV-24 scenario had lower energy consumptions and higher self-consumption rates than the BS-24 scenario, despite having a lower setpoint (22 ºC) for two thirds of the operation time. These differences are due to an optimized use of BIPV production, and the fact AHU was turned off during flexibility events. Further, these results show relevant potential to reduce electric grid energy demand by using demand flexibility based on HVAC control, either by considering cloud shading periods or by considering the difference between HVAC demand and BIPV consumption.

Figure 4.7 Results of the four demand flexibility scenarios for the 14th and 15th of May: Air temperature in the ground floor of South open space (1st row); fan coil cooling setpoint (2nd row); BIPV production by building floor area (3rd row); Electric grid demand (4th row); and accumulated electric grid demand (5th row). Gray areas corresponds to unoccupied periods.

Table 4.5 Total and HVAC: electric energy demand, electric grid energy demand, and self-consumption for the four simulated models. Total BIPV production: 21 Wh/m^2/h_o.

	Total electric energy consumption (Wh/(m2.ho))	Total electric grid energy demand (Wh/(m2.ho))	HVAC electric energy consumption (Wh/(m2.ho))	HVAC electric grid energy demand (Wh/(m2.ho))	Total BIPV self-consumption (%)	BIPV self-consumption for HVAC (%)
BS-22	36.1	15.9	16.8	3.9	92.6 %	76.8 %
BS-24	33.6 (-7 %)	14.0 (-12 %)	14.2 (-15 %)	2.9 (-26 %)	90.0 %	79.9 %
CL-24	35.6 (-1 %)	15.4 (-4 %)	16.2 (-3 %)	3.7(-6 %)	92.7 %	77.5 %
PV-24	32.5 (-10 %)	12.3 (-23 %)	13.2 (-21 %)	1.5 (-60 %)	92.9 %	88.3 %

4.3.3.2 Indoor comfort conditions

BaB based demand flexibility events rely on changes in thermal mass temperature and, consequently, room air temperature. In this context there is a need to assess indoor thermal comfort and IAQ during and after flexibility events. For this purpose, Table 4.6 shows the results of the predicted indoor operative temperature and CO_2 levels during occupied periods for the four flexibility scenarios. It should be noted that the cooling system of the building triggers according to the indoor air temperature and Table 6 results were calculated using the indoor operative temperature. Since operative temperature depends on both air temperature and radiant temperature (from walls, windows, etc.), values higher than the cooling setpoint (24 ºC) can be reached.

The operative temperature range analysis shows that, as expected, the BS-22 model and CL-24 had the highest percentage of time on the first temperature range (21-23 ºC). The flexibility events of PV-24 resulted in higher operative temperatures compared with BS-22, although only 5 % of the time is between 25-27 ºC. On the other hand, the raised cooling setpoint of the BS-24 model resulted in 37 % of the time in the 25-27 ºC operative temperature range. Additionally, the drifts and ramps were evaluated according to ASHRAE Standard 55-2017 [50]. No drifts and ramps that could result in discomfort occurred, except for one time in the atrium of PV-24 simulation. The absence of drifts and ramps is explained by the building characteristic (the measurement campaign did not result in discomfort either) and the limitation to a maximum indoor temperature of 24 ºC.

The analysis of indoor CO_2 concentration used the four categories in EN 16798-1:2019 [49]. The results shown that the BS-22 and BS-24 models were always below the limits of category I (a direct consequence of the AHU being on during all operation hours). The CL-24 model was

above category I for 8 % of the time and category II for 2 %, while PV-24 was above category I for 41 % of the time and above category II for 17 %. These values are not dangerous for the occupants and can be reduced by either incorporating natural ventilation or by scheduling the AHU to be turned on after a defined period of elevated indoor CO_2.

The results show that the two simulations with HVAC flexibility controls reduced the grid energy demand and increased self-consumption while maintaining indoor conditions comfortable to the occupants, especially the PV-24 scenario. Further, larger reductions could be obtained by raising the cooling setpoint more than 2 ºC, although high indoor temperatures and temperature ramps may arise and generate discomfort. In addition, the increase in the cooling setpoint may result in lower self-consumption rates, as demonstrated by the BS-24 scenario.

Table 4.6 Percentage of time out of limits for the four comfort categories of indoor operative temperature and CO_2 concentration.

	% Time in each indoor operative temperature range (ºC)				% Time CO2 concentration above outdoor (ppm)		
	21 - 23	23 - 25	25 - 27	27 - 29	Cat I (550)	Cat II (880)	Cat III & IV (1350)
BS-22	43 %	55 %	1 %	0 %	0 %	0 %	0 %
BS-24	7 %	56 %	37 %	0 %	0 %	0 %	0 %
CL-24	40 %	58 %	1 %	0 %	8 %	2 %	0 %
PV-24	26 %	68 %	5 %	0 %	41 %	17 %	0 %

4.4 Conclusions

This chapter analysed the effectiveness of using building thermal mass energy storage to offset temporary reductions in BIPV output due to passing clouds in cooling dominated office buildings. The chapter was divided in two parts. The first part characterized shading periods caused by passing clouds that may trigger HVAC flexibility events (minimum shading period of 5 minutes). This analysis identified four cloud regimes: cloudy, cloudy cold, cloudy hot, sunny. These regimes are defined by the number of days with cloud shading events that occur in different intervals of maximum daytime temperature. Independently of the cloud regime,

more than half of the identified shading periods last less than 20 minutes and occur during the afternoon.

The second part of the chapter analysed the effectiveness of turning off the HVAC system to offset temporary reductions in BIPV output due to passing clouds. Once the HVAC is turned off, the internal building thermal mass operates as a low-cost thermal energy storage system that limits indoor temperature increase during the energy demand flexibility event that occurs during the period of shading by the passing cloud. The analysis began with a measurement of the indoor temperature variation in an open plan office space where the HVAC system was tuned off for 128 minutes. The results show that after turning the HVAC off, the average indoor temperature took 21 min to increase 1 ºC, 51 minutes to 2 ºC, and 104 minutes to 3 ºC. These response times were longer than the majority of the clouds identified in the first part of this chapter (20 minutes), revealing that internal mass may be able to limit temperature increase during HVAC off events triggered by passing clouds.

The results of the measurement campaign were then used to calibrate a dynamic simulation model of the building. The calibrated model was used to simulate demand flexibility events triggered by passing clouds using two different strategies. In the first, CL-24, the flexibility events were triggered by the clouds identified in the first part of this chapter, occurring in 6 % of building operation hours. In the second scenario, PV-24, HVAC off flexibility events occur when BIPV production is lower than HVAC consumption (a condition that occurs in 37 % of the building operation hours). The simulation results show that both strategies were able to reduce grid energy demand while increasing BIPV self-consumption and maintaining comfortable indoor conditions. The PV-24 scenario performs better than the CL-24 scenario, achieving a 60 % reduction in grid energy demand.

Exploring demand flexibility together with weather variability (cloud shading) presents promising results and further researched is needed. The analysis of cloud shading regimes should be extended to multiple locations in the world to map the potential of cloud shading demand flexibility events and possibly identify other cloud regimes. In this building other strategies could be used to enhance energy efficiency without compromising occupants' comfort. In particular, the use of natural ventilation and night cooling could be used to reduce the HVAC energy consumption during the flexibility events or be used to cool down the building during night-time reducing the cooling demand in the following day [188,189]. Further, it would be interesting to simulate an AHU with frequency control to optimize BIPV self-consumption, as

well as test the effect of turning the AHU on when the temperature limits are reached instead of turning on the HVAC systems, especially when outdoor temperature is lower than indoors. Finally, further experimental studies should be performed, and occupant's feedback should be collected during these campaigns.

Chapter 5 – General conclusions

Understating climate change and its impacts is fundamental for accurate design and simulation of buildings. Future buildings will rely on three pillars that, sometimes, can be opposites: be climate resilient, use passive building strategies, and use local energy resources. These three pillars share a common need for high-resolution weather and climate data for accurate BES. This thesis developed on these pillars and used weather observations and state-of-the-art climate data from both historical and future simulations. First, future climate data files for BES were compared, secondly the impacts of climate change on passive building strategies were analysed, and finally the use of building thermal mass to offset BIPV production reductions caused by passing clouds was assessed.

Chapter 2 presented a comparative study of two methods to produce future climate hourly data data files for BES: Morphing and typical meteorological year of future climate (F-TMY). The assessment used as reference high-resolution RCM climate simulations of Iberia (historical and future hourly data for 1990-1999 and 2090-2099). This multi-year data was used as a reference to compare anomalies in air temperature, and the impact in BES predictions of annual and peak HVAC energy consumptions in four buildings. Additionally, this study performed a sensitivity analysis of morphing method. The analysis showed that BES inter-annual variability is similar in historical and future datasets. Thus, using multiple years of future hourly data outputted by RCM increase computational and time demand while failing to provide a significant advantage compared to a TMY analysis. A high-quality Morphed TMY weather file has a similar performance compared to F-TMY (average difference: 8 % versus 7 %), thus Morphing seems to be a good simplified solution for BES of future climate. However, Morphing based on different baseline climates, coarse grid resolution and/or outdated climate projections leads to BES average differences of 16 %-20 %, making these data files unsuitable for BES.

Chapter 3 presented an analysis of climate change effects on end-of-century air temperature, wind and solar radiation and its impacts on passive building strategies, focused on the EU 43 most populated cities. The analysis focused on the shift and reshape of annual and diurnal temperature cycles, particularly on when, where, and how passive design strategies (NV, night cooling, and solar shading) are affected, going beyond season or yearly effectiveness. The results showed that changes in the diurnal temperature cycle will affect the DTR, leading to two diurnal temperature cycle shapes: daytime (DTR increase) and a nighttime (DTR decrease), with different impacts on the heating and cooling seasons. This study identified that mild and warm days will occur earlier and persist until later in the year, shifting NV and shading seasons.

In all Europe, except in Scandinavia and the British Isles, the effectiveness of passive design strategies will be reduced. In Northern Europe, NV season will be 6 weeks longer, while in Southern Europe it will be 9 weeks shorter. In Southern Europe, shading season will increase 2.5 months, direct solar radiation in south façades will increase 35 % consequence of -13.5° in average maximum solar altitude, making overhangs less effective.

Chapter 4 presented an analysis of the effectiveness of demand flexibility, particularly HVAC system turn off, to offset temporary reductions in BIPV output due to passing clouds in a cooling dominated office building. Additionally, this chapter characterized shading periods caused by passing clouds that could trigger demand flexibility events (5 minutes minimum period). This characterization identified four cloud regimes (cloudy, cloudy cold, cloudy hot, sunny), and showed that more than half of clouds last less than 20 minutes and occur predominately in the afternoon, independently of the climate. Measurements performed in an occupied open plan office space showed that after turning the HVAC off, the building thermal mass limited indoor temperature increase to 2 ºC in the first 50 minutes. Finally, simulation analysis of HVAC control-based energy flexibility showed that it is possible to maintain acceptable thermal comfort while reducing grid energy demand by 60 % during the cooling season.

In the coming decades, the impacts of climate change on building energy consumption will be more prevalent and require further research. The results presented in this thesis have shown the importance of using high-resolution data for building energy studies. Further, future climate change studies should focus on shorter time scales, for example intra-daily changes, going beyond the seasonal and yearly effects. This topic can be further developed in the future, in particularly when the next generation of climate model simulation becomes available. These models will allow a better understanding of the long-term changes but will also provide the opportunity to have a deeper insight on the shorter timescales. The design of passive building strategies should be built on top of these new models, to ensure that strategies remain efficient in the decades to come. Finally, exploring demand flexibility together with weather variability (e.g. cloud shading) presents promising results, and further researched is needed for both present and future climates.

Chapter 6 - Bibliography

[1] IPCC, 2014: Climate Change 2014: Synthesis Report. Contribution of Working Groups I, II and III to the Fifth Assessment Report of the Intergovernmental Panel on Climate Change [Core Writing Team, R.K. Pachauri and L.A. Meyer (eds.)]. IPCC, Geneva, Switzerland, 151 pp. ISBN:978-92-9169-143-2

[2] World Meteorological Organization (2021). State of the global climate in 2020. WMO-No. 1264, 56 pp, ISBN 978-92-63-11264-4.

[3] Della-Marta, P. M., Haylock, M. R., Luterbacher, J., & Wanner, H. (2007). Doubled length of western European summer heat waves since 1880. Journal of Geophysical Research, 112(D15). doi:10.1029/2007jd008510

[4] Rogelj, J., Meinshausen, M., & Knutti, R. (2012). Global warming under old and new scenarios using IPCC climate sensitivity range estimates. Nature Climate Change, 2(4), 248–253. doi:10.1038/nclimate1385

[5] Russo, S., Dosio, A., Graversen, R. G., Sillmann, J., Carrao, H., Dunbar, M. B., Singleton, A., Montagna, P., Barbola, P., & Vogt, J. V. (2014), Magnitude of extreme heat waves in present climate and their projection in a warming world, J. Geophys. Res. Atmos., 119, 12,500– 12,512. doi:10.1002/2014JD022098.

[6] Dwyer, J.G., Biasutti, M., & Sobel, A.H. (2012). Projected Changes in the Seasonal Cycle of Surface Temperature. J. Climate, 25, 6359–6374. https://doi.org/10.1175/JCLI-D-11-00741.1

[7] Wang, G., & Dillon, M. (2014) Recent geographic convergence in diurnal and annual temperature cycling flattens global thermal profiles. Nature Clim Change 4, 988–992. doi:10.1038/nclimate2378

[8] Krayenhoff, E.S., Moustaoui, M., Broadbent, A.M., Gupta, V., & Georgescu, M. (2018). Diurnal interaction between urban expansion, climate change and adaptation in US cities. Nature Clim Change 8, 1097–1103. doi:10.1038/s41558-018-0320-9

[9] Cassou, C., & Cattiaux, J. (2016). Disruption of the European climate seasonal clock in a warming world. Nature Clim Change 6, 589–594. doi:10.1038/nclimate2969

[10] Harrington, L. J., Frame, D. J., Hawkins, E., & Joshi, M. (2017). Seasonal cycles enhance disparities between low-and high-income countries in exposure to monthly temperature emergence with future warming. Environmental Research Letters, 12(11), 114039. https://doi.org/10.1088/1748-9326/aa95ae

[11] Santamouris, M. (2020). Recent progress on urban overheating and heat island research. Integrated assessment of the energy, environmental, vulnerability and health impact. Synergies with the global climate change. Energy and Buildings, 207, 109482. https://doi.org/10.1016/j.enbuild.2019.109482

[12] Argüeso, D., Evans, J.P., Fita, L., & Bormann, K.J. (2014). Temperature response to future urbanization and climate change. Climate Dynamics 42, no. 7-8 (2014): 2183-2199. https://doi.org/10.1007/s00382-013-1789-6

[13] Dimoudi, A., & Tompa, C. (2008). Energy and environmental indicators related to construction of office buildings. Resources, Conservation and Recycling, 53(1-2), 86–95. doi:10.1016/j.resconrec.2008.09.008

[14] Mendler, S. (2008). Buildings: an essential sector in climate change mitigation. Growing the economy through global warming solutions, Civil Society Institution, 2008.

[15] Li, B., & Yao, R. (2012). Building energy efficiency for sustainable development in China: challenges and opportunities. Building Research & Information, 40(4), 417–431. doi:10.1080/09613218.2012.682419

[16] International Energy Agency (2008). Energy Efficiency Requirements in Building Codes – Energy Efficiency Policies for New Buildings, 2008.
[17] Pérez-Lombard, L., Ortiz, J., & Pout, C. (2008). A review on buildings energy consumption information. Energy and Buildings, 40(3), 394–398. doi:10.1016/j.enbuild.2007.03.007
[18] U.S. Department of Energy (2011). Buildings Energy Data Book, Department of Energy, U.S. Department of Energy, Washington DC, 2011.
[19] Yau, Y. H., & Hasbi, S. (2013). A review of climate change impacts on commercial buildings and their technical services in the tropics. Renewable and Sustainable Energy Reviews, 18, 430–441. doi:10.1016/j.rser.2012.10.035
[20] De Wilde, P., & Coley, D. (2012). The implications of a changing climate for buildings. Building and Environment, 55, 1–7. doi:10.1016/j.buildenv.2012.03.014
[21] Ürge-Vorsatz, D., Cabeza, L.F., Serrano, S., Barreneche, S., & Petrichenko, K. (2015). Heating and cooling energy trends and drivers in buildings. Renewable and Sustainable Energy Reviews, 41, 85-98, ISSN 1364-0321, https://doi.org/10.1016/j.rser.2014.08.039.
[22] Roshan, G., Oji, R., & Attia, S. (2019). Projecting the impact of climate change on design recommendations for residential buildings in Iran. Building and Environment, 155, 283-297. https://doi.org/10.1016/j.buildenv.2019.03.053
[23] Jensen, P. A., Maslesa, E., Berg, J. B., & Thuesen, C. (2018). 10 questions concerning sustainable building renovation. Building and Environment, 143, 130-137. https://doi.org/10.1016/j.buildenv.2018.06.051
[24] Garde, F., Lenoir, A., Scognamiglio, A., Aelenei, D., Waldren, D., Rostvik, H. N., Ayoub, J., Aelenei, L., Donn, M., Tardif, M., & Cory, S. (2014). Design of net zero energy buildings: feedback from international projects. Energy Procedia, 61, 995-998. https://doi.org/10.1016/j.egypro.2014.11.1011
[25] Costanzo, V., Fabbri, K., & Piraccini, S. (2018). Stressing the passive behavior of a Passivhaus: an evidence-based scenario analysis for a Mediterranean case study. Building and Environment, 142, 265-277. https://doi.org/10.1016/j.buildenv.2018.06.035
[26] Attia, S., Eleftheriou, P., Xeni, F., Morlot, R., Ménézo, C., Kostopoulos, V., Betsi, M., Kalaitzoglou, I., Pagliano, L., Cellura, M., Almeida, M., Ferreira, M., Baracu, T., Badescu, V., Crutescu, R., & Hidalgo-Betanzos, J.M. (2017). Overview and future challenges of nearly zero energy buildings (nZEB) design in Southern Europe. Energy and Buildings, 155, 439-458. https://doi.org/10.1016/j.enbuild.2017.09.043
[27] DeKay, M., & Brown, G. Z. (2013). Sun, wind, and light: Architectural design strategies. John Wiley & Sons. ISBN: 978-0-470-94578-0
[28] Bouchama, A., & Knochel, J.P. (2002). Heat stroke, New England Journal of Medicine, 346, , pp. 1978–1988, doi:10.1056/NEJMra011089.
[29] Robine, J.-M., Cheung, S. L. K., Le Roy, S., Van Oyen, H., Griffiths, C., Michel, J.-P., & Herrmann, F. R. (2008). Death toll exceeded 70,000 in Europe during the summer of 2003. Comptes Rendus Biologies, 331(2), 171–178. doi:10.1016/j.crvi.2007.12.001
[30] Li, D. H., Yang, L., & Lam, J. C. (2012). Impact of climate change on energy use in the built environment in different climate zones–a review. Energy, 42(1), 103-112. https://doi.org/10.1016/j.energy.2012.03.044
[31] Andrić, I., Le Corre, O., Lacarrière, B., Ferrão, P., & Al-Ghamdi, S. G. (2019). Initial approximation of the implications for architecture due to climate change. Advances in Building Energy Research, 1-31. https://doi.org/10.1080/17512549.2018.1562980

[32] Goetzler, W., Guernsey, M., Young, J., Fujrman, J., & Abdelaziz, A. (2016). The future of air conditioning for buildings (No. DOE/EE-1394). Navigant Consulting, Burlington, MA (United States). https://doi.org/10.2172/1420235
[33] ASHRAE. (2015). ASHRE Handbook - HVAC applications (SI). Atlanta, USA. ISSN 1078-6082
[34] Daly, D., Cooper, P., & Ma, Z. (2014). Implications of global warming for commercial building retrofitting in Australian cities. Building and Environment, 74, 86-95. https://doi.org/10.1016/j.buildenv.2014.01.008
[35] Herrera, M., Natarajan, S., Coley, D. A., Kershaw, T., Ramallo-González, A. P., Eames, M., Fosas, D., Wood, M. (2017). A review of current and future weather data for building simulation. Building Services Engineering Research and Technology, 38(5), 602–627. doi:10.1177/0143624417705937
[36] Hall, I. J., Prairie, R. R., Anderson, H. E., & Boes, E. C. (1978). Generation of a typical meteorological year, In: Proceedings of the 1978 annual meeting of the American Section of the International Solar Energy Society, 1978, 669-71.
[37] Kershaw, T., Eames, M., & Coley, D. (2010). Comparison of multi-year and reference year building simulations. Building Services Engineering Research and Technology, 31(4), 357-369. https://doi.org/10.1177/0143624410374689
[38] Crawley, D. B., & Lawrie, L. K. (2015, December). Rethinking the TMY: is the 'typical'meteorological year best for building performance simulation?. In Conference: Building Simulation.
[39] Rastogi, P., & Andersen, M. (2016). Incorporating Climate Change Predictions in the Analysis of Weather-Based Uncertainty. Proceedings of SimBuild, 6(1).
[40] Georgiou, G., Efterkhari, M., Eames, P., & Mourshed, M. (2013). A Study of the Effects of Weighting Indices for the Development of TMY Used for Building Simulation. Proceedings of BS, 922-929.
[41] Narowski, P., Janicki, M., & Heim, D. (2013, August). Comparison of Untypical Meteorological Years (UMY) and their influence on building energy performance simulations. In Proc. of Conference "Building Simulation–BS2013", Le Bourget-du-Lac (pp. 1414-1421).
[42] Yang, L., Lam, J. C., Liu, J., & Tsang, C. L. (2008). Building energy simulation using multi-years and typical meteorological years in different climates. Energy Conversion and Management, 49(1), 113-124. https://doi.org/10.1016/j.enconman.2007.05.004
[43] Notton, G., Nivet, M. L., Voyant, C., Paoli, C., Darras, C., Motte, F., & Fouilloy, A. (2018). Intermittent and stochastic character of renewable energy sources: Consequences, cost of intermittence and benefit of forecasting. Renewable and sustainable energy reviews, 87, 96-105. https://doi.org/10.1016/j.rser.2018.02.007
[44] Bendato, I., Bonfiglio, A., Brignone, M., Delfino, F., Pampararo, F., Procopio, R., & Rossi, M. (2018). Design criteria for the optimal sizing of integrated photovoltaic-storage systems. Energy, 149, 505-515. https://doi.org/10.1016/j.energy.2018.02.056
[45] Jensen, S. Ø., Marszal-Pomianowska, A., Lollini, R., Pasut, W., Knotzer, A., Engelmann, P., Stafford, A., & Reynders, G. (2017). IEA EBC annex 67 energy flexible buildings. Energy and Buildings, 155, 25-34. https://doi.org/10.1016/j.enbuild.2017.08.044
[46] Ooka, R., & Ikeda, S. (2015). A review on optimization techniques for active thermal energy storage control. Energy and Buildings, 106, 225-233. https://doi.org/10.1016/j.enbuild.2015.07.031
[47] Hedegaard, K., Mathiesen, B. V., Lund, H., & Heiselberg, P. (2012). Wind power integration using individual heat pumps–analysis of different heat storage options. Energy, 47(1), 284-293. https://doi.org/10.1016/j.energy.2012.09.030

[48] Reynders, G. N. T. S. D., Nuytten, T., & Saelens, D. (2013). Potential of structural thermal mass for demand-side management in dwellings. Building and Environment, 64, 187-199. https://doi.org/10.1016/j.buildenv.2013.03.010
[49] EN, CEN Standard. (2019). 16798-1. Energy Performance of Buildings—Ventilation for Buildings—Part 1: Indoor Environmental Input Parameters for Design and Assessment of Energy Performance of Buildings Addressing Indoor Air Quality. Thermal Environment, Lighting and Acoustics—Module M1-6
[50] ASHRAE Standard 55-2017: Thermal Environmental Conditions for Human Occupancy. ASHRAE standard, ISSN 1041-2336.
[51] Péan, T. Q., Salom, J., & Costa-Castelló, R. (2019). Review of control strategies for improving the energy flexibility provided by heat pump systems in buildings. Journal of Process Control, 74, 35-49. https://doi.org/10.1016/j.jprocont.2018.03.006
[52] Hurtado, L. A., Rhodes, J. D., Nguyen, P. H., Kamphuis, I. G., & Webber, M. E. (2017). Quantifying demand flexibility based on structural thermal storage and comfort management of non-residential buildings: A comparison between hot and cold climate zones. Applied energy, 195, 1047-1054. https://doi.org/10.1016/j.apenergy.2017.03.004
[53] Schermeyer, H., Vergara, C., & Fichtner, W. (2018). Renewable energy curtailment: A case study on today's and tomorrow's congestion management. Energy Policy, 112, 427-436. https://doi.org/10.1016/j.enpol.2017.10.037
[54] Schibuola, L., Scarpa, M., & Tambani, C. (2015). Demand response management by means of heat pumps controlled via real time pricing. Energy and Buildings, 90, 15-28. https://doi.org/10.1016/j.enbuild.2014.12.047
[55] Belcher, S., Hacker, J., & Powell, D. (2005). Constructing design weather data for future climates. Building Services Engineering Research and Technology, 26(1), 49–61. doi:10.1191/0143624405bt112oa
[56] Jentsch, M. F., James, P. A. B., Bourikas, L., Bahaj, A. S., Transforming existing weather data for worldwide location to enable energy and building performance simulation under future climates, Renewable Energy, 55, 2013, 514-24. https://doi.org/10.1016/j.renene.2012.12.049
[57] EnergyPlus (2019). EnergyPlus Weather Data. https://energyplus.net/weather [accessed 01/04/2019]
[58] Marion, W., & Urban, K. (1995). User`s manual for TMY2s: Derived from the 1961--1990 National Solar Radiation Data Base. doi:10.2172/87130
[59] ASHRAE, International weather for energy calculations (IWEC Weather Files) User's Manual, Version 1.1, 2012.
[60] Wilcox, S., & Marion, W. (2008). Users Manual for TMY3 Data Sets (Revised). doi:10.2172/928611.
[61] Climate One Building (2019). Climate One Building: Repository of free climate data for building performance simulation. http://climate.onebuilding.org/ [accessed 01/04/2019].
[62] Taylor, K. E., Stouffer, R. J., & Meehl, G. A. (2012). An Overview of CMIP5 and the Experiment Design. Bulletin of the American Meteorological Society, 93(4), 485–498. doi:10.1175/bams-d-11-00094.1
[63] Van Vuuren, D. P., Edmonds, J., Kainuma, M., Riahi, K., Thomson, A., Hibbard, K., Hurtt, G.C., Kram, T., Krey, V., Lamarque, J.F., Masui, T., Meinshausen, M., Nakicenovic, N., Smith, S.J., & Rose, S. K. (2011). The representative concentration pathways: an overview. Climatic Change, 109(1-2), 5–31. doi:10.1007/s10584-011-0148-z

[64] Roberge, F., & Sushama, L. (2018). Urban heat island in current and future climates for the island of Montreal. Sustainable Cities and Society, 40, 501–512. doi:10.1016/j.scs.2018.04.033
[65] Rodrigues, L. T., Gillott, M., & Tetlow, D. (2013). Summer overheating potential in a low-energy steel frame house in future climate scenarios. Sustainable Cities and Society, 7, 1–15. doi:10.1016/j.scs.2012.03.004
[66] Soares, P. M. M., Cardoso, R. M., Lima, D. C. A., & Miranda, P. M. A. (2017). Future precipitation in Portugal: high-resolution projections using WRF model and EURO-CORDEX multi-model ensembles. Climate Dynamics, 49(7-8), 2503–2530. doi:10.1007/s00382-016-3455-2
[67] Kikumoto, H., Ooka, R., Arima, Y., & Yamanaka, T. (2015). Study on the future weather data considering the global and local climate change for building energy simulation. Sustainable Cities and Society, 14, 404–413. doi:10.1016/j.scs.2014.08.007
[68] Lindberg, F., Thorsson, S., Rayner, D., & Lau, K. (2016). The impact of urban planning strategies on heat stress in a climate-change perspective. Sustainable Cities and Society, 25, 1–12. doi:10.1016/j.scs.2016.04.004
[69] Katragkou, E., García-Díez, M., Vautard, R., Sobolowski, S., Zanis, P., Alexandri, G., Cardoso, R.M., Colette, A., Fernández, J., Goblet, A., Georgen, K., Karacostas, T., Knist, S., Mayer, S., Soares, P.M.M., Pytharoulis, I, Tegoulias, I., Tsikerdekis, A., & Jacob, D. (2014). Hindcast regional climate simulations within EURO-CORDEX: evaluation of a WRF multi-physics ensemble. Geoscientific Model Development Discussions, 7(5), 6629–6675. doi:10.5194/gmdd-7-6629-2014
[70] Wang, H., & Chen, Q. (2014). Impact of climate change heating and cooling energy use in buildings in the United States. Energy and Buildings, 82, 428–436. doi:10.1016/j.enbuild.2014.07.034
[71] Jentsch, M. F., Bahaj, A. S., & James, P. A. B. (2008). Climate change future proofing of buildings—Generation and assessment of building simulation weather files. Energy and Buildings, 40(12), 2148–2168. doi:10.1016/j.enbuild.2008.06.005
[72] Kolokotroni, M., Ren, X., Davies, M., & Mavrogianni, A. (2012). London's urban heat island: Impact on current and future energy consumption in office buildings. Energy and buildings, 47, 2012, 302-311. doi:10.1016/j.enbuild.2011.12.019
[73] Gilles, F., Bernard, S., Ioannis, A., & Simon, R. (2017). Decision-making based on network visualization applied to building life cycle optimization. Sustainable Cities and Society, 35, 565–573. doi:10.1016/j.scs.2017.09.006
[74] IPCC, 2007: Climate Change 2007 The physical science basis. Contribution of working group I to the Fourth Assessment Report of the Intergovernmental Panel on Climate Change. Cambridge, UK and New York, NY, Usa: Cambridge Press, 996
[75] Robert, A., & Kummert, M. (2012). Designing net-zero energy buildings for the future climate, not for the past. Building and Environment, 55, 150–158. doi:10.1016/j.buildenv.2011.12.014
[76] Cox, R. A., Drews, M., Rode, C., & Nielsen, S. B. (2015). Simple future weather files for estimating heating and cooling demand. Building and Environment, 83, 104–114. doi:10.1016/j.buildenv.2014.04.006
[77] Rastogi, P., On the sensitivity of buildings to climate: the interaction of weather and building envelopes in determining future building energy consumption, Doctoral dissertation, École Polytechnique Féderale de Lausanne, 2016.
[78] Nik, V. M. (2016). Making energy simulation easier for future climate – Synthesizing typical and extreme weather data sets out of regional climate models (RCMs). Applied Energy, 177, 204–226. doi:10.1016/j.apenergy.2016.05.107

[79] Soares, P. M. M., Cardoso, R. M., Miranda, P. M. A., de Medeiros, J., Belo-Pereira, M., & Espirito-Santo, F. (2012). WRF high resolution dynamical downscaling of ERA-Interim for Portugal. Climate Dynamics, 39(9-10), 2497–2522. doi:10.1007/s00382-012-1315-2
[80] Mauree, D., Coccolo, S., Perera, A., Nik, V., Scartezzini, J. L., & Naboni, E. (2018). A new framework to evaluate urban design using urban microclimatic modeling in future climatic conditions. Sustainability, 10(4), 1134. https://doi.org/10.3390/su10041134
[81] Eames, M., Kershaw, T., & Coley, D. (2012). The appropriate spatial resolution of future weather files for building simulation. Journal of Building Performance Simulation, 5(6), 347–358. doi:10.1080/19401493.2011.608133
[82] Nik, V. M., Sasic Kalagasidis, A., & Kjellström, E. (2012). Statistical methods for assessing and analysing the building performance in respect to the future climate. Building and Environment, 53, 107–118. doi:10.1016/j.buildenv.2012.01.015
[83] Moazami, A., Nik, V. M., Carlucci, S., & Geving, S. (2019). Impacts of future weather data typology on building energy performance–Investigating long-term patterns of climate change and extreme weather conditions. Applied Energy, 238, 696-720. doi:10.1016/j.apenergy.2019.01.085.
[84] Cardoso, R. M., Soares, P. M. M., Miranda, P. M. A., & Belo-Pereira, M. (2012). WRF high resolution simulation of Iberian mean and extreme precipitation climate. International Journal of Climatology, 33(11), 2591–2608. doi:10.1002/joc.3616
[85] Giorgi, F., & Lionello, P. (2008). Climate change projections for the Mediterranean region. Global and Planetary Change, 63(2-3), 90–104. doi:10.1016/j.gloplacha.2007.09.005
[86] Eurostat. Population on 1 January by five year age group, sex metropolitan regions [met_pjangrp3]. Retrieved March 27, 2017, from http://ec.europa.eu/eurostat/web/products-datasets/-/met_pjangrp3
[87] Skamarock, W. C., Klemp, J. B., Dudhia, J., Gill, D. O., Barker, D., Duda, M. G., Huang, X., Wang, W., & Powers, J. G. (2008). A Description of the Advanced Research WRF Version 3. NCAR Technical Note NCAR/TN-475+STR, doi:10.5065/D68S4MVH.
[88] Soares, P. M. M., Lima, D. C. A., Cardoso, R. M., & Semedo, A. (2016). High resolution projections for the western Iberian coastal low level jet in a changing climate. Climate Dynamics, 49(5-6), 1547–1566. doi:10.1007/s00382-016-3397-8
[89] Hazeleger, W., Severijns, C., Semmler, T., Ştefănescu, S., Yang, S., Wang, X., Wyser, K., Dutra, E., Baldasano, J.M., Bintanja, R., Bougeault, P., Caballero, R., Ekman, A.M.L., Christensen, J.H., van den Hurk, B., Jimenez, P., Jones, C., Kållberg, P., Koenigk, T., McGrath, R., Miranda, P., van Noije, t., Palmer, T., Parodi, J.A., Schmith, T., Selten, F., Storelvmo, t., Sterl, A., Tapamo, H., Vancoppenolle, M., Viterbo, P., & Willén, U. (2010). EC-Earth. Bulletin of the American Meteorological Society, 91(10), 1357–1364. doi:10.1175/2010bams2877.1
[90] Hong S-Y, & Lim J-OJ (2006). The WRF single-moment 6-class microphysics scheme (WSM6). J Korean Meteorol Soc 42:129–151
[91] Janjic, Z.I. (2001). Nonsingular implementation of the Mellor–Yamada level 2.5 scheme in the NCEP Meso Model. NCEP Office Note 437, 61 pp
[92] Betts, A.K. (1986). A new convective adjustment scheme. Part I: Observational and theoretical basis. Quart J Roy Meteor Soc 112:677-691. https://doi.org/10.1002/qj.49711247307
[93] Betts, A.K., Miller, M.J. (1986). A new convective adjustment scheme. Part II: Single column tests using GATE wave, BOMEX, and arctic air-mass data sets. Quart J Roy Meteor Soc 112: 693-709. https://doi.org/10.1002/qj.49711247308
[94] Janjic, Z.I. (1990). The step-mountain coordinate: physical package. Mon Wea Rev 118:1429-1443. https://doi.org/10.1175/1520-0493(1990)118<1429:TSMCPP>2.0.CO;2

[95] Janjic, Z.I. (1994). The step-mountain eta coordinate model: further developments of the convection, viscous sublayer and turbulence closure schemes. Mon Wea Rev 122:927-945. https://doi.org/10.1175/1520-0493(1994)122<0927:TSMECM>2.0.CO;2
[96] Janjic, Z.I. (2000). Comments on "Development and Evaluation of a Convection Scheme for Use in Climate Models." Journal of the Atmospheric Sciences 57:3686. https://doi.org/10.1175/1520-0469(2000)057<3686:CODAEO>2.0.CO;2
[97] Chen, F., Dudhia, J. (2001). Coupling an advanced land surface–hydrology model with the Penn State–NCAR MM5 modeling system. Part I: Model implementation and sensitivity. Mon Wea Rev 129:569–585. https://doi.org/10.1175/1520-0493(2001)129<0569:CAALSH>2.0.CO;2
[98] Collins, W.D., Rasch, P.J., Boville, B.A., Hack, J.J., McCaa, J.R., Williamson, D.L., Kiehl, J.T., Briegleb, B., Bitz, C., Lin, S-J, Zhang, M., & Dai, Y. (2004). Description of the NCAR Community Atmospheric Model (CAM 3.0). NCAR Tech. Note, NCAR/TN-4641STR, 226 pp
[99] Nogueira, M., Soares, P. M. M., Tomé, R., & Cardoso, R. M. (2018). High-resolution multi-model projections of onshore wind resources over Portugal under a changing climate. Theoretical and Applied Climatology. doi:10.1007/s00704-018-2495-4
[100] Wolfram Research, Inc. (2019), Mathematica, Version 12.0, Champaign, IL.
[101] Chan, A. L. S., Chow, T. T., Fong, S. K. F., & Lin, J. Z. (2006). Generation of a typical meteorological year for Hong Kong. Energy Conversion and Management, 47(1), 87–96. doi:10.1016/j.enconman.2005.02.010
[102] Aguiar, R., Carvalho, M. J., Gonçalves, H. (2013). Climatologia e anos meteorológicos de referência para o Sistema Nacional de Certificação de Edifícios (versão 2013).
[103] Met Office (2019). Met office HadCM3: Met Office climate prediction model.
[104] Riahi, K., Rao, S., Krey, V., Cho, C., Chirkov, V., Fischer, G., Kindermann, G., Nakicenovic, N., & Rafaj, P. (2011). RCP 8.5—A scenario of comparatively high greenhouse gas emissions. Climatic Change, 109(1-2), 33. https://doi.org/10.1007/s10584-011-0149-y
[105] Deru, M., Field, K., Studer, D., Benne, K., Griffith, B., Torcellini, P., Liu, B., Halverson, M., Winiarski, D., Rosenberg, M., Yazdanian, M., Huang, J., & Crawley, D. (2011). U.S. Department of Energy Commercial Reference Building Models of the National Building Stock. doi:10.2172/1009264
[106] Martins, N. R., & Carrilho da Graça, G. (2017). Impact of outdoor PM2.5 on natural ventilation usability in California's nondomestic buildings. Applied Energy, 189, 711–724. doi:10.1016/j.apenergy.2016.12.103
[107] Pierucci, A., Cannavale, A., Martellotta, F., & Fiorito, F. (2018). Smart windows for carbon neutral buildings: A life cycle approach. Energy and Buildings, 165, 160-171. https://doi.org/10.1016/j.enbuild.2018.01.021
[108] Martins, N. R., & Carrilho da Graça, G. (2017). Simulation of the effect of fine particle pollution on the potential for natural ventilation of non-domestic buildings in European cities. Building and Environment, 115, 236-250. https://doi.org/10.1016/j.buildenv.2017.01.030
[109] Kottek, M., Grieser, J., Beck, C., Rudolf, B., & Rubel, F. (2006). World map of the Köppen-Geiger climate classification updated. Meteorologische Zeitschrift, 15(3), 259-263. DOI:10.1127/0941-2948/2006/0130
[110] Nicol, J. F. (2001, August). Characterising occupant behaviour in buildings: towards a stochastic model of occupant use of windows, lights, blinds, heaters and fans. In Proceedings of the seventh international IBPSA conference, Rio (Vol. 2, pp. 1073-1078).
[111] Francisco Pinto, J., & Carrilho da Graça, G. (2018). Comparison between geothermal district heating and deep energy refurbishment of residential building districts. Sustainable Cities and Society, 38, 309–324. doi:10.1016/j.scs.2018.01.008

[112] Eurostat. Distribution of population by degree of urbanisation, dwelling type and income group - EU-SILC survey [ilc_lvho01]. Retrieved August 26, 2019, from https://ec.europa.eu/eurostat/web/income-and-living-conditions/data/database
[113] Intelligent Energy Europe: ENTRANZE. Retrieved August 26, 2019 http://www.entranze.enerdata.eu/.
[114] Herkel, S., Knapp, U., & Pfafferott, J. (2008). Towards a model of user behaviour regarding the manual control of windows in office buildings. Building and Environment, 43(4), 588–600. doi:10.1016/j.buildenv.2006.06.031
[115] International Organization for Standardization. ISO 7730:2005 – ergonomics of the thermal environment – analytical determination and interpretation of thermal comfort using calculation of the PMV and PPD indices and local thermal comfort criteria, November 2005.
[116] Zhang, Y., & Barrett, P. (2012). Factors influencing the occupants' window opening behaviour in a naturally ventilated office building. Building and Environment, 50, 125-134. https://doi.org/10.1016/j.buildenv.2011.10.018
[117] IEA - EBC Annex 62 Ventilative cooling, Ventilative Cooling: State-of-the-art review, 2015.
[118] Artmann, N., Gyalistras, D., Manz, H., & Heiselberg, P. (2008). Impact of climate warming on passive night cooling potential. Building Research & Information, 36(2), 111-128, DOI: 10.1080/09613210701621919
[119] Frich, P., Alexander, L. V., Della-Marta, P. M., Gleason, B., Haylock, M., Tank, A. K., & Peterson, T., Observed coherent changes in climatic extremes during the second half of the twentieth century. Climate research, 19(3), 2012, 193-212. doi:10.3354/cr019193
[120] Sun, Y., Gu, L., Wu, C. J., & Augenbroe, G. (2014). Exploring HVAC system sizing under uncertainty. Energy and Buildings, 81, 243-252. https://doi.org/10.1016/j.enbuild.2014.06.026
[121] Aguiar, R., Oliveira, M., & Gonccedilalves, H. (2002). Climate change impacts on the thermal performance of Portuguese buildings. Results of the SIAM study. Building Services Engineering Research and Technology, 23(4), 223-231. https://doi.org/10.1191/0143624402bt045oa
[122] Pérez-Andreu, V., Aparicio-Fernández, C., Martínez-Ibernón, A., & Vivancos, J. L. (2018). Impact of climate change on heating and cooling energy demand in a residential building in a Mediterranean climate. Energy, 165, 63-74. https://doi.org/10.1016/j.energy.2018.09.015
[123] Chen, Y., Tong, Z., & Malkawi, A. (2017). Investigating natural ventilation potentials across the globe: Regional and climatic variations. Building and Environment, 122, 386-396. https://doi.org/10.1016/j.buildenv.2017.06.026
[124] Roetzel, A., Tsangrassoulis, A., Impact of climate change on comfort and energy performance in offices. Building and environment, 57, 2012, 349-361. https://doi.org/10.1016/j.buildenv.2012.06.002
[125] Asimakopoulos, D. A., Santamouris, M., Farrou, I., Laskari, M., Saliari, M., Zanis, G., Giannakidis, G., Tigas, K., Kapsomenakis, J., Douvis, C., Zerefos, S. C., Antonakaki, T., Modelling the energy demand projection of the building sector in Greece in the 21st century. Energy and Buildings, 49, 2012, 488-498. https://doi.org/10.1016/j.enbuild.2012.02.043
[126] Nik, V. M., & Kalagasidis, A. S. (2013). Impact study of the climate change on the energy performance of the building stock in Stockholm considering four climate uncertainties. Building and Environment, 60, 291-304. https://doi.org/10.1016/j.buildenv.2012.11.005
[127] Hamdy, M., Carlucci, S., Hoes, P. J., & Hensen, J. L. (2017). The impact of climate change on the overheating risk in dwellings—A Dutch case study. Building and Environment, 122, 307-323. https://doi.org/10.1016/j.buildenv.2017.06.031

[128] Porritt, S. M., Cropper, P. C., Shao, L., & Goodier, C. I. (2012). Ranking of interventions to reduce dwelling overheating during heat waves. Energy and Buildings, 55, 16-27. https://doi.org/10.1016/j.enbuild.2012.01.043
[129] Frank, T. (2005). Climate change impacts on building heating and cooling energy demand in Switzerland. Energy and buildings, 37(11), 1175-1185. https://doi.org/10.1016/j.enbuild.2005.06.019.
[130] Domínguez-Amarillo, S., Fernández-Agüera, J., Sendra, J. J., & Roaf, S. (2019). The performance of Mediterranean low-income housing in scenarios involving climate change. Energy and Buildings, 202, 109374. https://doi.org/10.1016/j.enbuild.2019.109374
[131] Pajek, L., & Košir, M. (2018). Implications of present and upcoming changes in bioclimatic potential for energy performance of residential buildings. Building and Environment, 127, 157-172. https://doi.org/10.1016/j.buildenv.2017.10.040
[132] Lee, E. S., & Tavil, A. (2007). Energy and visual comfort performance of electrochromic windows with overhangs. Building and Environment, 42(6), 2439-2449. https://doi.org/10.1016/j.buildenv.2006.04.016
[133] Hausfather, Z., Drake, H. F., Abbott, T., & Schmidt, G. A. (2019). Evaluating the performance of past climate model projections. Geophysical Research Letters, 46. https://doi.org/10.1029/2019GL085378
[134] Giorgi, F. (2019). Thirty years of regional climate modeling: where are we and where are we going next?. Journal of Geophysical Research: Atmospheres, 124(11), 5696-5723. doi:10.1029/2018JD030094
[135] Samuelsson, P., Jones, C. G., Willén, U., Ullerstig, A., Gollvik, S., Hansson, U. L. F., Jansson, C., Kjellström, E., Nikulin, G., Wyser, K., The Rossby Centre Regional Climate model RCA3: model description and performance. Tellus A, 63(1), 2011, 4-23. https://doi.org/10.1111/j.1600-0870.2010.00478.x
[136] Vautard R, Gobiet A, Jacob D, Belda M, Colette A, Déqué M, Fernández J, García-Díez M, Goergen K, Güttler I, Halenka T, Karacostas T, Katragkou E, Keuler K, Kotlarski S, Mayer S, van Meijgaard E, Nikulin G, Patarcic ̆ c M, Scinocca J, Sobolowski S, Suklitsch M, ´ Teichmann C, Warrach-Sagi K, Wulfmeyer V, & Yiou P. (2013). The simulation of European heat waves from an ensemble of regional climate models within the EURO-CORDEX project. Clim. Dyn. 41: 2555–2575. https://doi.org/10.1007/s00382-013-1714-z.
[137] Rasmussen R, Liu C, Ikeda K, Gochis D, Yates D, Chen F, Tewari M, Barlage M, Dudhia J, Yu W, & Miller K. (2011). High-resolution coupled climate runoff simulations of seasonal snowfall over Colorado: a process study of current and warmer climate. Journal of Climate, 24(12), 3015-48. https://doi.org/10.1175/2010JCLI3985.1
[138] Rockel, B., Will, A., & Hense, A. (2008). The regional climate model COSMO-CLM (CCLM). Meteorologische Zeitschrift, 17(4), 347-348. doi:10.1127/0941-2948/2008/0309
[139] Daniel, M., Lemonsu, A., Déqué, M., Somot, S., Alias, A., & Masson, V. (2019). Benefits of explicit urban parameterization in regional climate modeling to study climate and city interactions. Climate Dynamics, 52(5-6), 2745-2764. https://doi.org/10.1007/s00382-018-4289-x
[140] Jacob, D. (2001). A note to the simulation of the annual and inter-annual variability of the water budget over the Baltic Sea drainage basin. Meteorology and Atmospheric Physics, 77(1-4), 61-73. https://doi.org/10.1007/s007030170017
[141] Guerreiro, S. B., Dawson, R. J., Kilsby, C., Lewis, E., & Ford, A. (2018). Future heat-waves, droughts and floods in 571 European cities. Environmental Research Letters, 13(3), 034009.

[142] Bravo Dias, J., Carrilho da Graça, G., & Soares, P. M. (2020). Comparison of methodologies for generation of future weather data for building thermal energy simulation. Energy and Buildings, 206, 109556. https://doi.org/10.1016/j.enbuild.2019.109556.
[143] Chiesa, G., & Grosso, M. (2015). Geo-climatic applicability of natural ventilative cooling in the Mediterranean area. Energy and Buildings, 107, 376-391. https://doi.org/10.1016/j.enbuild.2015.08.043
[144] Chiesa, G., & Grosso, M. (2017). Cooling potential of natural ventilation in representative climates of central and southern Europe. International Journal of Ventilation, 16(2), 84-98. https://doi.org/10.1080/14733315.2016.1214394
[145] Akbari, H., Pomerantz, M., & Taha, H. (2001). Cool surfaces and shade trees to reduce energy use and improve air quality in urban areas. Solar energy, 70(3), 295-310. https://doi.org/10.1016/S0038-092X(00)00089-X
[146] Reindl, D. T., Beckman, W. A., & Duffie, J. A. (1990). Diffuse fraction correlations. Solar energy, 45(1), 1-7. https://doi.org/10.1016/0038-092X(90)90060-P
[147] Sargent, J. A., Niemasz, J., & Reinhart, C. F. (2011, November). Shaderade: combining Rhinoceros and Energyplus for the design of static exterior shading devices. In Proceedings of Building Simulation (Vol. 2011, pp. 14-16).
[148] 2013 ASHRAE Handbook - Fundamentals (SI Edition). (2013). S.l.: American Society of Heating, Refrigerating and Air-Conditioning Engineers, Inc.
[149] De Munck, C., Lemonsu, A., Masson, V., Le Bras, J., & Bonhomme, M. (2018). Evaluating the impacts of greening scenarios on thermal comfort and energy and water consumptions for adapting Paris city to climate change. Urban Climate, 23, 260-286. https://doi.org/10.1016/j.uclim.2017.01.003
[150] Kolokotroni, M., & Giridharan, R. (2008). Urban heat island intensity in London: An investigation of the impact of physical characteristics on changes in outdoor air temperature during summer. Solar energy, 82(11), 986-998. https://doi.org/10.1016/j.solener.2008.05.004
[151] Giridharan, R., & Kolokotroni, M. (2009). Urban heat island characteristics in London during winter. Solar Energy, 83(9), 1668-1682. https://doi.org/10.1016/j.solener.2009.06.007
[152] Panão, M. J. O., & Brito, M. C. (2018). Modelling aggregate hourly electricity consumption based on bottom-up building stock. Energy and Buildings, 170, 170-182. https://doi.org/10.1016/j.enbuild.2018.04.010
[153] Reynders, G., Lopes, R. A., Marszal-Pomianowska, A., Aelenei, D., Martins, J., & Saelens, D. (2018). Energy flexible buildings: An evaluation of definitions and quantification methodologies applied to thermal storage. Energy and Buildings, 166, 372-390. https://doi.org/10.1016/j.enbuild.2018.02.040
[154] Dar, U. I., Sartori, I., Georges, L., & Novakovic, V. (2014). Advanced control of heat pumps for improved flexibility of Net-ZEB towards the grid. Energy and Buildings, 69, 74-84. https://doi.org/10.1016/j.enbuild.2013.10.019
[155] Hirvonen, J., Kayo, G., Hasan, A., & Sirén, K. (2016). Zero energy level and economic potential of small-scale building-integrated PV with different heating systems in Nordic conditions. Applied Energy, 167, 255-269. https://doi.org/10.1016/j.apenergy.2015.12.037
[156] Foteinaki, K., Li, R., Heller, A., & Rode, C. (2018). Heating system energy flexibility of low-energy residential buildings. Energy and Buildings, 180, 95-108. https://doi.org/10.1016/j.enbuild.2018.09.030
[157] Miara, M., Günther, D., Leitner, Z. L., & Wapler, J. (2014). Simulation of an Air-to-Water Heat Pump System to Evaluate the Impact of Demand-Side-Management Measures on Efficiency and Load-Shifting Potential. Energy technology, 2(1), 90-99. https://doi.org/10.1002/ente.201300087

[158] De Coninck, R., Baetens, R., Saelens, D., Woyte, A., & Helsen, L. (2014). Rule-based demand-side management of domestic hot water production with heat pumps in zero energy neighbourhoods. Journal of Building Performance Simulation, 7(4), 271-288. https://doi.org/10.1080/19401493.2013.801518
[159] Panão, M. J. O., Mateus, N. M., & Carrilho da Graça, G. (2019). Measured and modeled performance of internal mass as a thermal energy battery for energy flexible residential buildings. Applied Energy, 239, 252-267. https://doi.org/10.1016/j.apenergy.2019.01.200
[160] Hong, J., Johnstone, C., Torriti, J., & Leach, M. (2012). Discrete demand side control performance under dynamic building simulation: A heat pump application. Renewable energy, 39(1), 85-95. https://doi.org/10.1016/j.renene.2011.07.042
[161] Aelenei, D., Lopes, R. A., Aelenei, L., & Gonçalves, H. (2019). Investigating the potential for energy flexibility in an office building with a vertical BIPV and a PV roof system. Renewable Energy, 137, 189-197. https://doi.org/10.1016/j.renene.2018.07.140
[162] Arteconi, A., Ciarrocchi, E., Pan, Q., Carducci, F., Comodi, G., Polonara, F., & Wang, R. (2017). Thermal energy storage coupled with PV panels for demand side management of industrial building cooling loads. Applied Energy, 185, 1984-1993. https://doi.org/10.1016/j.apenergy.2016.01.025
[163] Sehar, F., Pipattanasomporn, M., & Rahman, S. (2016). An energy management model to study energy and peak power savings from PV and storage in demand responsive buildings. Applied energy, 173, 406-417. https://doi.org/10.1016/j.apenergy.2016.04.039
[164] Puchegger, M. (2015). Electric load behaviour and DSM potential of office buildings. Energy and Buildings, 100, 43-49. https://doi.org/10.1016/j.enbuild.2014.12.046
[165] Lappalainen, K., & Valkealahti, S. (2016). Analysis of shading periods caused by moving clouds. Solar Energy, 135, 188-196. https://doi.org/10.1016/j.solener.2016.05.050
[166] Lohmann, G. M. (2018). Irradiance variability quantification and small-scale averaging in space and time: A short review. Atmosphere, 9(7), 264. https://doi.org/10.3390/atmos9070264
[167] Salom, J., Marszal, A. J., Widén, J., Candanedo, J., & Lindberg, K. B. (2014). Analysis of load match and grid interaction indicators in net zero energy buildings with simulated and monitored data. Applied Energy, 136, 119-131. https://doi.org/10.1016/j.apenergy.2014.09.018
[168] Jager, D.; Andreas, A.; (1996). NREL National Wind Technology Center (NWTC): M2 Tower; Boulder, Colorado (Data); NREL Report No. DA-5500-56489. http://dx.doi.org/10.5439/1052222
[169] Vignola, F.; Andreas, A.; (2013). University of Oregon: GPS-based Precipitable Water Vapor (Data); NREL Report No. DA-5500-64452. http://dx.doi.org/10.7799/1183467
[170] Maxey, C.; Andreas, A.; (2007). Oak Ridge National Laboratory (ORNL); Rotating Shadowband Radiometer (RSR); Oak Ridge, Tennessee (Data); NREL Report No. DA-5500-56512. http://dx.doi.org/10.5439/1052553
[171] Wilcox, S., & Andreas, A. (2010). Solar Resource & Meteorological Assessment Project (SOLRMAP): Southwest Solar Research Park (Formerly SolarCAT) Rotating Shadowband Radiometer (RSR); Phoenix, Arizona (Data). United States. http://dx.doi.org/10.5439/1052225
[172] Reno, M. J., & Hansen, C. W. (2016). Identification of periods of clear sky irradiance in time series of GHI measurements. Renewable Energy, 90, 520-531. https://doi.org/10.1016/j.renene.2015.12.031
[173] Assunção, H. F., Escobedo, J. F., & Oliveira, A. P. (2007). A new algorithm to estimate sky condition based on 5 minutes-averaged values of clearness index and relative optical air mass. Theoretical and Applied Climatology, 90(3-4), 235-248. https://doi.org/10.1007/s00704-006-0283-z
[174] Li, D. H., Lau, C. C., & Lam, J. C. (2004). Standard skies classification using common climatic parameters. J. Sol. Energy Eng., 126(3), 957-964. https://doi.org/10.1115/1.1740776

[175] Muneer, T., Gul, M. S., & Kubie, J. (2000). Models for estimating solar radiation and illuminance from meteorological parameters. J. Sol. Energy Eng., 122(3), 146-153. https://doi.org/10.1115/1.1313529
[176] Cucumo, M., De Rosa, A., Ferraro, V., Kaliakatsos, D., & Marinelli, V. (2010). Correlations of direct solar luminous efficacy for all sky, clear sky and intermediate sky conditions and comparisons with experimental data of five localities. Renewable Energy, 35(10), 2143-2156. https://doi.org/10.1016/j.renene.2010.04.004
[177] Lucien Wald. (2019) Basics in solar radiation at earth surface – Revised version. 2019. ffhal-02164311
[178] Albuquerque, D. P., Mateus, N., Avantaggiato, M., & Carrilho da Graça, G. (2020). Full-scale measurement and validated simulation of cooling load reduction due to nighttime natural ventilation of a large atrium. Energy and Buildings, 224, 110233. https://doi.org/10.1016/j.enbuild.2020.110233
[179] DOE, U. S. (2016). EnergyPlus engineering reference: the reference to EnergyPlus calculations. Lawrence Berkeley National Laboratory.
[180] Hong, T., & Lee, S. H. (2019). Integrating physics-based models with sensor data: An inverse modeling approach. Building and Environment, 154, 23-31. https://doi.org/10.1016/j.buildenv.2019.03.006
[181] Bergman, T. L., Incropera, F. P., DeWitt, D. P., & Lavine, A. S. (2011). Fundamentals of heat and mass transfer. John Wiley & Sons.
[182] Zhao, J., Lasternas, B., Lam, K. P., Yun, R., & Loftness, V. (2014). Occupant behavior and schedule modeling for building energy simulation through office appliance power consumption data mining. Energy and Buildings, 82, 341-355. https://doi.org/10.1016/j.enbuild.2014.07.033
[183] Leach, M., Lobato, C., Hirsch, A., Pless, S., & Torcellini, P. (2010). Technical support document: Strategies for 50% energy savings in large office buildings (No. NREL/TP-550-49213). National Renewable Energy Lab.(NREL), Golden, CO (United States). https://doi.org/10.2172/989024
[184] Ertesvåg, I. S. (2011). Uncertainties in heat-pump coefficient of performance (COP) and exergy efficiency based on standardized testing. Energy and buildings, 43(8), 1937-1946. https://doi.org/10.1016/j.enbuild.2011.03.039
[185] Carrilho da Graça, G., Martins, N. R., & Horta, C. S. (2012). Thermal and airflow simulation of a naturally ventilated shopping mall. Energy and Buildings, 50, 177-188. https://doi.org/10.1016/j.enbuild.2012.03.037
[186] Huld, T., Müller, R. and Gambardella, A., 2012. "A new solar radiation database for estimating PV performance in Europe and Africa". Solar Energy, 86, 1803-1815.
[187] JA Solar, “320W PERC Module. JAM60S01 300-320/PR”, Version No.: Global_EN_20180824A.
[188] Carrilho da Graça, G., & Linden, P. (2016). Ten questions about natural ventilation of non-domestic buildings. Building and Environment, 107, 263-273. https://doi.org/10.1016/j.buildenv.2016.08.007
[189] Corgnati, S. P., & Kindinis, A. (2007). Thermal mass activation by hollow core slab coupled with night ventilation to reduce summer cooling loads. Building and environment, 42(9), 3285-3297. https://doi.org/10.1016/j.buildenv.2006.08.018